UNIVERSITÀ DEGLI STUDI DI UDINE
hic sunt futura

www.uniud.it

Corso di dottorato di ricerca in:

"Scienze dell'Ingegneria Energetica e Ambientale"

in convenzione con Technische Universität Wien (TU Wien)
Doktoratsstudium der
Technischen Wissenschaften Maschinenbau

Ciclo (es. 33°)

Titolo della tesi

"Orientation and rotation rate of non-axisymmetric fibers in turbulent channel flow"

in co-tutela con Technische Universität Wien (TU Wien)

Dottorando

Supervisore

Co-supervisore

Anno (di discussione, non a.a.)

Università degli Studi di Udine
Dottorato di Ricerca in
Scienze dell'Ingegneria Energetica e Ambientale
XXXIII Ciclo

Technische Universität Wien
Doktoratsstudium der
Technischen Wissenschaften Maschinenbau

Orientation and rotation rates of non-axisymmetric fibers in turbulent channel flow

Mobin Alipour

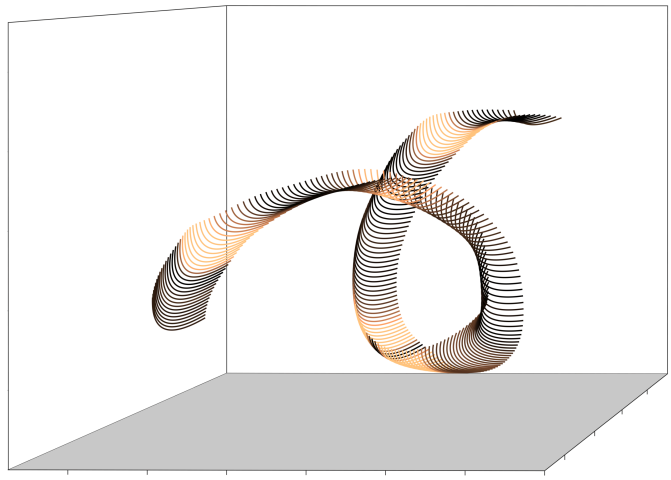

BOARD MEMBERS

Prof. Nicholas T. Ouellette	Reviewer
Prof. Chao Sun	Reviewer
Prof. Hendrik Kuhlmann	Committee member
Prof. Greg Voth	Committee member
Prof. Björn Hof	Committee member
Prof. Alfredo Soldati	Supervisor
Prof. Cristian Marchioli	Co-Supervisor
Prof. Alessandro Trovarelli	Doctorate Chair

Author's e-mail:
alipour.mobin@spes.uniud.it
mobin.alipour@tuwien.ac.at

Author's address:
Dipartimento Politecnico di Ingegneria e Architettura
Università degli Studi di Udine
Via delle Scienze 206
33100 Udine, Italy
Web: DIEGM - University of Udine

Institute of Fluid Mechanics and Heat Transfer
Technische Universität Wien
Getreidemarkt 9/E322
1060 Wien, Austria
Web: ISW - TU Wien

Cover:

Example of the measurement of a non-axisymmetric fibre travelling close to the wall, represented here by the grey surface. Fibre is coloured according to the instantaneous tumbling rate $\Omega_t\Omega_t$, normalised by the mean value computed over the entire track, $|\Omega_t\Omega_t|$. Gold colour represent higher mean square tumbling rate, while the balck color represents the lower magnitude. The acquisition rate is sufficiently high to resolve the dynamics of the fibre also in this case, in which the behaviour is complex (one every three instants measured is shown here).

Abstract

In this work, we investigate the dynamics of long non-axisymmetric fibers in turbulent channel flow. The experimental facility is the TU Wien Turbulent Water Channel, consisting of a closed water channel (aspect ratio 10), and the experiments are performed at the shear Reynolds number of 180, 360 and 720. Fibers are neutrally buoyant rods, length-to-diameter ratio of 120, and their asymmetry in shape is induced by a curvature. We propose, for the first time, a three-dimensional reconstruction and tracking method for non-axisymmetric fibers based on the light intensity distribution, which is obtained with the multiplicative algebraic reconstruction technique (MART). First, we discriminate the fibers, i.e. the voxels corresponding to the location of the fibers are detected. Then the curvature and orientation of the fibers are identified and the fibers are tracked within the measurement volume. We show that the proposed fiber detection methodology allows an accurate and time-resolved reconstruction of both position and orientation of the fibers. We investigate the behaviour of the fibers, from the near-wall region to the channel center, and we produce original statistics on the effect of curvature of the fibers on their orientation and rotation rates. Shape asymmetry shows a significant effect on the distribution, orientation and rotation rates. Our measurements of the orientation and rotation rates of the fibers in the center of the channel, the most homogenous part of the channel, shows that statistics, although influenced by the curvature, bear similarities with those obtained in previous investigations in homogenous isotropic turbulence. Preferential orientation of the fibers in the near wall region shows a noticeable influence by the near wall coherent structures, and shape asymmetry dictates the different orientations for fibers. In particular, we observed that orientation of curved fibers in the near wall region, bears similarities with the inertial disks preferential orientation. In this thesis, we also show that, non-axisymmetric fibers have higher probability to experience extreme motions in the near-wall region compared to the channel center. Statistics of both mean square spinning and tumbling rates of the fibers are reported in this study. We have been able to compare the tumbling rate of our long non-axisymmetric fibers with previous solutions for curved ellipsoids in simple shear flow. Finally, we report that, independent of fibers shape asymmetry rate and their length to flow Kolmogorov length scale ratio, fibers tend to spin more than tumble, $\langle \Omega_s \Omega_s \rangle / \langle \Omega_t \Omega_t \rangle > 1$ and magnitude of this ratio decreases by increasing the asymmetry in shape.

Contents

Acknowledgements

During the last 45 months, I had the privilege to take part in setup, design and performing experiments of three different projects, among which, one was my PhD thesis. A unique experience and an exciting opportunity for a young PhD student. I am happy to had this chance, I learned a lot and will always appreciate it. I would like to thank my PhD supervisor, Prof. Alfredo Soldati, who provided me this unique opportunity and always supported me during my PhD with his insightful advises. His suggestions shaped the basis of my future academic career, the thing that I will always remember and appreciate. I would also like to thank Dr. Marco De Paoli, who generously helped me to tackle the challenges I had during my PhD and was available all the times, he was patient and always kind. I also would like to thank Prof. Cristian Marchioli, my PhD co-supervisor, for the interesting discussions and kind advises, and Dr. Francesco Zonta for his kind and honest suggestions whenever I needed to took important decisions. I will never forget the coffee break chats about football and the philosophy of not to disturb the universe. A special thanks goes to the committee members and reviewers, who spent time for reviewing and assessing my work. Their comments, suggestion and insightful observations are greatly appreciated and were very helpful. I would like to sincerely thank Prof. Sina Ghaemi for all the online discussions and his kind suggestions regarding the experiments.

I would like to thank my close friend Ali Farid who is just like my brother, we started our journey abroad 8 years ago, and each year passing, our friendship bonds got stronger. I really appreciate the support from my close friends: Farzad Shams, Salar Rahimi and Arsalan Javanmard. Our weekly online meetings were always joyful and boosted my mood. I would also like to thank my colleagues, Arash and Pejman who became my dear friends in the last 3 years. Their support and friendship, especially during the last months, was very crucial for me and will always be in my mind, I am really happy and feel lucky to met them. I am also thankful to Alessio and Giovanni, my dear colleagues, for their support, hosting dinners and board games. I should also thank Atabak, my old friend, who was always supportive and kind. I am grateful for the help and support of Mr. Werner Jandl and Mr. Franz Neuwirth, our laboratories technical staff, without which, setting up the experiments would have been much more difficult.

All said, I would like to sincerely thank my beloved family. My parents and lovely sister, without their patient, love and moral support I could not have enough courage to continue the path I started. I wish, there will be a day that I can make them happy and proud and we can all be together. Last thing to say, I hope in the near future, If I have enough merit to stay in academia and achieve my personal goals, when I open this thesis and check these pages, I will feel happy by the choices that I have taken up to that date and have not forgotten the lessons that I learnt from this stage of my career.

1 Introduction

The prediction of preferential orientation of anisotropic particles in turbulent flows is of importance because of the many implications it can bear for industrial and environmental applications [85]. Anisotropic particles have applications in industrially-relevant flows, such as in pulp and papermaking [51] and environmental problems, like modelling of phytoplankton [31, 7], sedimentation [55], aerosols [42], ice crystals in clouds [80, 47, 39] and micro-fiber pollution in ocean [71]. Among all different types of anisotropic particles, fibers have significant importance due to their wider range of applications. In majority of the applications, fibers are not perfectly symmetrical and they have asymmetry in their shape. This asymmetry is important since it could influence their orientation and rotational dynamics. In this study, for the first time, we aim at investigating the orientation and rotation rate of non-axisymmetric fibers in turbulent channel flow by means of volumetric experimental techniques. This chapter is tailored in this way: first, in §1.1, a thorough overview of the literature by focusing on the experimental investigations of anisotropic particles, is presented. Later on, in §1.2, the scope and outline of the thesis, including a brief description of each chapter, is provided.

1.1 Literature review

In recent years, significant effort has been devoted to investigate numerically the dynamics of rigid and axisymmetric ellipsoids in homogeneous and isotropic turbulence (HIT) [79, 59, 16, 70] and in turbulent channel flow [56, 52, 92, 93, 20, 19, 53, 91, 27, 28]. Natural fibers can have complex and non-regular shapes, hard to be systematically characterised. Therefore, many theoretical and numerical investigations have been focused on axisymmetric ellipsoids: in this case fluid torques are mathematically trackable, and this shape has the advantage that the torques on small particles with many other shapes are the same as their equivalent ellipsoids [12, 13]. Many analyses on axisymmetric ellipsoids in turbulence have been conducted via numerical simulations, which due to high computational costs, limited the applications to moderate Reynolds numbers, an exception being the recent numerical simulation of Jie et al. [40]. The common assumption of these works is that the particles size is set to be smaller than the smallest length scale of the flow, a condition that might not be satisfied in practical applications. Recent numerical investigations on finite-size ellipsoid in turbulent

channel flow [26, 30, 95, 87, 5, 96] overcame this small size assumption, but they are limited to even lower flow Reynolds numbers, small overall number of particles and small fiber aspect ratio.

One of the first attempts to experimentally investigate the orientation of anisotropic particles in turbulent flow was done by Bernstein and Shapiro [8]. They performed a wide range of experiments at low and moderate Reynolds numbers in a pipe flow and did the recoding by using Microscopic Video-Photography. Orientation Density Function of the particles by means of calculating the distribution of the frequency of Euler angles in a planar configuration is presented in their work. They observed a broad distribution with a tendency towards random distribution for particles in turbulent regime. Later on, Parsheh et al. [67], did perform experiments on rigid fibers at nearly homogenous isotropic turbulence side of a planar contraction. They did a planar image processing and measure the orientation distribution of rigid fibers, where fibers with curvature were eliminated from the statistic. They showed that orientation distribution is weakly depended on the Reynolds number and the fiber diameter is an appropriate length scale to evaluate the fiber inertia. Parsa et al. [65], did simultaneous measurement of flow and laden rods in a chaotic quasi-two-dimensional fluid flows. They did use fluorescent rods and tracers for two dimensional and simultaneous tracking process. Regardless of the length of the rods used in their experiments, results of the measured rotation rate of the rods were in good agreement with the predicted rotation rate by assuming uniform velocity gradient tensor acting on non-inertial ellipsoids. In addition, they observed that the length of the rod does not have significant role on the alignment of rods with the direction of the Cauchy-Green deformation tensor, even though the rods used in their experiments in some cases were much longer than flow length scale.

Dearing et al. [22], did introduce a phase discrimination algorithm for investigating concentration and orientation data of rigid rods in turbulent pipe flow. The discrimination was based on two dimensional image processing and coupled with planar Particle Image Velocity of the driving flow. Authors showed that fibers prefer to align almost parallel to the channel in the close wall region. Concentration and orientation data were compared with Direct Numerical Simulation (DNS) data of [52]. Although, in general, there is a good agreement between the results, concentration peak happens in higher y^+, channel height in wall units, compared to the DNS predictions. In addition, DNS data, predicts that orientation of the fibers in center of the channel are close to random distribution, which looks under predicted compared to the experimental data. Both of the discrepancies observed in the comparison of the data, are speculated to be originated from the assumptions taken to account in the modelling used for the DNS and also the intrinsic loss of information associated with the two-dimensional experimental measurement. Håkansson et al. [33], investigate the effect of concentration on fiber streaks in free surface wall turbulence by using one dimensional Voronoi analysis. They observed that concentration does not have any effect on the streak width for concentration higher than 0.05 particle per pixel column in an image. Later on, Capone et al. [17], studied the effect of rods with Stokes number around unity in the inlet and downstream region of a jet pipe flow. This study was a simultaneous flow and laden phase investigation based on the phase discrimination algorithm presented by authors for planar configurations. Their results showed that rod like particles with

this range of Stokes number (0.7) have a lag in their velocity with respect to unladen phase in the inlet region, where this lag is decreasing in downstream region. In addition, they showed that turbulence intensity is increasing in presence of the rod like particles, which is in contrast of effect induce by spheres, and authors speculate the reason behind this difference to the wake originated by the rotation and translation of the rods.

Abbasi Hoseini et al. [2], did simultaneous planar Particle Image Velocimatery of unladen and Particle Tracking Velocimetry of laden flows in free surface wall turbulence. They suspended the flow with rod like particles in three aspect ratios. Their results show that fiber-wall interaction is dependent on the fibers aspect ratio, where shorter ones are indirectly affected by coherent structures than physical interaction with wall. They also showed that in buffer region, shorter fibers accumulates preferentially in low-speed regions while the longer ones has a same likelihood to exists in either sweep or ejection regions. First experimental study on the dynamics of rigid rod like particles laden in turbulent channel flow, is in planar PTV configuration and done by Capone et al. [18], but with the intrinsic loss of information associated with the two-dimensional measurements. They observed that in the close wall region fibers stream-wise velocity is higher than surrounding fluid suggesting their preferential distribution in near wall high-speed coherent structures, similar to the observation done by Abbasi Hoseini et al. [2] done in free surface wall turbulence. In addition, it is shown in their work that the relative concentration decreases in buffer region linearly compare to channel center without any sign of accumulation in the near wall zone, in contrast of the prediction of numerical simulations, [52], where there should be a accumulation in the vicinity of approximately one L^+, fiber length in wall units, of the wall. Yang et al. [90] did perform experiments of both rod and disk like inertial ellipsoid in two dimensional turbulence conditions. They show that rods with larger aspect ratio have movements which are predominant with their major axis direction. Later, Di Benedetto et al. [24], investigate the preferential orientation of the both neutrally and negatively buoyant rod and disk like ellipsoids in a free surface gravity wave flow. By using planar image analysing, they gave the statistics of both polar and out of plane orientation of the particles as function of the wave strength. Their results are in agreement with the previously suggested theoretical prediction, [23], for wave induced polar preferential orientation, ϕ_w. The authors show that the PDF of the orientation of the particles has a bimodal shape due to the competition between wave and settling forces where peaks refers to ϕ_w and the settling preferential orientation, $\phi_s = \pi/2$. In addition, their statistics show that some portion of the particles have tendency toward orthogonal orientation with respect to the wave panel (out of plane orientation). Recently, Bakhuis et al. [6], did perform a series of interesting experiments of sub-centimetre cylinders inside a Taylor-Couette facility where flow was in ultimate regime of TC configuration. Cylinders diameter and length were both larger than Kolmogorov length scales of the flow. They showed that concentration is homogenous in radial direction and particles show almost no lag with respect to flow velocity. The latter is surprising due to the relatively big size of the particles and high value of Stokes number based on Kolmogorov time scale and authors explained this by considering the turbulent dynamic time in the size scale of the particles. Interestingly, they showed that no matter what is the Reynolds number or concentration of the

particles, their preferential orientation with respect to the inner wall of the TC cell is approximately $-68° \pm 9°$.

Most of the recent volumetric experimental investigations of anisotropic particles have been done in Homogenous Isotropic Turbulence (HIT). In two separate papers and for the first time, Parsa et al. [66] and Parsa and Voth [64], performed series of experiments in HIT and track the slender rods with different aspect ratios by using three dimensional tracking technique. In their pioneering works, they show that anisotropic rode like particles preferentially follow the driving flow due to the tendency of their orientation to be correlated by the velocity gradient tensor. Moreover, they conclude that this alignment depends on shape of the particle, which eventually can heavily affect the rotation rate. In the latter work, the authors investigated wider range of rods including higher values of L^*, ratio of length of rod to the Kolmogorov length scale of the flow, and eventually reported a scaling law for the mean square rotation rate of rods as a function of the length of fibers in the inertial range, $\langle \dot{p}_i \dot{p}_i \rangle \propto {L^*}^{-4/3} \tau_k^{-2}$, where $\mathbf{p}$ is the orientation vector and τ_k is the Kolmogorov time scale of the flow. Another interesting finding of this work was the point that, in general, rotation of the rods are controlled by the eddies with a size near to their length and the Probability Density Function of the rotation rate weakly depends on the length of the rods. Bordoloi and Variano [9], did experiments by using cylindrical hydrogel particles where both length and diameter of the particles were larger than the length scale of the flow. Since they used transparent particles filled with tracers, they were able to use Stereo Particle Image Velocimetry method to reconstruct the flow velocity and measure the angular velocity of the particles. They found that the mean square enstrophy of the particle scales as $\langle \Omega_i \Omega_i \rangle \propto {d_{eq}}^{-4/3} \tau_k^{-2}$, where d_{eq} is the volume-equivalent spherical diameter of the cylinders and Ω is the angular velocity of the particles. Mean square enstrophy is equal to the summation of mean square spinning and tumbling where spinning is the particle rotation around the principal axis and tumbling refers to the rotation around axis perpendicular to the principal axis. Difference in the scaling of this study and what Parsa and Voth [64] suggested was hypothesised to two possible reasons by the authors: first, Parsa and Voth [64], only considered tumbling and not the full body rotation in the scaling and second, they used slender rods with much smaller diameter compared to what Bordoloi and Variano [9] used in their study.

Later on, to answer this discrepancy, Bounoua et al. [11], did investigate the same scaling by using wide range of aspect ratio of inertial rods relying on varying diameter and length separately. They introduced a new derivation for Stokes number, tumbling stokes number S_{tp}, which is derived from conservation of angular momentum and neglecting the Coriolis term of it. They showed that thumbing can be scaled as $\langle \dot{p}_i \dot{p}_i \rangle \propto 1/(1 + S_{tp}^2) {L^*}^{-4/3} \tau_k^{-2}$, by which both results of Parsa and Voth [64] and Bordoloi and Variano [9] will collapse on a same curve. In this scaling, τ_k refers o Kolmogorov time scale. This scaling is verified by Kuperman et al. [49], where authors did experimental investigation on the dynamics of the inertial rods in HIT and using Digital Holographic Cinematography to reconstruct the fibers in 3D Volume describe in detail in Sabban et al. [74]. Bordoloi et al. [10], did experiments of mesoscale rods with wide range of L^* in HIT and successfully fit the data with the same scaling suggested by Bounoua et al. [11]. Based on the author knowledge, the only available study for investigating the mean square spinning of the inertial fibers, is very recently published

by Oehmke et al. [62], where they use visual helix marks on the surface of the fibers by which they can measure the spinning. Fibers used in their study are all inertial, $L^* > 10$ and they report both statistics of mean square spinning and tumbling. They observed that, same as fibers with length smaller than Kolmogorov length scale, fibers spin more than tumble even when they are inertial. This observation is in agreement with recent numerical work done by Picardo et al. [68], where they suggest that inertial fibers preferentially trap in vortex tube and as a result they spin more than tumble. In addition, Oehmke et al. [62] showed that unlike tumbling, mean square spinning should be scaled by the fiber diameter rather than the length, $\langle \Omega_s \Omega_s \rangle \propto d^{*-4/3} \tau_k^{-2}$, where d^* stands for the ratio of the fiber diameter to the Kolmogorov length scale of the flow.

Very recently, Jiang et al. [38] investigated the rotation of oblate and prolate spheroids in Rayleigh-Bénard Cell. They showed that, the trend of mean square tumbling rate as function of the aspect ratio, has a peak for weakly oblate spheroids which is in contrast of universal trend previously reported for HIT configuration. The authors shows that this difference between the trends decreases by reducing the mean shear effect induced by kinetic boundary layer. Only available experimental study on fibers in turbulent channel flow done by means of volumetric experimental methods is published very recently by Shaik et al. [78], where they used Digital Holographic Cinematography to reconstruct the fibers in 3D Volume describe in detail in Sabban et al. [74]. Fiber used in this study have Stokes numbers of 0.2 and 0.34. Authors observed that, although fibers lag the stream-wise velocity of the unladen flow in the channel center, they have higher average stream-wise velocity in the vicinity of the wall region. They also showed that fibers mean square tumbling non-dimensiolised by the viscous time scale of the flow, $\langle \Omega^+ \Omega^+ \rangle$, stays constant in the vicinity of the channel center and the magnitude increases by approaching the wall.

There are couple of experimental attempts to investigate the dynamics of anisotropic particles with complex shapes. Marcus et al. [54] did use cross and jack shaped particles in HIT chamber and investigate their rotation rate. Jack, which is consist of four symmetrical arms, and Cross, which is consist of two intersecting symmetrical arms, were used with the aim of possible similarities with sphere and oblate spheroids respectively. Indeed, mean square tumbling rate of the cross shaped particles were in agreement with the DNS predictions for oblate spheroids, same for Jack particle where they showed a same behaviour as spheres. Pujara et al. [69] did use cube, cuboid and cone as well as inertial and big rods in a HIT configuration and investigate their dynamics and rotation rate, where they reported a scaling for mean square full body rotation rate equal to $\langle \Omega_i \Omega_i \rangle \propto {d_{eq}}^{-4/3}$, which is same as what is reported in the same research groups earlier work [9]. In addition to these works, in the recent years, there are some experimental studies for investigate the dynamics of flexible particles. For the first time, Brouzet et al. [14] did investigate the dynamics of flexible filaments in HIT configuration and their results show that there is a specific threshold for the length of the filament smaller than which effect of flexibility will be negligible in turbulence. Very recently, Hejazi et al. [34] did experiments by using flexible triads, an object consist of three symmetric arms, in a vertical turbulent channel flow with aim of direct reconstructing the velocity gradient tensor by using arm deformation and rotation rate. Initially, they introduce a model correlating the fluid strain to particle's deformation

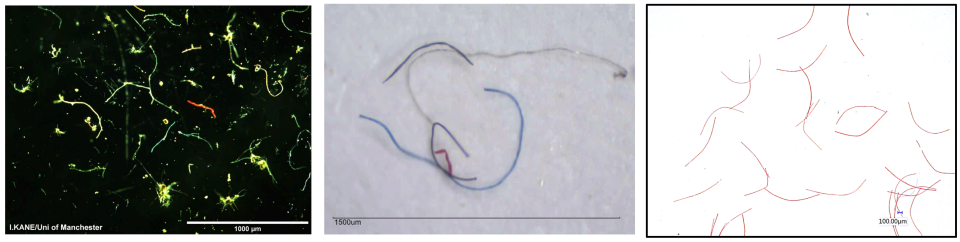

FIGURE 1.1 – Panel (a) Microscope photograph of sample extracted from marine sediments [41]. Panel (b) Microscope photograph of sample extracted from a water sample in Blue Hill Bay in the gulf of Maine. Photograph: Marine Environmental Research Institute. Panel (c) Non-axisymmetric fibers used in this study.

by using the data of 2D experiments in linear shear flow and then examine the model in 3D experiments. Although 3D experiments were done with an excellent accuracy for Euler angles and results were promising, since each particle needs an individual calibration, measuring deformation statistics and velocity gradient in turbulence were not possible and should be considered as a possible future development.
However, in most of industrial and environmental applications, rod-like particles are not axisymmetric; they have an asymmetry in their shape or mass distribution. For instance, microscopic image of microfibers obtained from marine sediments and sea water are shown in figure 1.1(a) and (b), where it is obvious that all fibers are extremely slender and more importantly they have an asymmetry in their shape. In figure 1.1(c), fibers used in this study is shown and there is a significant similarity in terms of asymmetry in shape with real microfibers shown in figure 1.1(a) and (b). Experimental results on the settling behaviour of inertial rods, Roy et al. [73], showed that rods undergo a critical change in orientation due to asymmetry in their mass distribution, and it was shown theoretically by Hinch and Leal [35] and numerically by Wang et al. [88], Crowdy [21] and Thorp and Lister [83] that even small deviations from the axisymmetric shape can produce a significant change of the rotational dynamics. To the best of our knowledge, neither experimental nor numerical works on non-axisymmetric shape fibers in turbulent flows are currently available, and we aim precisely at this gap.

1.2 Scope of the thesis

In this study, we investigate the dynamics of long, non-axisymmetric fibers in a turbulent channel flow and introduce a novel experimental methodology by which we are able to evaluate the effect of shape assymetry on the dynamics of the fibers. Experiments are carried out in the TU Wien Turbulent Water Channel, which is a gravity driven, large aspect ratio facility. Turbulence is naturally generated by a long hydrodynamic developing length. Fibers used in this study are neutrally buoyant, have different curvatures and all are dispersed in the flow simultaneously. Three-dimensional imaging of the fibers is carried out to reconstruct the shape and spatial orientation of the fibers and track their motion. The database produced consists of concentration, orientation

and rotation rates of fibers that are classified according to their curvature. The measurements cover more than half of the channel height, to capture both the center of the channel (HIT-like turbulence) and the near-wall region (inner and buffer layers, controlled by shear and viscous forces). The fibers used in this study can be considered as slender bodies with high length-to-diameter ratio, $\lambda = 120$, and very small Stokes number, $St < 0.02$ depending on the Reynolds number of the experiment.
The thesis is organised as following chapters:

- In §2, experimental facility, particles parameters and image acquisition system are described. Moreover, the methodology used to reconstruct and track the fibers is presented in this chapter. This methodology provides us an opportunity to detect the asymmetry of the fibers, in this case curvature, while they are tracked in time. In this way, we can investigate the effect of curvature on the statistics of the fibers.

- In §3, we measured the orientation and rotation rate of the fibres according to their curvature in shear Reynolds number, $\mathrm{Re}_\tau = 360$. We compare the tumbling rate of our long non-axisymmetric fibres with previous solutions for curved ellipsoids in simple shear flow. This solution is provided by solving numerically the autonomous system of ordinary differential equations for the Euler angles of curved ellipsoids in laminar shear flow, introduced by Hinch and Leal [35].

- In §4, we investigate the effect of Reynolds number on the concentration, orientation and rotation rate of the fibers. Statistics are provided for three Reynolds numbers, Re_τ=180, Re_τ=360 and Re_τ=720 and similar to §3, statistics are classified based on fibers curvature. In this chapter, particular focus is on the reasons behind the observed trends for fibers concentration and orientation.

- In §5, we introduced the adaptive filtering method and evaluate its effect compared to case of constant kernel by referring to the the mean square tumbling and spinning rate statistics. In addition to the curvature, we also classify the statistics based on the end-to-end length (named as effective length) of the fibers, L_{eff}. Tumbling and spinning statistics are provided for three Reynolds numbers, Re_τ=180, Re_τ=360 and Re_τ=720 and shown as function of the ratio of effective length to the local Kolmogorov length scale, $L^* = L_{eff}/l_k$.

- In §6, we provide the brief qualitative results of the fibers, classified based on their curvature class, by particular focus on near wall region and recording much larger domain in span-wise direction for Re_τ=180. In this way, we are able to investigate the possible influence of near wall coherent structures such as turbulent streaks on the orientation and concentration of fibers.

- In §7, conclusions, possible applications and suggested future works of this study are discussed.

Reference	Particle shape	Type	Re	λ	St_η	L_f/l_{flow}	Apparatus/Technique
Bernstein and Shapiro [8]	Rod	Rigid	51-1.089$\times 10^4$	10	NA	NA	PF/ 2D-ODF
Parsheh et al. [67]	Rod	Rigid	[1][8.5-17]$\times 10^4$	56.14	[5.6-6.25]$\times 10^{-3}$	NA	CWL / 2D-IP
Parsa et al. [65]	Rod	Rigid	[1]95-187	5-20	NA	NA	SEFL / 2D-DS + 2D-T
Parsa et al. [66]	Rod	Rigid	[2]160-214	5	NA	2.6-4.8	HIT / 3D-T
Dearing et al. [22]	Rod	Rigid	[3]250	13.3	0.7	NA	PF / 2D-DS + 2D-PIV
Capone et al. [17]	Rod	Rigid	[1]9000	13.3	0.7	NA	TPJ / 2D-DS + 2D-PIV
Marcus et al. [54]	Jack and cross	Rigid	[2]91	[1]10	NA	[3]6	HIT / 3D-T
Parsa and Voth [64]	Rod	Rigid	[2]150-210	5:76	NA	2.8-72.9	HIT / 3D-T
Brouzet et al. [14]	Filament	Flexible	[1][1-14]$\times 10^6$	12.22:258	NA	NA	VKF / 3D-T
Ni et al. [60]	Rod	Rigid	[2]140	23.3	0.008	2.3	HIT / 3D-T
Abbasi Hoseini et al. [2]	Rod	Rigid	[3]170	7-28	0.2:0.3	NA	WT / 2D-PIV+2D-PTV
Kramel et al. [46]	Chiral dipoles	Rigid	[2]120-183	10	NA	35-72	HIT / 3D-T
Sabban et al. [74]	Rod	Rigid	[2]130	36.5-19	1.35-2.34	2.8	HIT / 3D-T
Bordoloi and Variano [9]	Hydrogel cylinders	Rigid	NA	0.96-3.79	0.36-0.95	16.6-68.7	HIT / S-PIV
Capone et al. [18]	Rod	Rigid	[3]780	13.3	0.7	23	WBCF / 2D-T
Bounoua et al. [11]	Rod	Rigid	[2]350-610	2.5-80	[1]0.016-2.8	22-850	CTT / 3D-T

TABLE 1.1 – Caption is described in the next page.

Reference	Particle shape	Type	Re	λ	St_η	L_f/l_{flow}	Apparatus/Technique
Pujara et al. [69]	Cube, cuboid, cone, rod	Rigid	[2]261	1-3.72	NA	[2]13-55	HIT / S-PIV
Hejazi et al. [34]	Triads	Flexible	[2]198	[2]10	NA	[3]39.28	VWBCF / 3D-T
Zhao et al. [94]	Rod	Rigid	[2]140-271	23.3	0.002-0.01	2.3-5.2	HIT / 3D-T
Kuperman et al. [49]	Rod	Rigid	[2]115	30.7-88.1	1-32.5	3.6-17.3	HIT / 3D-T
Bakhuis et al. [6]	Rod	Rigid	[1][8.3-25]$\times 10^5$	5.3	110-510	44-95	TC / 2D-T
Di Benedetto et al. [24]	Rod and Disk	Rigid	[4]46-66	$0.16 - 7.8$	NA	NA	SGWF / 2D-T
Bordoloi et al. [10]	Rod	Rigid	[2]350-610	2-80	[2]0.014-2.68	51.1-858.9	HIT / 3D-T
Jiang et al. [38]	Rod and disk	Rigid	[5]545	6-1/6	NA	1.43-1.57	RBC / 3D-T
Shaik et al. [78]	Rod	Rigid	[3]435	31-47	0.22-0.34	28-51	WBCF / 3D-T
Oehmke et al. [62]	Rod	Rigid	[6]90-630	5.4:10.8	[3]< 0.02	10:220	HIT / 3D-T
Present study	Rod (non axisymm.)	Rigid	[3]360	120	0.003	2.38	WBCF / 3D-DS + 3D-T

TABLE 1.2 – Summary of experimental investigations on anisotropic particle laden flows available in literature. Apparatuses and techniques are reported and abbreviated as follow: Pipe Flow (PF), Orientation Density Function (ODF), Close Water Loop (CWL), Two dimensional Image Processing (2D-IP), Shallow Electrolytic Fluid Layer (SEFL), Two dimensional Phase Discrimination (2D-DS), Two dimensional Tracking (2D-T), Homogenous Isotropic Turbulence (HIT), Three-dimensional Tracking (3D-T), Two dimensional Particle Image Velocimetry (2D-PIV), Water table (WT), Turbulent Pipe Jet (TPJ), Von Kàrmàn Flow (VK), Two dimensional Particle Tracking Velocimetry (2D-PTV), Stereoscopic Particle Image Velocimetry (S-PIV), Wall Bounded Channel Flow (WBCF), Cube Tank Turbulence (CTT), Vertical Wall Bounded Channel Flow (VWBCF), Taylor-Couette (TC), Surface Gravity Wave flow (SGWF), Rayleigh-Bénard Cell (RBC) and Three-dimensional Phase Discrimination (3D-DS). Re is the Reynolds number and [1],[2],[3],[4] refer to bulk, integral, wall shear and particle Reynolds numbers respectively. Re in [5] is calculated based on root mean square of velocity and Re in [5] is calculated based on Taylor lengths scale. λ refers to aspect ratio of the objects and in [1],[2] λ is measured by considering arm of the objects. St_η is the particle translational stokes number, but in works marked as [1],[2],[3], authors introduced a tumbling Stokes number to evaluate their data. L_f/l_{flow} stands for the ratio of the length of the objects to the flow length scale. In the works marked with [1],[2], L_f is calculated by taking to account one arm of the objects, whereas in [3], equivalent diameter is used.

2

Methodology

Context of this chapter is recently published in:

M. Alipour, M. De Paoli, S. Ghaemi, and A. Soldati. *Long non-axisymmetric fibres in turbulent channel flow. J Fluid Mech, 916, 2021. [3]*

In this chapter experimental facility, particles parameters and image acquisition system are described in §2.1.1, §2.1.2 and §2.1.3, respectively. Moreover, the methodology used to reconstruct and track the fibers is presented in §2.2. This methodology provides us an opportunity to detect the rate of asymmetry of the fibers, in this case measured by the curvature, while they are tracked in time. In this way, we can investigate the effect of curvature on the behaviour of the fibers.

2.1 Experimental setup

We measure experimentally the three-dimensional distribution, orientation and rotation rate of long fibers in a fully-developed, turbulent channel flow. In this section, we describe the experimental apparatus, flow parameters, fiber properties and three-dimensional fiber detection technique used in this study.

2.1.1 Flow apparatus

The experimental facility is the TU Wien Turbulent Water Channel, consisting of a 10 m long water channel, constructed by combining 5 sections of 2 m each, with cross-sectional dimensions of 80×8 cm^2 ($w\times2h$, where h is half channel height). Each section of the channel is equipped with de-airing valves, which allows to remove the bubbles trapped close to the top wall of the channel. The channel is manufactured using Polymethyl methacrylate (PMMA) with thickness of 1.5 cm, which is fully transparent. The experimental setup is sketched in figure 2.1(a). The upper cover of the channel is removable in all sections, and both open and close channel experiments can be performed. In this study, we only consider the close channel configuration with no free surface. The fluid is circulated from the downstream to the upstream reservoir by a pump, and the flow is subsequently driven by gravity. A centrifugal volute pump (maximum flow rate of 147 m^3/h) and a Proline Promag 10D Electromagnetic flowmeter are used. Average temperature of the water is kept at 15°C, which results

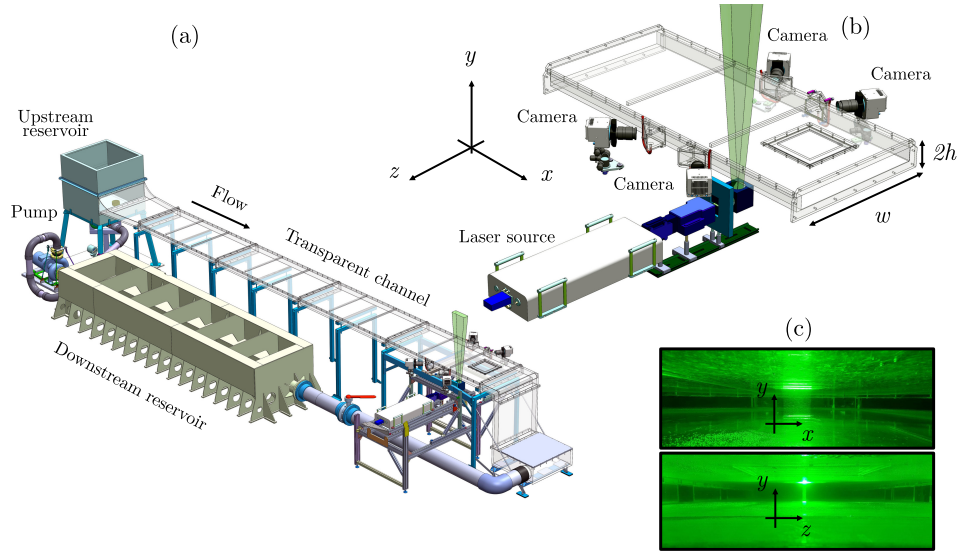

FIGURE 2.1 – Schematic of the TU Wien Turbulent Water Channel and test section. Panel (a) The system consists of two reservoirs at ambient pressure, a centrifugal pump and a rectangular channel (aspect ratio 10). The test section, is located 8.5 m downstream of the channel entrance, to ensure a fully developed turbulent flow. Panel (b) Close-up view of the test section, where an array of four cameras is used to record the 3D motion of the particles. The laser volume, indicated by the green region, is located at the channel mid-span. To reduce the optical image distortion due to astigmatism, cameras look through prisms filled with water. The laboratory reference frame (x, y, z, respectively streamwise, wall-normal and spanwise directions) is also shown. Panel (c) Field of view of the cameras and illumination volume.

in a dynamic viscosity equal to $\mu = 1.138{\times}10^{-3}$ Pa·s [44]. In order to eliminate all vibrations, possibly created by either the pump or the chiller of the laser, both equipments are placed on vibration isolators.

2.1.2 Fiber properties

In this study, the fibers consist of Polyamide 6.6 (PA6.6) Precision Cut Flock (Flockan) with linear density of $\rho_l = 9 \times 10^{-8}$ kg/m (0.9 dtex). The density and cutting length are $\rho = 1.15 \times 10^3$ kg/m^3 and $L_f = 1.2$ mm, respectively, corresponding to a diameter $d_f = \sqrt{4\rho_l/(\rho\pi)} \approx 10$ μm. In figure 2.2, we present a microscopic view of the fibers considered in this study. This observation is important because we used this initially qualitative view to categorise the shape of the fibers in the systematic way. In figure 2.2(a), we show a raw image of a large quantity of the fibers in dry condition. Fibers are very elongated and characterised by a large value of anisotropy ratio, $\lambda = L_f/d_f \approx 120$ and in addition, they are characterised by a small curvature. In figure 2.2(b), we show a limited number of fibers on a white horizontal background. In this view, we can better appreciate the curvature and also more importantly, we can appreciate that all fibers are planar. Finally, from the close up view of figure 2.2(c), fibers seem to present no inflection point. Observing many samples like the ones pre-

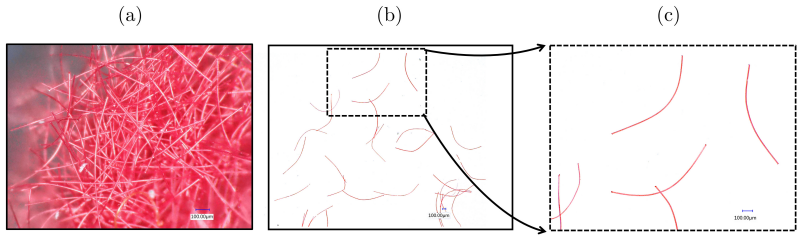

FIGURE 2.2 – Fiber samples. Panel (a) Raw image of a cluster of fibers (microscope view). Panel (b) Close-up view of fibers characterised by different shapes, mainly non-axisymmetric.

sented in figure 2.2, lead us to hypothesise that fibers can be described by a second order polynomial curve. This point together with the methodology used to detect and model the fibers will be further discussed in §2.2.2.
The dimensionless parameter used to characterise the behaviour of particles transported by the flow is the particle Stokes number, St, which quantifies the ratio between the particle relaxation time, τ_f, and the viscous time scale, τ. To estimate the translational relaxation time of the fibers, we use the relaxation time of randomly oriented prolate spheroids. We considered the relation proposed by Bernstein and Shapiro [8], which gives

$$\tau_f = \frac{\rho d^2}{18\mu} \frac{\lambda \ln\left(\lambda + \sqrt{\lambda^2 - 1}\right)}{\sqrt{\lambda^2 - 1}} \ , \tag{2.1}$$

where d, in the instance of anisotropic and axisymmetric particles, is the diameter perpendicular to the symmetry axis. Although fibers used in the present study are not exactly prolate spheroids, Eq. (2.1) can provide a good approximation of their relaxation time. The τ_f computed as in Eq. (2.1) is based on the relaxation time of a spherical particle ($\rho d^2/18\mu$), and corrected for prolate spheroids as function of the fiber aspect ratio, $\lambda = L_f/d_f$.

2.1.3 Three-dimensional imaging

The measurement is carried out in correspondence of the test section, located 8.5 m ($\approx 200h$) downstream the channel entrance, to ensure the fully developed flow condition. The measurement volume ($53.4 \times 53.4 \times 14$ mm^3) is located at the mid-span of the channel. A close-up view of the test section is provided in figure 2.1(b). Illumination comes from the bottom and consists of a thick laser sheet (527 nm, double cavity, 25 mJ per pulse, Litron LD60-532 PIV). The images are recorded using four Phantom VEO 340 L cameras with sensor size of 2560×1600 pixel at 0.8 kHz and each pixel size is 10×10 μm^2. The cameras are located on both sides of the channel and in linear configuration. Side and front view of the measurement volume is depicted in figure 2.1(c). Camera holders are equipped with dampers to remove any possible vibration coming from the channel frame. In order to increase the accuracy of the three-dimensional reconstruction process, we placed the cameras with angles of 35° and 30° with respect to the spanwise axis of the channel. To minimise the optical astigmatism, we used four prisms filled with water at the side walls of the channel.

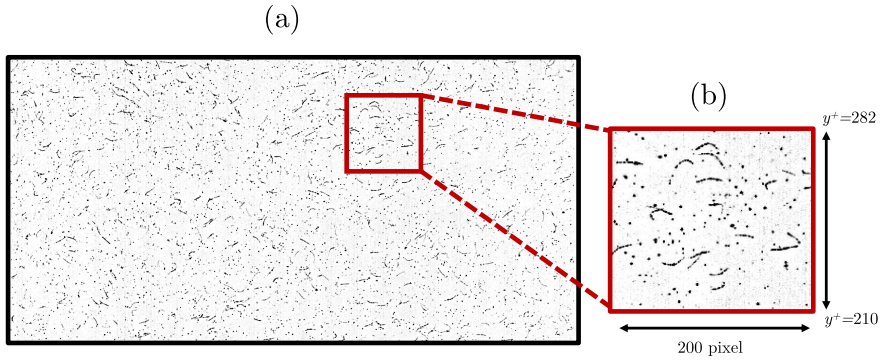

FIGURE 2.3 – Panel (a) Example of raw image referring to a portion of the domain. Curved fibers as well as tracer particles can be identified. Panel (b) Close-up view of a group of fibers. The resolution adopted is sufficient to properly characterise the fibers, which consist of tens of pixel.

Finally, the cameras are equipped with Scheimpflug adaptors and objective lenses with focal length $f = 100$ mm.

Prior to reconstruction of the measurement volume, raw images were pre-processed using time and spatial filters. First step of the image pre-processing consists of removing the background noise by subtracting the minimum intensity value of the dataset from each image. Afterwards, a spatial filter is applied to the images by subtracting the minimum intensity within a kernel of five pixel from each pixel. Finally, the intensities were normalised by the average intensity within a kernel of 300 pixel. These steps were essential to increase the signal-to-noise ratio of the images and to improve the quality of the reconstruction process. A three-dimensional calibration target with size of 58×58 mm^2 was used to map the coordinate system of the illuminated volume on the image. Afterwards, a third-order polynomial function was used for the mapping process. Initial standard deviation of the calibration fit was in the scale of 0.3 pixel, which eventually reduced to values smaller than 0.03 pixel (averaged on all camera views) by applying the Volume Self-Calibration (VSC) algorithm [89]. VSC was done by assuming $8 \times 8 \times 5$ (x, y, z) sub-volumes and resulted in average disparity error of approximately 0.02 pixel, which is 5 times smaller than recommended threshold for VSC accuracy [89]. In order to implement the VSC, flow must be seeded with spherical shaped tracers. Multiplicative Algebraic Reconstruction Technique (MART) [29] is used to reconstruct the 3D distribution of light intensity from 2D images of tracer particles and fibers. Since in this study we use MART to reconstruct both unladen and fiber-laden flows and the VSC process is a main step of the calibration to be done before MART, we seeded the water with tracers prior to dispersing the fibers into the water. An example of raw image of fiber-laden flow containing both fibers and tracer is shown in figure 2.3. Each snapshot of fiber-laden recording contains, on average, approximately 1000 fibers and the corresponding volume fraction and concentration are $O(10^{-6})$ and 0.025 mm^{-3}, respectively. Therefore, it is reasonable to consider that the one way coupling assumption holds. All processes of image acquisition and single phase velocimetry have been carried out using Davis (LaVision GmbH).

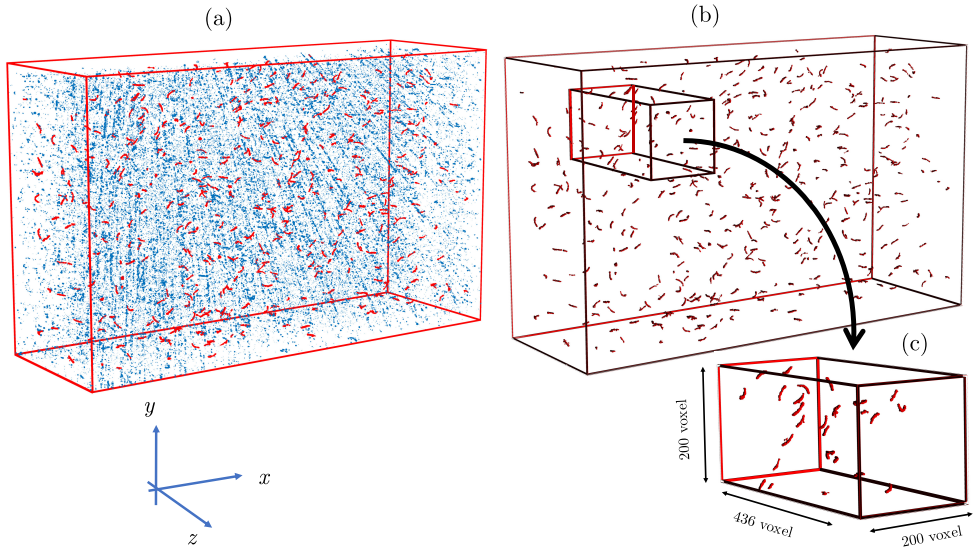

FIGURE 2.4 – Panel (a) Three-dimensional light intensity distribution is obtained using MART [29], and corresponding voxels are shown. Panel (b) After masking, fibers (red voxel) are discriminated from the other objects, e.g. tracers, noise and ghost particles (blue voxel). Panel (c) Close up view of a small portion of the domain (size is reported). We observe that, although fibers are characterised by a complex shape, they are well captured by the reconstruction and discrimination processes proposed here.

2.2 Fiber detection and tracking

In this study, we use MART to reconstruct the 3D light intensity distribution of both unladen and fiber-laden flows. To discriminate the fibers, we developed a MATLAB based in-house code, which is described in §2.2.1. Fibers modelling is discussed in §2.2.2 and §2.2.3. Finally, fiber tracking and calculation of rotation rates are analysed in §2.2.4 and §2.2.5, respectively.

2.2.1 Phase discrimination

The process of fibers discrimination is used to distinguish the fibers from the tracers and the other spurious, reconstructed objects, and consists of a combination MART and volumetric masking. An example of discrimination process is shown in figure 2.4. First, the three-dimensional light intensity distribution, consisting of normalised intensities (i.e. intensity has values from 0 to 1), is obtained from the MART reconstruction process. The three-dimensional matrix of light intensities is binarised [figure 2.4(a)], according to a threshold value set to 0.05. All the groups of contiguous voxels with unitary value are identified as a cluster. Then, an effective length of the cluster, L_{eff}, is computed by which we can discriminate the fibers (red colored clusters) from tracers and optical noises (blue colored clusters) as shown in figure 2.4(b) .
We describe here the process of identification of the effective cluster length, L_{eff}. We

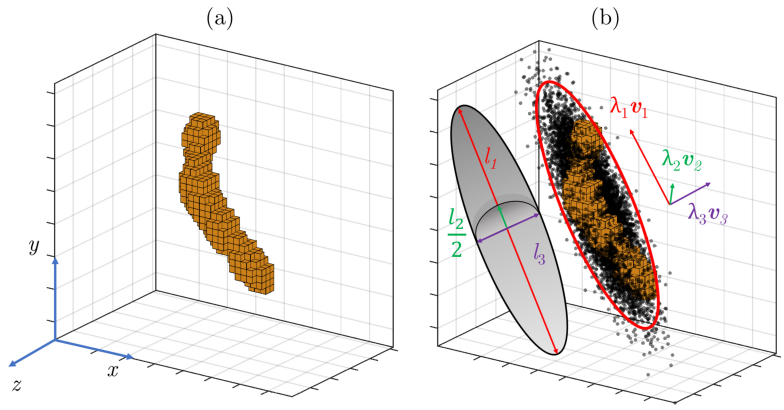

FIGURE 2.5 – Fiber consisting of the binarized voxel values is shown in panel (a). Scatter data [black bullets in panel (b)] represent the MND having mean $\boldsymbol{\mu}$ and covariance $\mathbf{C}$. The three-dimensional distribution of these data defines an ellipsoid with axes length l_i. The directions of the principal axis of the ellipsoid (eigenvectors $\mathbf{v}_i$ of the covariance matrix) are also shown. The eigenvectors are rescaled according to their correspondent eigenvalues (λ_i), so that the product $\lambda_i \mathbf{v}_i$ is proportional to the ellipsoid axis length l_i.

consider the binarised voxel distribution and associated to a fiber [figure 2.5(a)]. Since the position of each voxel of the fiber in the three-dimensional space (x, y, z) is known, the covariance matrix of the fiber can be computed as:

$$\mathbf{C} = \begin{bmatrix} \mathrm{cov}(x,x) & \mathrm{cov}(x,y) & \mathrm{cov}(x,z) \\ \mathrm{cov}(y,x) & \mathrm{cov}(y,y) & \mathrm{cov}(y,z) \\ \mathrm{cov}(z,x) & \mathrm{cov}(z,y) & \mathrm{cov}(z,z) \end{bmatrix}, \tag{2.2}$$

where $\mathrm{cov}(x, y)$ is the covariance of x and y defined as

$$\mathrm{cov}(x,y) = \frac{1}{n}\sum_{i=1}^{n}(x_i - \overline{x})(y_i - \overline{y}), \tag{2.3}$$

and $\overline{x}$ is the mean value of the x. The very same procedure applies to all other elements of $\mathbf{C}$. Then, a Multivariate Normal Distribution (MND) corresponding to the mean $\boldsymbol{\mu} = [\overline{x}, \overline{y}, \overline{z}]$ and the covariance $\mathbf{C}$ is generated [45]. Scattered data representing the MND are shown as black symbols in figure 2.5(b). The three-dimensional distribution of these points defines an ellipsoid with axes length l_i.

A correspondence exists between this ellipsoid and the properties of the matrix $\mathbf{C}$. Indeed, the eigenvectors $\mathbf{v}_i$ of the matrix $\mathbf{C}$ are oriented in the directions of the principal axis of the ellipsoid. Moreover, $\lambda_i \mathbf{v}_i$, i.e. the eigenvectors rescaled according to their correspondent eigenvalues (λ_i), are proportional to the ellipsoid axis length $l_i = 2\sqrt{\alpha \lambda_i}$, where α is a scale factor. Finally, the effective length L_{eff} used as threshold for the discrimination process, is defined as the length of the major axis of the ellipsoid, $L_{\mathrm{eff}} = l_1$.

Clusters with effective length in the range of $20 < L_{\text{eff}} < 40$ voxel [red voxels in figure 2.4(a)] are identified as fibers, and all remaining clusters [blue voxels in figure 2.4(a)] are removed. The above-mentioned range for the effective length is set by considering the fibers size. By this masking, the majority of the tracers is removed and only large clusters of voxels remain [figure 2.4(b)], which mostly represent the real fibers. In some unlikely cases, these clusters may still consist of spurious objects. However, they do not persist over long time periods and can be eliminated by removing the clusters tracked over a short number of snapshots.
We would like to clarify one point here: although the diameter of the fiber is in the scale of the pixel size of the censor, the actual diameter size of the fibers in terms of voxels are bigger than one voxel. The particle image diameter is function of geometrical and image diffraction diameter, therefore its reconstructed diameter could be bigger than magnified geometrical diameter, detailed description is provided by Scarano [76]. Based on the imaging parameters used in our experiments and reported in table. 3.1, minimum fiber diameter in terms of voxel is 3-4 voxels.

2.2.2 Fiber modeling

To quantify the fibers concentration, orientation and rotation rate, after discrimination each fiber has to be associated with the representing coordinates in the three-dimensional space. To this aim, we developed a physically-grounded geometrical model for the fibers. We consider a rigid and non-axisymmetric fiber of length L_f and we assume that the fibers are bent but not twisted. This hypothesis is motivated by observations, and represents the ground of the modeling process proposed. As a consequence, one can show that the fiber lays on a plane, i.e. it can always exist in at least one plane, Π, in the three-dimensional space, (x, y, z), that contains the fiber. An example of voxel distribution, discriminated as in §2.2.1, is sketched in figure 2.6(a), where the colour of the voxels refers to the reconstructed light intensity. The geometrical description of the fiber [red line in figure 2.6(a)] is obtained through a process of modeling, consisting of three main steps:

1. Preliminary determination of the fiber orientation: we consider the cluster of voxel identified as a fiber in the discrimination process. We consider the coordinates of the voxels located at two ends of the fibers and then find the distance between these two points. The direction of the laboratory reference frame (x, y or z) along which this difference is maximum is preliminarily considered as the orientation of the fiber. In figure 2.6(a), the fiber orientation is x, and we define x as the preliminary "fiber direction".

2. Identification of the fiber cross section centers: we consider the light intensities of the voxels defining the fiber. We group the voxels according to the planes perpendicular to the fiber direction. Therefore, each plane represents (approximately) a cross section of the fiber. We determine the center of each cross section as the averaged voxel coordinate (x, y, z) weighted on the light intensity of the voxels. In the fiber shown in figure 2.6(a), the centers of the cross sections, (y, z) planes, are found. These centers are explicitly indicated as red stars [figure 2.6(a)].

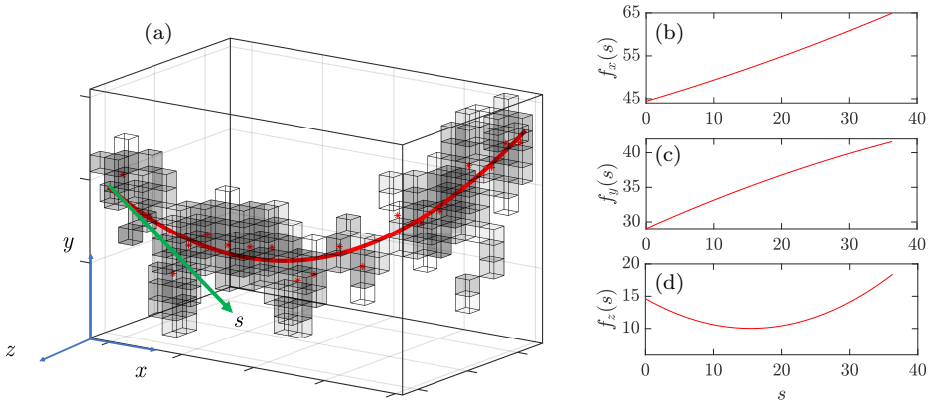

FIGURE 2.6 – (a) Example of fiber reconstruction (red curve) obtained from light intensity distribution. Voxels, here represented as cubes, are coloured according to their light intensity, from lower (white) to higher (black). The laboratory reference frame $(x, y, z$, blue vectors) is shown, as well as the origin and direction of the arc length coordinate, s (green vector), which is used to perform the reconstruction. (b-d) Coordinates of the voxels belonging to the fibers are approximated by three functions (f_x, f_y, f_z) obtained by fitting the coordinates of the centers, as defined in §2.2.2 [red stars in panel (a)], as a function of the curvilinear coordinate, s.

3. Definition of the fiber major axis: finally, the fiber axis is defined as the best-fit of the centers defined above. To this aim, we define the arc length coordinate, s, with origin and end in the first and last cross sectional centers, so that $0 \leq s \leq L_f$. To identify the fiber position in space, for each direction x_i (where x_i stands for x, y or z), we find the function f_{x_i} that best fits in a least-square sense the coordinates of the centers. In this way, the functions f_{x_i} required to approximate the fibers coordinate x_i as a function of the arc length coordinate, s, are obtained [figures 2.6(b)-(d)].

   In particular, for the present case we set the functions f_{x_i} to be second-order polynomials, so that:

$$f_{x_i} = a_i s^2 + b_i s + c_i \ . \tag{2.4}$$

   One can show analytically that this assumption is consistent with the initial hypothesis that the fiber is contained on a plane. This assumption is also consistent with direct observations of the fibers (see §2.2). Indeed, in figure 2.2(b) and figure 2.2(c) fibers seem planar and without any inflection point.

The fibers coordinates, f_{x_i}, can be written in matrix form as

$$\mathbf{x}_f = \begin{bmatrix} f_x \\ f_y \\ f_z \end{bmatrix} = \begin{bmatrix} a_1 & b_1 & c_1 \\ a_2 & b_2 & c_2 \\ a_3 & b_3 & c_3 \end{bmatrix} \begin{bmatrix} s^2 \\ s \\ 1 \end{bmatrix} = \mathbf{A}\mathbf{s} \ , \tag{2.5}$$

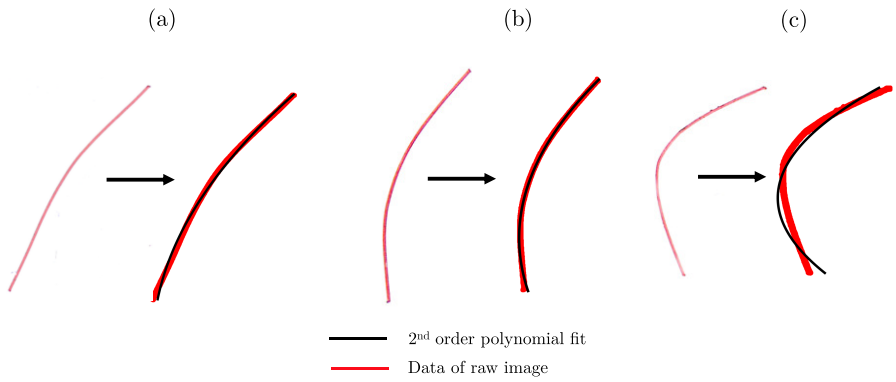

FIGURE 2.7 – Fiber samples. Panel (a)-(c) Three different classes of fibers, classified according to their curvature, are shown. The fibers (left, red objects taken from microscope images) are well fitted by the second order polynomials (right, black objects obtained from fitting). This assumption is required to employ the method proposed here.

where $\mathbf{x}_f$ is the approximated fiber coordinates vector, $\mathbf{A}$ is the matrix of the coefficients (a_i, b_i, c_i) and $\mathbf{s}$ contains the arc length coordinate vector. Therefore, the modeled fiber is fully defined by the matrix $\mathbf{A}$ and the length L_f. An example of the reconstruction process performed for fibers of different shape is shown in figure 2.7. In particular, we observe in figure 2.7(a-b) that the fibers (left, red objects taken from microscope images) are well fitted by second order polynomials (right, black objects obtained from fitting).

The proposed fitting method is based on the assumption that the fiber is a parabolic segment. However, even in cases in fiber are not precisely parabolic segments, like the case shown in figure 2.7(c), in which fiber curvature exhibits strong gradients, the proposed fitting method supplies a reasonably accurate approximation for the shape of the real fiber.

The next step required for the fiber tracking consists of identifying the fibers center of mass and orientation. We consider now the fiber sketched in red in figure 2.8(a). The projection of the fiber on the reference planes is shown (blue lines) as well as the center of mass of the fiber $\mathbf{G} = (x_G, y_G, z_G)$, where

$$x_{i,G} = \frac{1}{L_f} \int_0^{L_f} x_i(s)\, \mathrm{d}s \ , \tag{2.6}$$

where x_i stands for x, y or z. The plane Π containing the fiber is defined by the equation

$$\mathbf{n} \cdot [\mathbf{e_1}(x - x_G) + \mathbf{e_2}(y - y_G) + \mathbf{e_3}(z - z_G)] = 0 \ , \tag{2.7}$$

where $\mathbf{e_i}$ are the unit vectors of the laboratory reference frame and $\mathbf{n}$ is the unit vector perpendicular to Π. Given three points of the fiber ($\mathbf{A}$, $\mathbf{B}$ and $\mathbf{C}$), $\mathbf{n}$ is determined as

$$\mathbf{n} = \begin{bmatrix} (y_B - y_A)(z_C - z_A) - (z_B - z_A)(y_C - y_A) \\ (x_C - x_A)(z_B - z_A) - (x_B - x_A)(z_C - z_A) \\ (x_B - x_A)(y_C - y_A) - (y_B - y_A)(x_C - x_A) \end{bmatrix} . \tag{2.8}$$

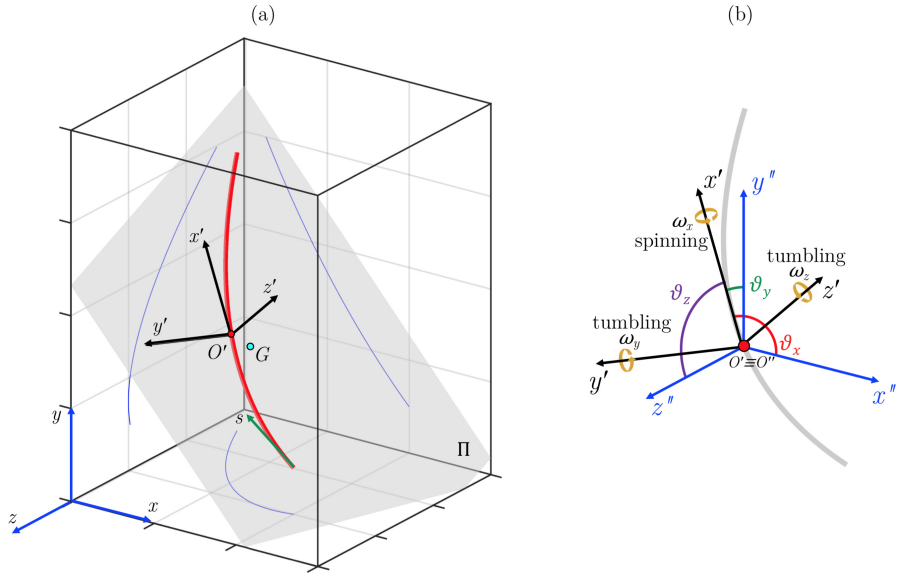

FIGURE 2.8 – (a) Non-axisymmetric fiber (red line) laying on the plane Π. The inertial frame of reference, with axes labeled as x, y and z, remains fixed in space and time. The fiber frame of reference, centered in the fiber midpoint located at $s = L_f/2$ (O', red bullet), has axes (x', y', z') aligned with the principal directions of the inertia tensor. The projection of the fiber on the three planes is also shown (blue lines). Note that, in general, the center of mass of the fiber (G, cyan bullet) may be external to the fiber. (b) Angles defined between the reference frame of the fiber ($O'x'y'z'$) and the reference frame of the laboratory translated to the midpoint O' ($O''x''y''z''$).

Following Voth and Soldati [85], we define the fiber reference frame using the inertia tensor

$$\mathbf{I}_{ij} = \rho_l \int_0^{L_f} \left[(f_{x_i} - x_{i,G})^2 \delta_{ij} - (f_{x_i} - x_{i,G})(f_{x_j} - x_{j,G}) \right] \, \mathrm{d}s, \tag{2.9}$$

with ρ_l [kg/m] the linear density of the fibers and δ_{ij} the Kronecker delta. Therefore, we align the reference frame of the fiber ($O'x'y'z'$) with the normalised eigenvectors of $\mathbf{I}$. Note that the eigenvalues of $\mathbf{I}$ are real and positive and correspond to the principal inertia moments of the fiber, I_1, I_2 and I_3. In the present case, one eigenvalue is much smaller than the other two and we align x' with the correspondent eigenvector. Similarly, y' and z' are aligned with the second and third eigenvector respectively. When the fiber is curved, x' and z' belong to Π whereas y' is aligned with $\mathbf{n}$.

The system is represented in figure 2.8(b). Three rotations (and the corresponding rotation matrices) are required to identify the orientation of the fiber with respect to the lab reference frame. To this aim, we use the quaternions formulation [50]. We consider the unit vectors of the reference frame $O'x'y'z'$ and $O''x''y''z''$, respectively $\mathbf{e'_1}, \mathbf{e'_2}, \mathbf{e'_3}$ and $\mathbf{e''_1}, \mathbf{e''_2}, \mathbf{e''_3}$. The angle ϑ_x is defined here as the angle required to align

$\mathbf{e}_1''$ with $\mathbf{e}_1'$. We compute the unit quaternion $\mathbf{q}$ as:

$$\mathbf{q} = \begin{bmatrix} q_s \\ q_x \\ q_y \\ q_z \end{bmatrix} = \frac{1}{\sqrt{(q_s^*)^2 + (q_x^*)^2 + (q_y^*)^2 + (q_z^*)^2}} \begin{bmatrix} q_s^* \\ q_x^* \\ q_y^* \\ q_z^* \end{bmatrix} \tag{2.10}$$

with $q_s^* = 1 + \mathbf{e}_1'' \cdot \mathbf{e}_1'$ and $[q_x^* \; q_y^* \; q_z^*]^T = \mathbf{e}_1'' \times \mathbf{e}_1'$. The rotation matrix associated to the quaternion $\mathbf{q}$ is

$$\mathbf{R}_{\vartheta_x} = \begin{bmatrix} 1/2 - q_y^2 - q_z^2 & q_x q_y - q_s q_z & q_x q_z + q_s q_y \\ q_x q_y + q_s q_z & 1/2 - q_x^2 - q_z^2 & q_y q_z - q_s q_x \\ q_x q_z - q_s q_y & q_y q_z + q_s q_x & 1/2 - q_x^2 - q_y^2 \end{bmatrix}, \tag{2.11}$$

and we have that $\mathbf{e}_1'' = \mathbf{R}_{\vartheta_x} \mathbf{e}_1'$. The rotation angle is finally determined as

$$\vartheta_x = 2\text{atan2}\left(\sqrt{q_x^2 + q_y^2 + q_z^2}, q_s\right). \tag{2.12}$$

Following the same procedure, the two rotation matrices $\mathbf{R}_{\vartheta_y}$, $\mathbf{R}_{\vartheta_z}$ and the corresponding angles are determined.

2.2.3 Curvature

The model adopted to describe the fiber, as discussed in §2.2.2, makes it to lie on the plane containing the fiber, Π, which is fully determined by the normal vector $\mathbf{n}$. The coordinates of the fiber can be expressed with respect to a specific reference frame so that the two axis (x', y') lie on Π and the third (z') axis corresponds to $\mathbf{n}$. As a result, the coordinates of the fiber with respect to this reference frame are

$$\mathbf{x}_f' = \begin{bmatrix} f_{x'} \\ f_{y'} \\ f_{z'} \end{bmatrix} = \begin{bmatrix} a_1' & b_1' & c_1' \\ a_2' & b_2' & c_2' \\ 0 & 0 & 0 \end{bmatrix} \begin{bmatrix} s^2 \\ s \\ 1 \end{bmatrix}, \tag{2.13}$$

consisting of the projection of the parametric curve defined by Eq. (2.5), with a_i', b_i', c_i' suitable coefficients (these coefficients are obtained applying an appropriate rotation $\mathbf{R}$ to the matrix of coefficients, $\mathbf{A}$). The local curvature, $\kappa_l(s)$, of the two-dimensional parametric function defined in Eq. (2.13) is given by:

$$\kappa_l(s) = \frac{f_{x'}' f_{y'}'' - f_{x'}'' f_{y'}'}{\left[\left(f_{x'}'\right)^2 + \left(f_{y'}'\right)^2\right]^{3/2}}, \tag{2.14}$$

where the symbols $'$ and $''$ indicate the first and second derivative with respect to the coordinate s. Therefore, using Eq. (2.13), the local curvature reads:

$$\kappa_l(s) = \frac{2(a_2' b_1' - a_1' b_2')}{\left[\left(2a_1' s + b_1'\right)^2 + \left(2a_2' s + b_2'\right)^2\right]^{3/2}}, \tag{2.15}$$

and the unit vectors locally tangent, $\mathbf{T}(s)$, and normal, $\mathbf{N}(s)$, to the fiber in the reference frame of the plane are (see figure 2.9):

$$\mathbf{T}(s) = \begin{bmatrix} 2a_1's + b_1' \\ 2a_2's + b_2' \\ 0 \end{bmatrix} \quad , \quad \mathbf{N}(s) = \frac{1}{\kappa_l(s)} \begin{bmatrix} 2a_1' \\ 2a_2' \\ 0 \end{bmatrix} . \tag{2.16}$$

In the following, we will characterise the behaviour of the fibers according to their mean curvature, defined here as:

$$\kappa = \frac{1}{L_f} \int_0^{L_f} |\kappa_l(s)| \, \mathrm{d}s \, . \tag{2.17}$$

We estimate the length of the fiber by computing the Probability Density Function (PDF) of the length of all fibers tracked in our experiments [figure 2.10(a)], where the fiber length corresponds to the mean length measured in all time instances of the track for each fiber. The representative fiber length is chosen by referring to the peak of the PDF corresponding to $\overline{L_f} = 1.26$ mm, which is slightly higher than the mean length of the fibers based on manufactured nominal length (1.2 mm), perhaps due to accuracy of the cutting process. To examine the accuracy of the length reconstruction, we plot the PDF of standard deviation (σ) of the fibers lengths measured within each track for all fibers in figure 2.10(b). Most probable standard deviation of the measured fiber length corresponds to 0.65 mm, representing a deviation close to 5% of the nominal length of the fibers. The mean curvature κ is normalised by κ_0, which is calculated by considering the curvature of a arc of half circle with length equal to the mean length of the fibers, i.e. $\kappa_0 = \pi/\overline{L_f} = 2.53$ mm^{-1}. Finally, fibers are classified according to their dimensionless curvature, $\kappa^* = \kappa/\kappa_0$, so that straight fibers correspond to $\kappa^* = 0$ and semicircumference shaped fibers to $\kappa^* = 1$. The PDF of κ^* of all fibers tracked in the experiments is reported in figure 2.10(c). We observe that the fibers used in this study are far from being considered as straight. In order to be able to characterise their behaviour as function of their curvature, we arbitrarily divided the data set into different classes consisting of ranges of curvature. By this classification, we analyse the effect of curvature on the main dynamics of the fibers.

2.2.4 Tracking

The tracking process consists of the identification of the same fiber in two consecutive frames. After fiber discrimination, reconstruction and modelling, the center of mass of the fiber (x_G, y_G, z_G) is identified in the first instant. In the subsequent instant, the presence of the center of mass of a fiber within a distance of 5 voxel from the previous one is searched. The threshold radius of 5 voxel is set according to the estimated flow velocity. If a center of mass is found within this range, the fiber in two consecutive frames is tracked. The behaviour of a single fiber is shown in figure 2.11. The measured position of the center of mass [symbols in figure 2.11(a)-(c)] experiences fluctuations in all directions. However, the spanwise and wall-normal components are more affected due to the short displacement between two consecutive snapshots. This effect is even more pronounced in the instance of the fiber orientation angles, $\vartheta_x, \vartheta_y, \vartheta_z$ [symbols in figure 2.11(d)-(f)]. Since these fluctuations have negative effects on the calculation

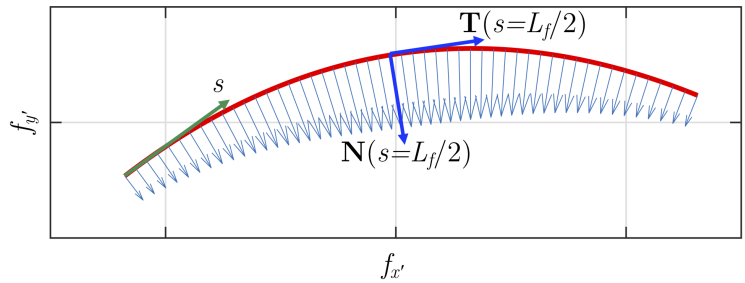

FIGURE 2.9 – Projection of the fiber on the plane Π. The unit vectors normal, $\mathbf{N}(s)$, and tangent $\mathbf{T}(s)$ at the midpoint of the fiber ($s = L_f/2$) are also shown. The normal vectors (blue) are proportional to the local curvature, κ_l.

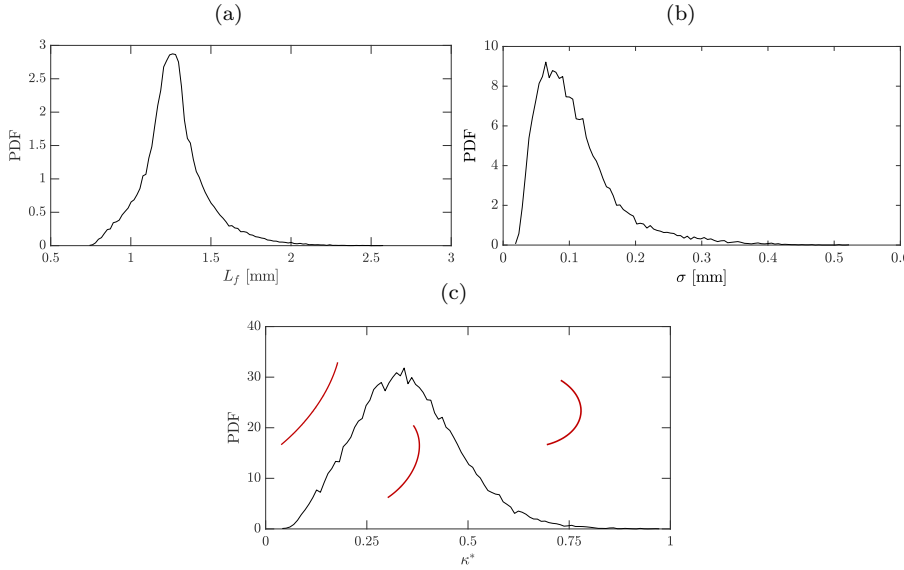

FIGURE 2.10 – PDF of length (a) and standard deviation (σ) (b) normalised curvature of the fibers reconstructed in this study (c) of the fibers reconstructed in this study. Most probable fiber length measured corresponds to 1.26 mm, close to the nominal cutting value ($L_f = 1.2$ mm). Most probable standard deviation of the measured fiber length corresponds to 0.65 mm. Most probable fiber shape corresponds to the normalised curvature value $\kappa^* = 0.31$.

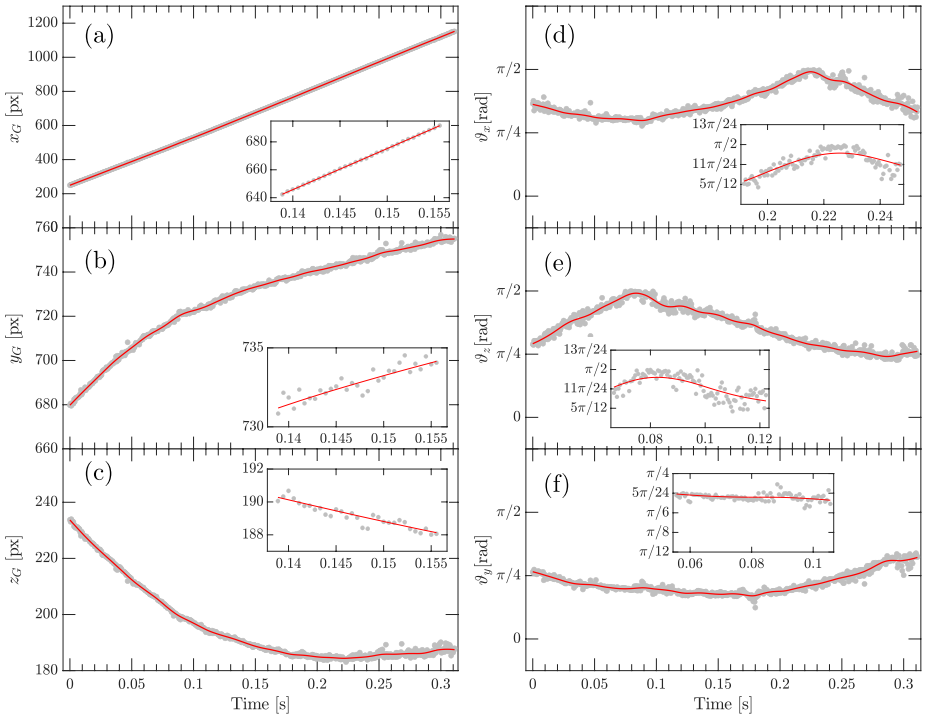

FIGURE 2.11 – Trajectory of the center of mass $[x_G, y_G, z_G$, panels (a)-(c)] and fiber orientation $[(\vartheta_x, \vartheta_z, \vartheta_y$, panels (d)-(f)] of the fiber with respect to the snapshot number. Data measurements (grey symbols) are well resolved in time (see insets), and are filtered in time using a second-order polynomial (red lines).

of the velocity components, location and orientation of the fibers are filtered in time using a second-order polynomial. This filter is sufficient to capture the fiber motion and to reduce the noise from the experimental measurements [72]. The window size of the filter is set to approximately 2.8 τ and only fibers tracked longer than this time window are considered for the statistics. Effect of kernel size of the filtering on the statistics is thoroughly analysed in §5.2. Finally, the time derivatives of the filtered quantities are obtained from the coefficients of the polynomials. The effect of the time-filtering is shown in figure 2.11 (red lines).

2.2.5 Tumbling and spinning rates

In case of axisymmetric particles, rotation rates are decomposed into a component along the symmetry axis, called spinning, and two components perpendicular to the symmetry axis, defined as tumbling [85]. To compute the angular velocities required to identify spinning and tumbling rates, a different set of angles is used compared to that introduced in Sec. 2.2.2. In particular, we use the Euler angles corresponding to a specific rotation matrix. The columns of this matrix are the eigenvectors of the inertia tensor. We consider the reference frame of the fiber, $(O'x'y'z')$, indicated in figure 2.8(b): with the Euler angles, three angular velocities can be computed, ω_x, ω_y and ω_z, which are aligned with the axes x', y' and z', respectively.
Following Voth and Soldati [85], we define the solid body rotation rate, $\mathbf{\Omega} = \boldsymbol{\omega}_x + \boldsymbol{\omega}_y + \boldsymbol{\omega}_z$. In the instance of axisymmetric particles, a unit vector $\mathbf{p}$ aligned with the symmetry axis is used to define the spinning and tumbling rates. In our case, since in general the fiber is non-axisymmetric, we arbitrarily align $\mathbf{p}$ with x'. We can rewrite the solid body rotation in terms of squared spinning ($\mathbf{\Omega}_s$) and squared tumbling ($\mathbf{\Omega}_t$) components, so that $\mathbf{\Omega} = \mathbf{\Omega}_s + \mathbf{\Omega}_t$, where

$$\mathbf{\Omega_s} = (\mathbf{\Omega} \cdot \mathbf{p})\mathbf{p} = \omega_x \mathbf{p} \quad \text{and} \quad \mathbf{\Omega}_t = \mathbf{\Omega} \times \mathbf{p} \ . \tag{2.18}$$

As a results, one can show that $\Omega_t \Omega_t = (\mathbf{\Omega}_t \cdot \mathbf{\Omega}_t) = (\omega_y^2 + \omega_z^2)$.

2.3 Summary

In this section we summarise the methodology of fiber reconstruction and tracking that is used in this study. We employ a Multiplicative Algebraic Reconstruction Technique (MART) [29] to find the 3D distribution of light intensity obtained from 2D images. The images consist of tracers and fibres and thus, after MART reconstruction is obtained, a discrimination process is required to identify the clusters of voxel corresponding to fibres. The fibres are non-axisymmetric objects that have a complex shape. Therefore, their geometry is modelled to find a simple mathematical description that allows the determination of their orientation. Finally, the fibres are followed in subsequent snapshots and tracked to find their trajectory, velocity, and rotation rate. The process of discrimination, modelling and tracking, is summarised in figure 2.12. A description of the main steps follows. Each snapshot of the experiment consists of four images obtained simultaneously from the cameras arranged as in figure 2.1. The recorded images contain a two-dimensional distribution of light intensities, corresponding to both fibres and tracer particles. One snapshot obtained from 4 cameras is

shown in figure 2.12(a-1)-(a-4). After few pre-processing operations (see also §2.1.3), the images are analysed to find the three-dimensional matrix of light intensities via MART reconstruction [figure 2.12(b)]. For this purpose DaVis 10 (LaVision GmbH) is used. Location (spatial coordinates) and light intensity of the voxel corresponding to fibres and tracers, respectively red and blue objects in figure 2.12(b), are known. Due to the presence of optical noise, not all the cluster of the reconstructed voxels represent the fibers, therefore a discrimination process is essential. In this step, by means of an in house-code, we discriminate the fibers and detect their position in space. Each cluster of voxel is analysed: The size (maximum length) of the clusters is identified and those that do not exceed a specific size threshold are removed. As a result, only the larger clusters are kept, as shown in figure 2.12(c). Finally, each cluster is examined to determine the best-fitting second-order curve used to model the fiber.

The choice of second order is based on physical and geometrical observations. In particular, from microscope images [figure2.2(a)], one can observe that fibers present a nearly symmetric and planar geometry. The fitting process, which is shown in figure 2.12(d), is based on the curvilinear coordinate s, with $0 \leq s \leq L_f$. The polynomial curve obtained is used to determine orientation, center of mass and curvature of each fiber. In particular, the reference frame of the lab translated to the midpoint of the fiber ($O''x''y''z''$) is determined. The natural reference frame of the fiber ($O'x'y'z'$), i.e. a local reference frame centered in the midpoint of the fiber and aligned with the eigenvectors of the inertia tensor, is also determined and used as reference to discuss the orientation of the fibers. In addition, the rotation rates experienced by the fibers with respect the reference frame $O'x'y'z'$, known as spinning and tumbling, are determined. Fibers orientation angles and rotation rates are defined as in figure 2.12(e).

When the geometry of the fiber is determined, a local value of curvature $\kappa_l(s)$ is obtained for all values of s considered. Then, the mean value of curvature computed over the entire fiber length (κ) is determined. Finally, it is normalised by the curvature $\kappa_0 = \pi/L_f$, i.e. the curvature of a fiber having length L_f and shape of half a circle, and the dimensionless curvature $\kappa^* = \kappa/\kappa_0$ is obtained. This definition suggests that the normalised curvature is $\kappa^* = 0$ for straight fibers and $\kappa^* = 1$ for semi-circumference shaped fibers.

The above mentioned procedure is iterated over subsequent snapshots to track the fibers and compute velocity and rotation rates. First, the fiber is identified in two consecutive frames by searching within a sphere of radius five voxel within the position of the fibers at the first snapshot. The measurements are time-resolved, and the displacement of the fibers between two consecutive frames is less than four voxel. After tracking the fiber over at least 2.8 τ consecutive snapshots, trajectories and orientations are filtered (second-order polynomial filtering) to remove spurious fluctuations, and then the statistics are computed. Effect of kernel size of the filtering on the statistics is thoroughly analysed in §5.2. This approach is considered a good compromise to capture the fibers dynamics and to reduce the noise from the experimental measurements [72]. The window size of the filter is set to be approximately 2.8 τ^+ and only fibers tracked longer than this time window are considered for the statistics. This window size is used for statistics shown in §3 and §4, while in §5.2 adaptive filtering is introduced and effect of kernel size of the filtering on the statistics is thoroughly

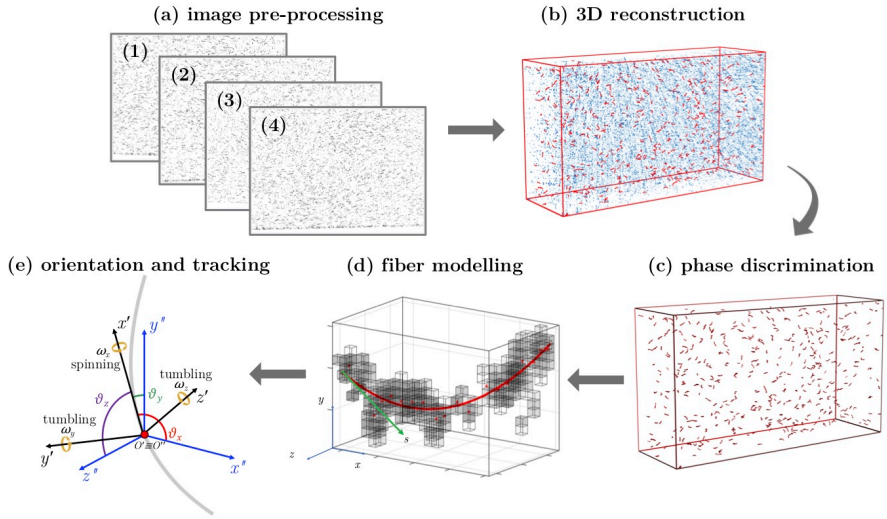

FIGURE 2.12 – Summary of the methodology adopted to identify the location and orientation of the fibers. Each snapshot consists of four images (a) that are pre-processed and used to obtain the 3D light intentisty distribution (b), consisting of tracers (blue) and fibers (red). Each cluster of voxel large than a specific threshold is identified as a fiber (c), and the geometry of it is determined (d). Finally, the local reference frame of the fibers is found, and the orientation with respect to the lab reference frame is obtained (e).

analysed .

3

Effect of Curvature

Context of this chapter is recently published in:

M. Alipour, M. De Paoli, S. Ghaemi, and A. Soldati. *Long non-axisymmetric fibres in turbulent channel flow. J Fluid Mech, 916, 2021. [3]*

In this chapter, we analyze the orientation and rotation rate of the fibres according to their curvature at shear Reynolds number, $\mathrm{Re}_\tau = 360$. Experimental properties are discussed in detail in §3.1. Results of concentration and stream-wise velocity are provided in §3.1.2 and orientation statistics are shown in §3.1.3. In addition, we have been able to compare the tumbling rate of our long non-axisymmetric fibres with previous solutions for curved ellipsoids in simple shear flow. This solution is provided by solving numerically the autonomous system of ordinary differential equations for the Euler angles of curved ellipsoids in laminar shear flow, introduced by Hinch and Leal [35]. These results are shown in §3.1.4.

3.1 Experimental setup

In all experiments, a constant flow rate of 39.6 m^3/h has been chosen, corresponding to a bulk velocity of 0.172 m/s and a bulk Reynolds number based on channel full height ($2h$) of $Re_b = 12500$. The shear velocity of the unladen flow is $u_\tau = 10.2$ mm/s, which gives a friction Reynolds number $Re_\tau = u_\tau h/\nu = 360$, where ν is the kinematic viscosity of water at the temperature of 15°C. Viscous time and length scales of the flow are $\tau = \nu/u_\tau^2 \approx 11$ ms and $\delta = h/Re_\tau \approx 110$ μm, respectively. Kolmogorov time and length scale of the flow at the center of the channel are computed as $\tau_k = (\tau^2/\epsilon_d^+)^{0.5} \approx 220$ ms and $l_k = (\delta^4/\epsilon_d^+)^{0.25} \approx 500$ μm, where ϵ_d^+ is the turbulent dissipation in wall units obtained from the DNS database. Relative length and diameter of the fibers to the length scales of the flow, L_f/l_η, L_f/δ, d_f/l_η and d_f/δ, are equal to 2.38, 10.58, 0.02 and 0.09, respectively. In the present study, the relaxation time of the fiber is $\tau_f = 3.5$ μs which is obtained by using Eq. 2.1, corresponding to $St = 0.003$. In the center of channel, the Kolmogorov time scale should be used to estimate the Stokes number rather than viscous time scale. As a result, the particle Stokes number based on the Kolmogorov time scale at the channel center is 1.54×10^{-4}. We observe that in both cases the Stokes number is small enough to neglect any possible inertial effect.
In the following, we provide an estimate of the maximum deformation that fibers can

experience. To this aim, we assume a simplified flow configuration in which a straight fiber is cylindrical, blocked on one end and free to move on the other end (cantilever beam). For simplicity, we consider the flow as uniform, perpendicular to the fiber axis and characterised by a velocity u_τ. We choose this penalizing configuration to show that, also in presence of critical conditions, the deformation experienced by the fiber is negligible, and that fibers can be considered as rigid objects. We assume that the fiber Young's modulus is $E = 2.5$ GPa [i.e. half of that measured for fibers having diameter 20μm, 15]. The Reynolds number of the fiber, $Re_f = u_\tau d_f/\nu \approx 0.09$ gives a drag coefficient $C_D = 66.1$ [82]. As a result, the force acting on the fiber is $F_D = C_D \rho u_\tau^2 L_f d_f/2 = 4.1 \times 10^{-8}$ N. The maximum fiber deformation is computed with the Euler-Bernoulli theory for beams as:

$$w_M = \frac{qL_f^4}{8EI} = 7.2 \times 10^{-3} \text{ mm}, \tag{3.1}$$

where $I = \pi d_f^4/64$ and $q = F_D/L_f$ is the hydrodynamic force per unit of fiber length, which we assume to be uniformly distributed along the fiber. The maximum value of deformation obtained is sufficiently small ($w_M/L_f = 0.6\%$) to consider fibers as rigid bodies. However, longer and more flexible fibers can exhibit large deformations, potentially producing flow modifications due to an intermittent storage/exchange of energy with the fluid [4].

Data acquisition has been performed using three different recording settings for unladen and fiber-laden experiments. The reason behind this choice is the high temporal resolution that fiber-laden experiments require to accurately measure the rotation rate. We used double-frame mode with 3.5 ms time delay for laser pulses for the image acquisition of tomo-PIV in the unladen flow. In addition to double frame recording, to perform a 3D-PTV velocimetry in the unladen flow, we recorded single-frame images at 1 kHz acquisition rate. Flow was seeded with tracers, with a diameter of 20 μm, by providing particle per pixel (ppp) concentration of 0.035 and 0.02 for tomo-PIV and 3D-PTV recordings, respectively. Source density number of the recordings, N_s, which quantifies the total number of pixel occupied by the tracers [for further details, see 76], is equal to 0.44 for tomo-PIV and 0.25 for 3D-PTV, and fall within the limits recommended by Novara and Scarano [61]. In case of fiber-laden experiments, images have been recorded at 1.8 kHz in single-frame mode, to ensure that the displacement of fibers in the center of the channel cannot exceed 2 pixel. In this way, the measurements are well resolved in time and the accuracy of the tracking process is higher. Source density number N_s in this case is equal to 0.1. Focal length, aperture size and depth of focus were the same for both unladen and fiber-laden recordings and were 100 mm, f/22 and 31 mm respectively. As a result, the digital resolution of the images is 24.1 pixel/mm. The cameras sensor size was cropped down to 1280×1280 pixel. Illumination was obtained with the simultaneous emission of both laser cavities. Details of recording properties are given in table 3.1.

3.1.1 Unladen flow velocimetry

The velocimetry of the unladen flow is carried out using both tomographic particle image velocimetry (tomo-PIV) [29], and Shake-the-Box (STB) algorithms [77]. The

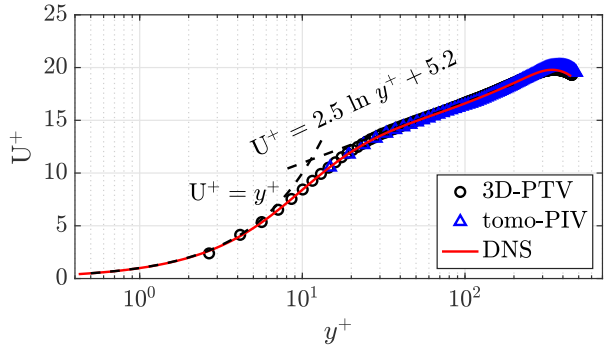

FIGURE 3.1 – Mean velocity profile obtained from 3D-PTV (Shake-the-box, circles) and tomo-PIV (triangles) compared with DNS at $Re_\tau = 350$ (solid line) [32].

Illumination volume (x, y, z)	$53.4 \times 53.4 \times 14$ mm^3
CCD sensor size (cropped)	1280×1280 pixel
Digital resolution	0.04166 mm/pixel
$f/\#$	22
Magnification	0.24
Depth of field	31 mm
Frame rate of fiber-laden recording	1.8 kHz
Frame rate of unladen recording, STB	1 kHz
Frame rate of double frame unladen recording, tomo-PIV	0.04 kHz
Standard deviation of calibration fit	< 0.03 pixel

TABLE 3.1 – Summary of the camera and laser recording parameters adopted.

cross-correlation process was applied to interrogation volumes of $48 \times 48 \times 48$ voxels. Prior to using the STB method, optical transfer function (OTF) was applied to correct the shape of particles by fitting an elliptical gaussian model to each sub-volume of the VSC. In total, 3×10^4 tracks in each snapshot were detected by the STB process. To evaluate the properties of the fluid flow considered, we compared single phase measurements with direct numerical simulations (DNS) of channel flow at $Re_\tau = 350$. Simulations are based on an in-house pseudo-spectral solver (Fourier-Chebyshev discretisation) [97]. The size of the channel is $4\pi h \times 2h \times 2\pi h$ and the domain is discretised with $512 \times 513 \times 512$ collocations points, in directions x, y and z respectively, with the lower wall located at $y = 0$. Statistics are computed over a time window of $1500\tau^+$. The mean velocity profile (streamwise) obtained from 3D-PTV (Shake-the-box, circles) and tomo-PIV (triangles) is compared with DNS results at $Re_\tau = 350$ (solid line) in figure 3.1.

We present the results of our dataset which consists of about 10^5 fibers, each tracked over at least 50 consecutive frames. This corresponds to a minimum time window of 28 ms ($\approx 2.8\tau$). We report, the wall-normal distribution of concentration, orientation and rotation rates of non-axisymmetric fibers and we also investigate how these parameters

are influenced by the fiber curvature.

3.1.2 Concentration

In figure 3.2, we present fiber concentration and average streamwise velocity as a function of wall distance. Fibers concentration for each curvature class, defined as the number of fibers (N) at a given y^+ normalised by the total number of fibers of that class (N_0), is shown in figure 3.2(a) as a function of the wall-normal coordinate. We classify here the fibers in three different classes according to their curvature, and the classification is highlighted on top of figure 3.2. The trend observed for the fibers of the first curvature class (defined here as straight fibers) is in agreement with previous experimental [18, 48] and numerical [95] investigations: N reduces from channel center towards the close-wall region. While concentration of fibers belonging to the first curvature class reduces from the center towards the near-wall region, this trend changes when the curvature of the fibers is increased. It has been shown numerically [88, 83] that, unlike straight rods, curved shaped fibers in shear flow experience a drift motion, i.e. a motion at constant velocity in a direction that differs from the flow direction. Therefore, we speculate that non-axisymmetric fibers in the buffer layer could experience more drift and out-of-plane (spanwise) displacements compared to straight fibers. This increases their permanence in the near-wall region and can possibly justify the accumulations observed for non-axisymmetric fibers. More detailed discussion regarding the possible reasons behind this near wall trend for concentration is provided in §4.2.1. We report in figure 3.2(b) the mean velocity profile of the fibers, in correspondence of three values of curvature, against the unladen flow velocity profile. We observe that the velocity of the fibers matches the fluid velocity when $y^+ \geq 50$, and it is also independent of curvature. Similarly to what has been reported for interface-resolved numerical simulations [95, and references therein], we observed that for all curvature values considered, fibers in the near-wall region ($y^+ < 50$) move faster than the fluid, possibly due to fibers sampling preferentially high-speed streaks. According to Do-Quang et al. [26], when long finite-size fibers move towards the wall transported by turbulent sweeps, collisions with the wall prevent fibers from passively following the fluid towards low-speed regions. As a result, the residence time of the fibers in high-speed flow regions is longer than that in the low-speed regions, and therefore the average streamwise velocity of the fibers can be larger than that of the fluid. This conclusion is supported by the results of Abbasi Hoseini et al. [2], who studied experimentally the behaviour of straight fibers in the near-wall region. They observed that fibers accumulate in high-speed streaks, and this tendency increases with the aspect ratio of the fiber. In our case, we can assume that the effective aspect ratio of the fiber is maximum when the fiber is straight, and it reduces when the fiber has a curvature. Therefore, it is reasonable to expect that the straighter the fibers, the higher their tendency to stay in high-speed streaks, the higher the mean velocity. This is in agreement with the near-wall results of figure 3.2(b), where an increase of curvature produces a reduction of velocity.

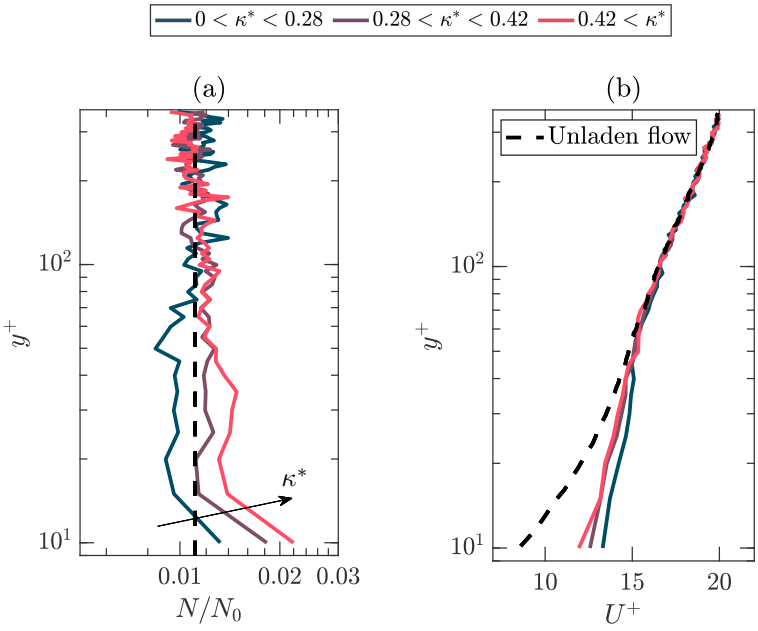

FIGURE 3.2 – (a) $x - z$ averaged normalised concentration of the fibers for three different classes. Vertical dash-line represents mean value of the concentration. (b) $x - z$ averaged streamwise velocity of fibers, U^+ (solid lines). The fluid velocity profile obtained for the unladen flow (dashed line) is also shown.

3.1.3 Orientation

To investigate the orientation of the fibers, we considered the angles that the fibers form with respect to streamwise, spanwise and wall normal directions (ϑ_x, ϑ_z and ϑ_y), as shown in figure 2.8(b). We classify the fibers in three curvature classes and we show in figure 3.3 the PDF of these angles in two different regions of the channel: center [$320 \leq y^+ \leq 400$, figures 3.3(a)-(c)] and near-wall [$0 \leq y^+ \leq 25$ figures 3.3(d)-(f)].
PDFs of ϑ_y [figures 3.3(a),(d)] show that the trend is independent of curvature in both regions considered. Near the wall, the peak of the PDF is close to $\pi/2$, i.e. the major axis of the fiber, x', belongs to a plane parallel to the channel wall. In the channel center no preferential alignment is expected, this is confirmed by figure 3.3(a), in which distribution appears random compared to the wall region. To summarize, in the near-wall region [figures 3.3(d)], the most probable orientation of the fibers with respect to wall normal direction, regardless of their curvature, is $\vartheta_y \approx \pi/2$, i.e. fiber preferably flow with x' parallel to the channel wall (xz plane). This observation is in agreement with both experimental [18] and numerical [26, 52, 19] findings obtained for ellipsoids in channel flow.
In the near-wall region ($0 \leq y^+ \leq 25$), we observe a preferential out of flow-plane orientation [(ϑ_z), figure 3.3(f)], which is sensitive to the curvature class of the fibers. In this region, for all curvatures, PDF of ϑ_y exhibits a sharp peak for $\vartheta_y \approx \pi/2$, that is, x' lies on xz planes and it appears that, the PDF of ϑ_x [figure 3.3(e)] and ϑ_z [figure 3.3(f)] are correlated. Fibers with high curvature values preferably align with the streamwise direction [figure 3.3(e), $\vartheta_x \approx 0$], but for fibers with low curvatures, we observe a bimodal (double peak) distribution. In contrast, the PDF of ϑ_x for straight fibers has a dominant peak for $\vartheta_x \approx \pi/3$. In figure 3.4, we consider the contours of joint probability distribution computed with respect to the orientation angles ϑ_x and ϑ_z. Joint PDF data for the near wall region are shown in figure 3.4 (a-c) for $\kappa^* < 0.28$, $0.28 < \kappa^* < 0.42$ and $\kappa^* > 0.42$, respectively. Data referring to the center are shown in figure 3.4 (d-f). We can see that in the near wall region, figure 3.4 (a-c), no matter of the curvature class, joint PDF show a correlated orientation for ϑ_x and ϑ_z, unlike the center of the channel, figure 3.4 (d-f), where PDF data for all curvature classes are totally scattered and uncorrelated. In particular, we focus on panel (c), i.e. curved fibers in the near-wall region. Indeed the fibers that contribute to the peak at $\vartheta_x = \pi/12$ in figure 3.3(e) are those that contribute to the peak at $\vartheta_z = 5\pi/12$ in figure 3.3(f). This is confirmed by figures 3.4(c), in which the maximum probability occurs for $\vartheta_x = \pi/12, \vartheta_z = 5\pi/12$. In this sense, in terms of orientation we can say that very curved fibers behave more like disks and out-of-plane orientations are less probable.
Although the reason behind the shape of the PDF is not fully clear, we observed (not reported here) that the two peak distribution persists for almost all curvature classes considered in the region $25 \leq y^+ \leq 100$. This behaviour is not solely function of curvature, but it is also sensitive to the local flow conditions (velocity gradients). We speculate that the different preferential orientation of the fibers in sweep and ejection structures is the main cause of above-mentioned bimodal distribution, and the curvature defines the magnitude of the dominant peak. This speculation is discussed in more detail in §4.2.3. Due to possible similarities with HIT conditions, fibers in the center of the channel have no preferential alignment with respect to the wall-normal

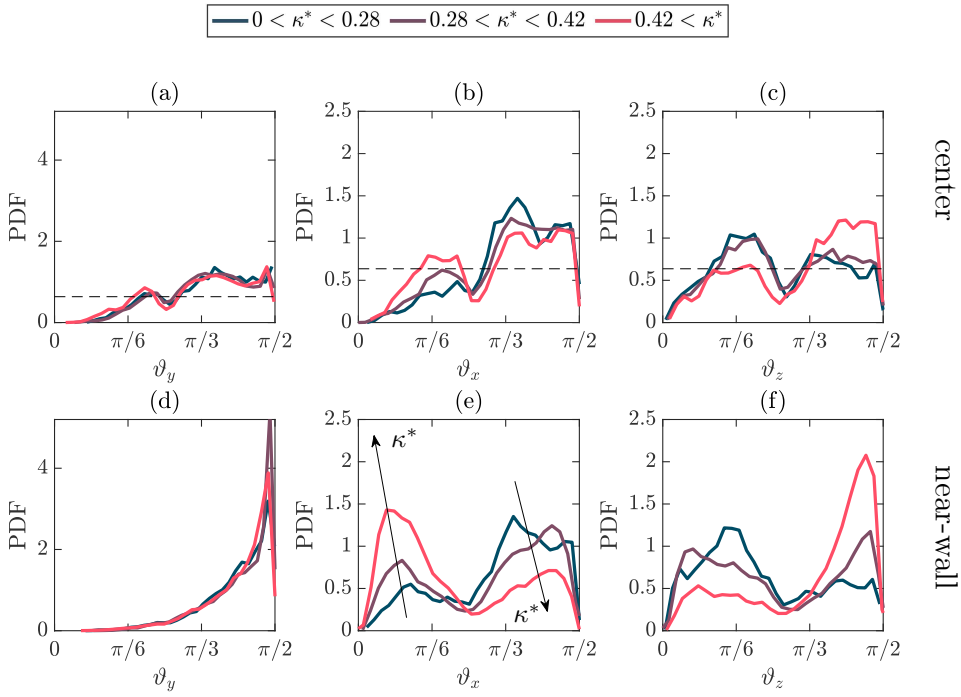

FIGURE 3.3 – PDF of the orientation angles of the fibers $(\vartheta_x, \vartheta_y, \vartheta_z)$ in the channel center $[320 \leq y^+ \leq 400$, panels (a)-(c)] and near-wall $[0 \leq y^+ \leq 25$, panels (d)-(f)]. Due to symmetry, angles shown are reduced to the first quadrant. Dashed lines in (a)-(c) represent uniform with no preferential distribution.

direction [ϑ_y, figure 3.3(a)]. In figures 3.3(b)-(c), the same behaviour is observed for the orientation with respect to the other directions, ϑ_x and ϑ_z respectively. In this case, with respect to the near-wall region, fibers exhibit a remarkably lower tendency to orient in a preferential direction.

3.1.4 Rotational dynamics

After the seminal work of Jeffery [37], in the instance of straight ellipsoids in shear flow, Hinch and Leal [35] investigated the dynamics of curved fibers in the same configuration. With the aid of asymptotic techniques, they showed that the rotational dynamics of slightly curved fibers can be significantly different from that observed in straight ellipsoids. In this section, we present experimental observations of the effect of curvature on the rotational dynamics of non-axisymmetric fibers discussing first the rotation rate about the axis of the laboratory reference frame and later examining the rotation rate about the fibers frame system, i.e. tumbling and spinning. Stream- and spanwise averaged rotation rates of the fibers, classified in three different ranges of curvature, are presented in figure 3.5, where panels 3.5(a),(b) and (c) refer to the rate of change of ϑ_x, ϑ_z and ϑ_y respectively. In particular, the $x-z$ averaged angular velocities, $|\dot{\vartheta}_x|, |\dot{\vartheta}_y|$ and $|\dot{\vartheta}_z|$, are defined as the mean value computed over horizontal planes of $|\partial\vartheta_x/\partial t|, |\partial\vartheta_y/\partial t|$ and $|\partial\vartheta_z/\partial t|$, respectively. Our data show that non-axisymmetric fibers rotate faster compared to straight rods, for all components considered and all along the channel height. We observe that, for the curvature classes considered, a nearly constant difference in the magnitude of the three rotation rates. We therefore observe that in the central region of the channel ($320 \leq y^+ \leq 400$), the rotation rate is uniform (i.e. independent of the y^+) for all classes. In this region, since fibers are long, they interact with the large structures of the flow. In the near-wall region, due to the greater shear, the magnitude of the rotation rate increases approaching the wall. It is also visible from figure 3.5(c) that the magnitude of the rotation rate $|\dot{\vartheta}_y|$ is lower than the other two components, $|\dot{\vartheta}_x|$ and $|\dot{\vartheta}_z|$.
Finally, we remark that there exists a nearly constant difference in the magnitude of the three rotation rates for different curvatures. To explain this observation, we associate the fibers with an effective length corresponding to the distance between two ends of the fibers. Since all fibers have statistically the same length, non-axisymmetric fibers have smaller effective length compared with straight rods. In this context, it is reasonable to assume that the longer effective length, the slower the rotation rate of the fibers.
In order to investigate the rotational dynamics of the fibers with respect to their local reference frame, we analyse the statistics of square tumbling rate, $\Omega_t\Omega_t$ (defined in §2.2.5), as a function of their curvature. As an example, a trajectory is shown in figure 3.6, in which fiber is coloured according with the instantaneous square tumbling rate ($\Omega_t\Omega_t$) normalised by the mean value computed over the entire track, $\langle\Omega_t\Omega_t\rangle$. The fiber tracked is located in the near-wall region, and the wall is here indicated as a grey surface. First, we observe that the acquisition rate used is sufficient to resolve the dynamics of the fiber in the present flow configuration [one every three instants measured is shown in figure 3.6(a),(b)]. The dynamics of the fiber is complex and characterised by subsequent rotations, which can be appreciated in the front view, in

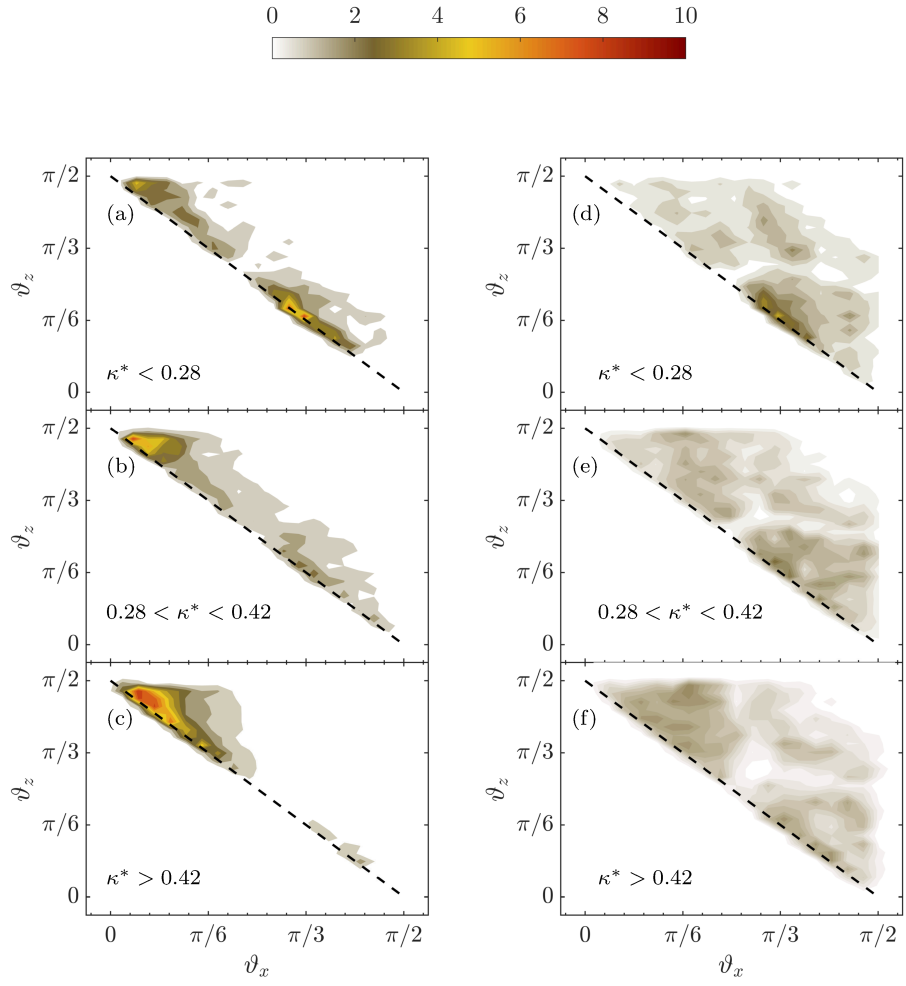

FIGURE 3.4 – Contours of joint probability distribution computed with respect to the orientation angles ϑ_x and ϑ_z. Two regions of the flow are considered: near-wall ($0 < y^+ < 25$, left column) and center ($320 < y^+ < 400$, right column). Fibers of different curvature are considered: $\kappa^* < 0.28$ (a,d), $0.28 < \kappa^* < 0.42$ (b,e) and $0.42 < \kappa^*$ (c,f).

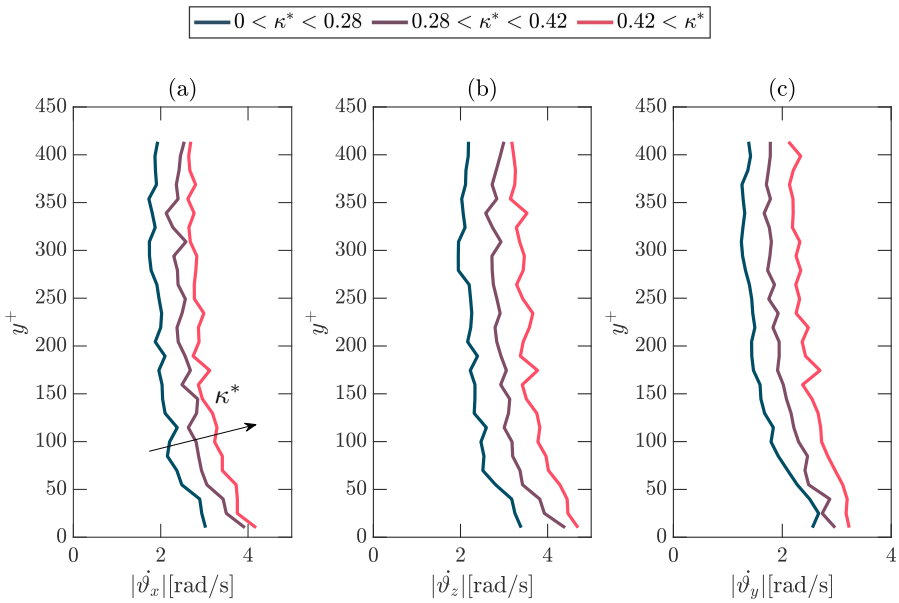

FIGURE 3.5 – $x-z$ averaged angular velocities of all three classes of fibers. The angular velocities in directions x, y and z ($|\dot{\vartheta}_x|, |\dot{\vartheta}_y|, |\dot{\vartheta}_z|$) are defined as the mean value computed over horizontal planes of $|\partial\vartheta_x/\partial t|, |\partial\vartheta_y/\partial t|$ and $|\partial\vartheta_z/\partial t|$, respectively.

figure 3.6(a). We also observe that the radius of the trajectory of the fiber is of the order of $20-30$ wall units, likely corresponding to the characteristic size of the coherent structures populating the turbulent near-wall region. It is also possible to observe from figure 3.6(b) the variation in the streamwise velocity of the fiber: closer to the wall, the velocity of the fiber is lower and the displacement between two consecutive instants is small. Away from the wall, the fiber moves faster and the distance between two consecutive positions increases. We also observe that the fiber can experience rapid changes of the tumbling rate, represented by strong color gradients in figure 3.6(a),(b). To provide a more global and quantitative estimation of the tumbling rates, we consider $\Omega_t\Omega_t$ computed over the whole dataset and non-dimensionalised with respect to the local Kolmogorov time scale, $\langle\Omega_t^*\Omega_t^*\rangle = \langle\Omega_t\Omega_t\rangle\tau_k^2$. Results are reported in figure 3.7(a) for three different regions of the channel, and as a function of the curvature of the fibers. Deviations from straight rod shape towards fibers with curvature produce significant changes in the magnitude of the tumbling rate, as shown in figure 3.7(a), where the dimensionless mean square tumbling rate increases with the curvature, κ^*. Moreover, we observe that the tumbling rate increases with the wall-normal coordinate, y^+. The studies investigating particles tumbling behaviour currently available in literature are related to straight rods [66, 54, 74, 11, 49, 10, 38]. For long and neutrally buoyant straight rods in HIT conditions, the magnitude of mean square tumbling rate is observed to be approximately 0.1 [66, 64]. Profile of the $\langle\Omega_t^*\Omega_t^*\rangle$ [figure 3.7(a)] at the center of the channel suggests that for vanishing curvature ($\kappa^* \to 0$), $\langle\Omega_t^*\Omega_t^*\rangle$ would be in the same order of magnitude of the mean square tumbling rate of straight rods obtained in HIT configuration. Same observation holds for the mean square tumbling

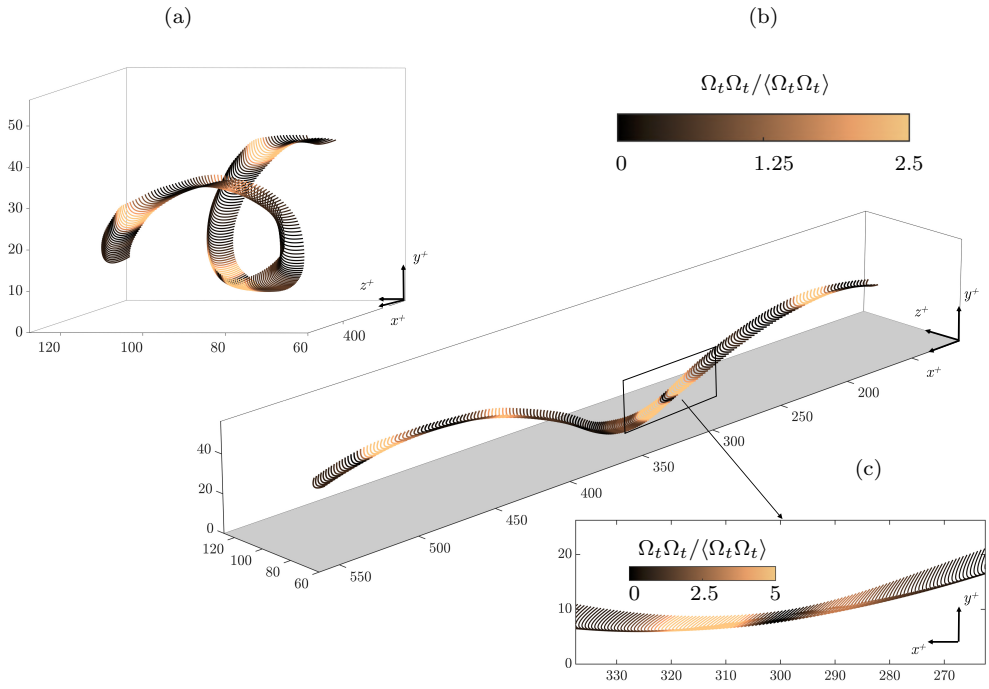

FIGURE 3.6 – Measurement of non-axisymmetric fiber travelling close to the wall, represented here by the grey surface. Front view (a) and side views (b,c) are shown. Fiber is coloured according to the instantaneous tumbling rate $\Omega_t\Omega_t$, normalised by the mean value computed over the entire track, $|\Omega_t\Omega_t|$. The acquisition rate is sufficiently high to resolve the dynamics of the fiber also in this case, in which the behaviour is complex. One in three instants measured is shown in (b), whereas all instants recorded are shown in (c). We can appreciate from panel (c) that the measurements are sufficiently resolved in time to smoothly record the transition from low (black) to high (yellow) tumbling dynamics. Time evolution of the motion of this track is available as Movie 1 in electronic supplementary materials.

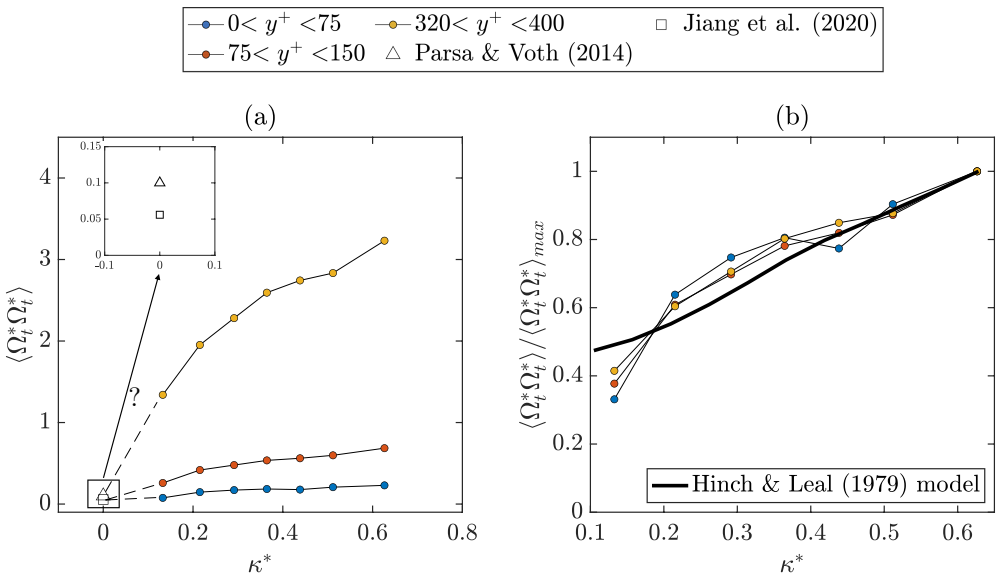

FIGURE 3.7 – Influence of curvature on the tumbling rate. Panel (a) $x-z$ averaged tumbling values, $\langle \Omega_t^* \Omega_t^* \rangle$, at different wall-normal locations. Panel (b) $x-z$ averaged tumbling values normalised by the maximum tumbling value of the specified region, compared with results obtained with the Hinch and Leal [35] model (solid line).

rate measured in the near-wall region of Rayleigh-Bénard experiments [38]. We would like to mention a possible error of bias here: Since the time scale of the flow varies from the wall to the center of the channel, the temporal filter used to process the data could slightly underestimate – wall region – or slightly overestimate – central region – the magnitudes of $\langle \Omega_t^* \Omega_t^* \rangle$. However, in all cases, the reported trend will not change. Effect of kernel size of the filtering on the statistics is thoroughly analysed in §5.2. Effect of kernel size of the filtering on the statistics is thoroughly analysed in §5.2.

We compare now the mean square tumbling rate of non-axisymmetric fibers (present experiments) with that of non-axisymmetric ellipsoids in viscous flow (theoretical model). We solve numerically the autonomous system of ordinary differential equations for the Euler angles of curved ellipsoids in laminar shear flow [35]. We consider the same range of curvature (κ^*) studied in our experiments, and $\kappa^* \to 0$ gives the so called "Jeffery orbits" [37]. We will refer at the results obtained from this procedure as Hinch and Leal [35] model.

Hinch and Leal [35] introduced an autonomous system of ordinary differential equa-

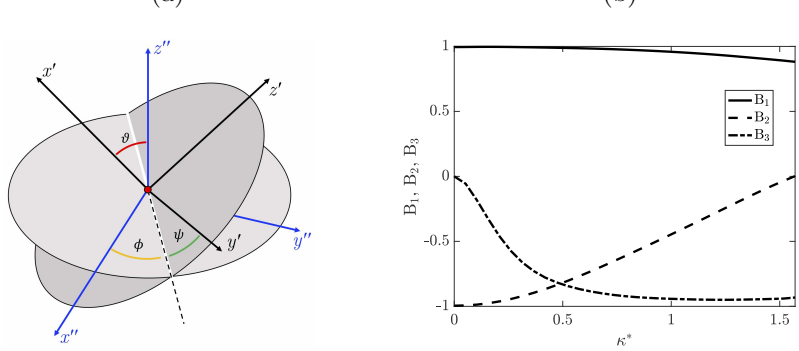

FIGURE 3.8 – (a) Definition of Euler angles (ϑ, ψ, ϕ) adopted. (b) Coefficients B_1, B_2 and B_3 as function of curvature, κ^*.

tions to describe the evolution of the Euler angles of any ellipsoid as:

$$\dot{\vartheta} = \frac{1}{2}\alpha \sin 2\vartheta \sin 2\phi + \frac{1}{2}\beta(-\sin 2\vartheta \sin 2\phi \cos 2\psi - 2\sin\vartheta \cos 2\vartheta \sin 2\psi), \quad (3.2)$$

$$\dot{\phi} = -\frac{1}{2} + \alpha \cos 2\phi + \beta(-\cos\vartheta \sin 2\phi \sin 2\psi + \cos 2\phi \sin 2\psi), \quad (3.3)$$

$$\dot{\psi} = -\alpha \cos\vartheta \cos 2\phi + \beta(\cos^2\vartheta \sin 2\phi \sin 2\psi - \cos\vartheta \cos 2\phi \cos 2\psi) + \gamma(\cos^2\vartheta \sin 2\phi \sin 2\psi - 2\cos\vartheta \cos 2\phi \cos 2\psi + \sin 2\phi \sin 2\psi), \quad (3.4)$$

where Euler angles (ϑ, ψ, ϕ) are defined as in figure 3.8 and $\alpha = 0.25(B_2 - B_1)$, $\beta = 0.25(B_2 + B_1)$ and $\gamma = 0.25B_3$, with B_i coefficients to be defined. Thorp and Lister [83] observed that Eqs. (3.2)-(3.4) are valid for any object with two planes of symmetry, provided that B_1, B_2 and B_3 can be measured independently. In case of axisymmetric ellipsoids, $B_1 = B_2$ and $B_3 = 0$. When the particle shape starts to deviate from the symmetric condition, values of B_1, B_2 and B_3 will be independent of each other and should be found from the grand resistance matrix [75]. Representation of B_1, B_2 and B_3 values as function of curvature for a curved prolate ellipsoid with aspect ratio of 20 is shown in figure 3.8(b). We used these values to solve Eq. (3.2) for ϑ, ϕ and ψ. An example of Euler angles for two different values of curvature is reported in figure 3.9(a). Euler angles are correlated to the rotation rate around the particles axis as follows:

$$\omega_z = \dot{\vartheta}\cos(\psi) + \sin(\vartheta)\sin(\psi)\dot{\phi}\ , \quad (3.5)$$

$$\omega_y = -\dot{\vartheta}\sin(\psi) + \sin(\vartheta)\cos(\psi)\dot{\phi}\ , \quad (3.6)$$

$$\omega_x = \dot{\psi} + \cos(\vartheta)\dot{\phi}\ , \quad (3.7)$$

with ω_i defined as in figure 2.8. We find the values of ω_z and ω_y for different initial conditions for the Euler angles $(\vartheta_0, n\pi, \psi_0)$, with $\vartheta_0, \psi_0 \in [0; \pi]$ and n integer. mean square tumbling rate are shown in figure 3.9(b), where $\Omega_t\Omega_t = \omega_z^2 + \omega_y^2$. We observed that while the location of the crossing point of the tumbling components, $\langle\omega_z^2\rangle$ and

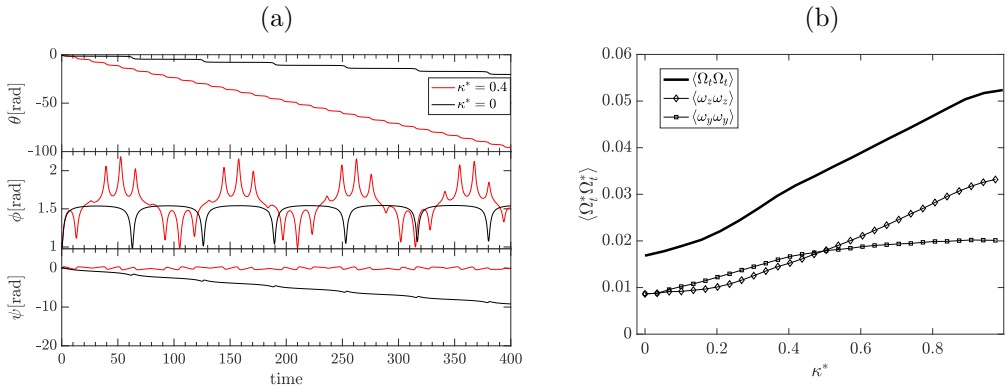

FIGURE 3.9 – (a) Evolution of Euler angles ϑ, ϕ and ψ for $\kappa^* = 0$ (straight fiber) and $\kappa^* = 0.4$ (curved fiber). (b) Components of the tumbling rate obtained from the model of Hinch and Leal [35]. Squares and diamonds represent $\langle \omega_y^2 \rangle$ and $\langle \omega_z^2 \rangle$ respectively, whereas solid line $\langle \Omega_t \Omega_t \rangle$ is the sum of the two contributions.

$\langle \omega_y^2 \rangle$, is sensitive to the time window considered, the averaged tumbling rate $\langle \Omega_t \Omega_t \rangle$ is independent of the time interval size.

In figure 3.7(b), $\langle \Omega_t^* \Omega_t^* \rangle$ is normalised by the maximum value of the mean tumbling rate of each region, $\langle \Omega_t^* \Omega_t^* \rangle_{max}$ (corresponding also to the maximum κ^* considered), and then shown with the data obtained from the analytical results as function of curvature. Even though the flow configuration is different, and more importantly shear decreases approaching the channel center, the dependency of the normalised tumbling rate with respect to the curvature value is in fair agreement with the behaviour predicted by the Hinch and Leal [35] model. This indicates that, although fibers interact with flow structures of different size across the entire channel height, for the specific parameter range explored in this paper, the curvature-induced asymmetry, in other words fibers shape, is chiefly responsible for the observed trend.

In the instance of (axisymmetric) ellipsoids, the mean values of the two components of the tumbling (ω_y^* and ω_z^*) averaged over a long time window will match. Indeed, straight ellipsoids can have infinite planes of symmetry containing the symmetry axis, and the dynamics is invariant with respect to the local reference frame chosen, provided that the symmetry axis coincides with one of the axis of the local reference frame. However, this is not the case when the particle shape becomes non-axisymmetric. To investigate this behaviour, in figure 3.10 we plot separately the components of mean square tumbling rate averaged over the region considered, $\langle \omega_y^* \omega_y^* \rangle$ and $\langle \omega_z^* \omega_z^* \rangle$, along with the numerical results obtained from the model by Hinch and Leal [35]. Note that " * " represents the non-dimensionalisation with respect to the local Kolmogorov time scale. We observe from the model results that there should be a crossing point for the two tumbling components. We confirm the existence of this crossing point for all datasets presented and at all locations in the channel (figure 3.10).

Finally, we consider the PDFs of square tumbling rate normalised by mean square tumbling rate of each curvature class, $\Omega_t^* \Omega_t^* / \langle \Omega_t^* \Omega_t^* \rangle$. Results are shown for the center

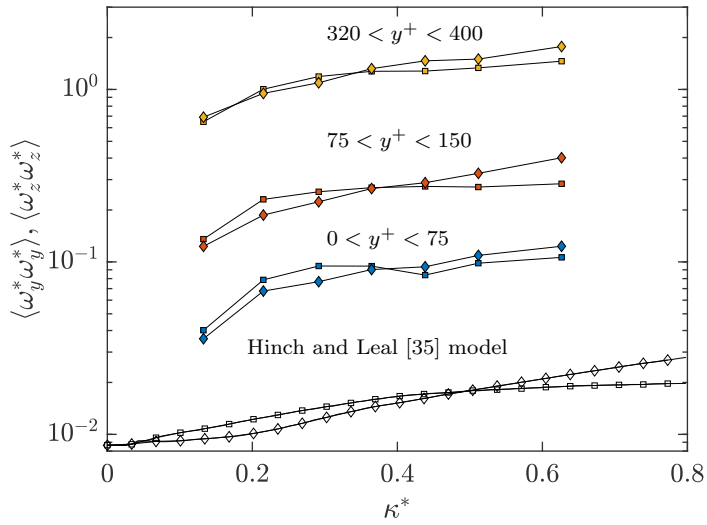

FIGURE 3.10 – $x-z$ averaged tumbling components, as a function of curvature, for three regions of the channel. Results for curved ellipsoids, obtained from the model by Hinch and Leal [35] are also reported. Squares and diamonds represent ω_y^* and ω_z^* respectively.

($320 \leq y^+ \leq 400$) and for the near-wall regions ($0 \leq y^+ \leq 25$) of the channel, in figures 4.4(a) and 3.11(b) respectively. In the center, the PDFs show a trend for low values of $\Omega_t^* \Omega_t^* / \langle \Omega_t^* \Omega_t^* \rangle$: curved fibers experience more frequently low-speed rotation motions than the straight ones . These results do not contradict the $x-z$ averaged square tumbling rate data shown in figure 3.7, since statistics reported in figure 3.11 are normalised by the mean value of each class, which increases with curvature. In addition, our results for "straight fibers" are in fair agreement with the previously reported experimental data obtained for straight rods in HIT configuration [66, 38], as shown in figure 3.11(a). However, we remark here that fibers belonging to the first curvature class cannot be strictly considered as straight. In the near-wall region, figure 3.11(b), for all curvature classes the probability of having extreme events is higher compared to the channel center, figure 3.11(a), due to the presence of near-wall coherent structures and fiber-wall interactions. In addition, we observe from figure 3.11(b) that the probability of having extreme events decreases with curvature. We remark here that, in general, non-axisymmetric fibers are characterised by higher tumbling rates compared to straight rods (shown in figure 3.7), but in figure 3.11 the tumbling rate reported is normalised with respect to the mean value of each class.

3.2 Conclusions

In this chapter, we investigated experimentally the behaviour of long non-axisymmetric fibers in turbulent channel flow. We provided, original experimental measurements of concentration, orientation and rotation rates of long curved fibers. The effect of the non-axisymmetric shape of the fibers produces important differences in the fiber

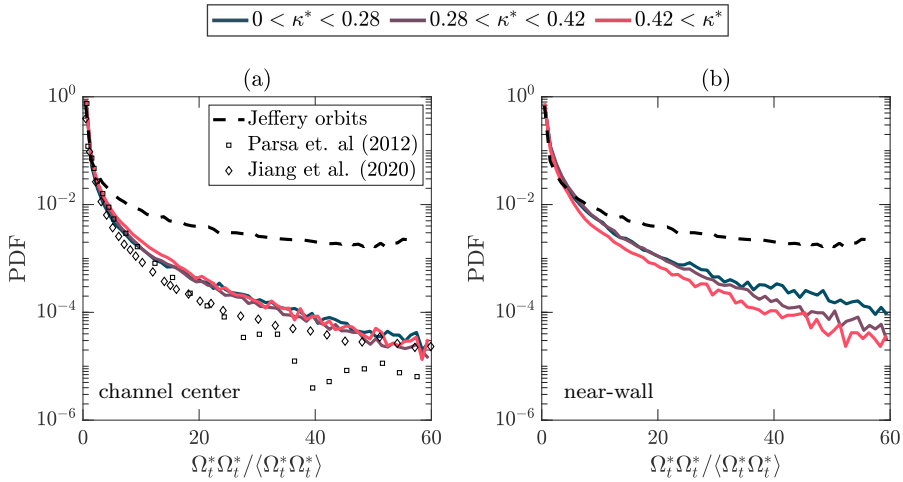

FIGURE 3.11 – PDF distribution of tumbling rates in the channel center ($320 \leq y^+ \leq 400$), panel (a), and in the near-wall region $0 \leq y^+ \leq 25$, panel (b), is reported for fibers with different curvatures. Experimental measurements for straight fibers in HIT configuration [66, 38] are also shown (symbols) as well as results for straight ellipsoids [Jeffery orbits, obtained with the Hinch and Leal [35] model with $\kappa^* = 0$, dashed line].

behaviour with respect to straight rods, both in terms of orientation and rotation rates. We confirmed previous results on fibers concentration and velocity, obtained from direct numerical simulations of straight fibers in turbulent channel flow. We observed a curvature effect on the concentration of the fibers and we also speculate that fibers preferably stay in high-speed streaks, in agreement with previous observations. We also characterised the fibers behaviour in different regions of the channel, namely channel center and near-wall regions, and we observed that the orientation of the fiber with respect to stream- and spanwise directions is strongly influenced by curvature. Similarly, the rotation rates (i.e. the rate of change of the orientation angles) strongly depend on the curvature of the fibers: high curvature values produce large rotation rates across the entire channel height. We measured the tumbling rate of long, non-axisymmetric fibers and we compared the results with the numerical solutions obtained for curved ellipsoids in shear flow [35]. We found that the normalised square tumbling rate of the fibers is in excellent agreement with the theoretical predictions, and also in this case the curvature plays a key role, modulating the intensity of the tumbling rate measured. Finally, we observed that the fiber dynamics in the center of the channel shares some similarities with previous results in HIT configuration, which makes the current facility suitable to obtain information for both bounded and unbounded flows.

4

Effect of Reynolds number

In this chapter, we investigate the effect of Reynolds number on the concentration, orientation and rotation rate of the fibers. Statistics are provided for three Reynolds numbers, Re_τ=180, Re_τ=360 and Re_τ=720 and similar to §3, statistics are classified based on fibers curvature. In this chapter, particular focus is on the reasons behind the observed trends for fibers concentration and orientation.

4.1 Experimental setup

We performed three-dimensional tracking of fibers in turbulent channel flow. The fibres are polyamide-based, long and non-axisymmetric. A microscope view in dry conditions is reported in figure 2.2. We use the experimental facility, the fibre modelling and tracking methodology presented in §2 and §3. The existing database (limited to $Re_\tau = 360$) has been extended by adding further measurements at lower ($Re_\tau = 180$) and higher ($Re_\tau = 720$) Reynolds numbers. The shear Reynolds number, $Re_\tau = u_\tau h/\nu$, is based on shear velocity (u_τ), half channel height ($h = 80$ mm) and kinematic viscosity of the fluid (ν). The fluid used for the experiments is water at the average temperature of 15°C, corresponding to dynamic viscosity $\mu = 1.138{\times}10^{-3}$ Pa·s [44].
Details of flow and imaging parameters for all experiments considered are reported in table 4.1. Image acquisition and single phase velocimetry have been carried out using Davis 10(LaVision GmbH). The Stokes number of the fibres calculated as the ratio of fiber response time to the viscous time of the flow (τ) varies between $St = 0.001$ ($Re_\tau = 180$) and $St = 0.011$ ($Re_\tau = 720$). When computed with respect to the Kolmogorov time scale, the Stokes number of the fibers is even lower, and varies between $St = 3.9 \times 10^{-4}$ ($Re_\tau = 180$) and $St = 4.3 \times 10^{-4}$ ($Re_\tau = 720$), therefore, we conclude that the inertia of the fibres has negligible effects.

4.1.1 Single-phase velocimetry

The single-phase velocimetry has been obtained with the Shake-the-Box (STB) algorithm [77], a three-dimensional and time-resolved particle tracking method (4D-PTV). The flow is seeded with tracer particles (diameter 20 μm), which are also used for the Volume-Self-Calibration (VSC) algorithm [89] required for the fibres reconstruction and tracking. To increase the signal-to-noise ratio of the recorded images, a series

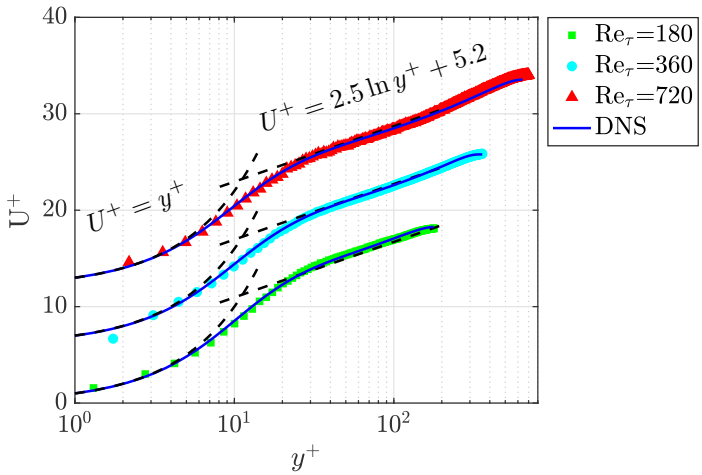

FIGURE 4.1 – Streamwise velocity profiles for the experimental configurations considered. Fluid velocity (U^+) and wall-normal coordinates (y^+) are reported in wall units. Symbols refer to experimental measurements labelled as $Re_\tau = 180$ (□), $Re_\tau = 360$ (◯) and $Re_\tau = 720$ (△) (see table 4.1 for a summary of the parameters of the experiments). Profiles are increased by a coefficient 6 for better visualisation. Solid lines refer to velocity profiles obtained from direct numerical simulations at $Re_\tau = 180$ [57], $Re_\tau = 350$ [32] and $Re_\tau = 650$ [36]. Dashed lines indicate the theoretical profiles in the inner ($U^+ = y^+$) and outer ($U^+ = 2.5 \ln y^+ + 5.2$) layers.

Flow parameters			Imaging parameters			Flow and fibre scales		
Re_τ [-]	$Re_{\tau,\text{eff}}$ [-]	Phase	resolution [px]	f [Hz]	volume [mm^3]	τ [s]	δ [10^{-3} m]	L_f/δ [-]
180	195	Water	1280×1280	600	$53.4 \times 53.4 \times 14$	0.0366	0.204	5.9
		Fibers	1280×1280	1000	$53.4 \times 53.4 \times 14$			
360	363	Water	1280×1280	1000	$53.4 \times 53.4 \times 14$	0.0104	0.11	10.9
		Fibers	1280×1280	1800	$53.4 \times 53.4 \times 14$			
720	703	Water	1024×1104	1800	$44.9 \times 48.4 \times 13$	0.0028	0.057	21.6
		Fibers	1024×1104	2600	$44.9 \times 48.4 \times 13$			

TABLE 4.1 – Summary of the flow and imaging parameters adopted. The reference and effective Reynolds numbers, respectively Re_τ and $Re_{\tau,\text{eff}}$, are reported. Imaging parameters for the single-phase (water) and partcile-laden (fibers) as well as flow and fibres scales in wall-units are indicated. τ and δ refer to viscous time and length scales, respectively.

of preparatory steps has been applied (e.g. time and spatial filtering, background noise removal). Further details on the image preprocessing applied are described in §2.1.3. Afterwards, VSC is performed, assuming $8\times8\times5$ (x, y, z) sub-volumes (average disparity error of ≈ 0.02 pixel, well within the limits recommended by [89]).
The particles are tracked through the STB method is applied, after optical transfer function (OTF) are obtained and used to correct the particles shape. In each snapshot, on average, a number of particle tracks greater than 2×10^4 has been detected by the STB tracking algorithm for different Re_τ cases. In figure 4.1, we compare the quality of the flow produced in the TU Wien Turbulent Water Channel against the results obtained in Direct Numerical Simulations (DNS) [57, 3, 36]. The streamwise fluid velocity (U^+) is reported as a function of the distance from the wall (y^+), and both variables are expressed in inner units for the three Reynolds number considered. We observe that the mean velocity profiles obtained from 4D-PTV (Shake-the-box, symbols) are in excellent agreement with the DNS results (solid line) over the whole channel height. The size of the

4.2 Results

We present the results of our dataset which consists of about 5×10^4 fibers, each tracked over at least 100, 50 and 20 consecutive frames for $Re_\tau = 180, 360$ and 720, respectively. This corresponds to a minimum time window of $\approx 2.8\tau$. We report the wall-normal distribution of concentration, orientation and rotation rates of non-axisymmetric fibers and we also investigate how these parameters are influenced by the fiber curvature.

4.2.1 Concentration

We consider here the fibres distribution as a function of the wall-normal coordinate, y^+. For each curvature class, we introduce the normalised fibres concentration defined as fibres count (N) divided by the total number of fibres detected in that class (N_0). The data are averaged in $(x - z)$ by considering 90 bins in height of the channel. The statistics are reported for the entire channel height ($0 \leq y^+ \leq \mathrm{Re}_\tau$) and for three ranges of curvature (κ^*). The horizontally-averaged $(x - z)$ normalised fibres concentration, N/N_0, is reported is figure 4.2 for all Reynolds number considered. We will analyse first the effect of curvature and then the effect of Reynolds number on the fibres distribution.
As already observed in §3.1.2, while no remarkable difference occurs in the core of the flow (centre of the channel), the tendency of non-axisymmetric fibres to accumulate in the near-wall region is higher than for straight fibres. This trend, that is consistent for all Reynolds numbers considered, occurs over a region of variable thickness, from $y^+ \leq 50$ when $\mathrm{Re}_\tau = 180$, to $y^+ \leq 150$ for $\mathrm{Re}_\tau = 720$. The minimum y^+ location at which fibers are detected is also variable with Re_τ, since the physical fibres and domain size are kept constant, and the dimensionless fiber length (L_f^+) increases with Re_τ. Moreover, we wish to comment here on the higher near-wall accumulation reported in §3.1.2, figure 3.2(a), for $10 \leq y^+ \leq 20$ with respect to figure 4.2(b). In this chapter, the experimental database previously used ($\mathrm{Re}_\tau = 360$) has been extended

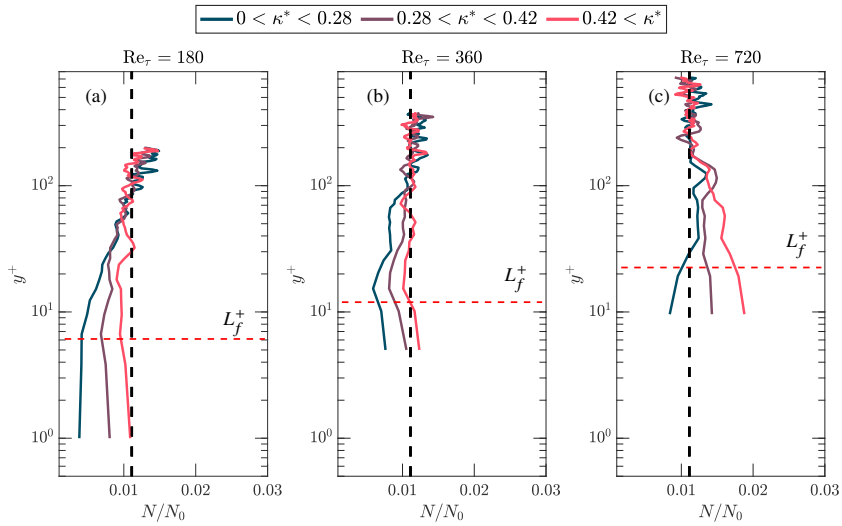

FIGURE 4.2 – (a) $x - z$ averaged normalised fibers concentration (N/N_0, solid lines) is shown as a function of the distance from the wall (y^+) for three different curvature classes (κ^*). The mean value of concentration (vertical, dashed lines) is indicated, as well as the location corresponding to the fiber length in inner units (L_f^+, horizontal, dashed lines). The Reynolds numbers, Re_τ, increases from (a) to (c).

and the measurements improved. As a result, when $\mathrm{Re}_\tau = 360$, fibres are tracked down to $y^+ = 5$ and the normalised concentration values for $10 \leq y^+ \leq 20$ slightly differ from previous measurements. We would like to point out a possible source of uncertainty of the method proposed. Due to the presence of laser reflections at the bottom wall, measurements very close to the wall surface ($0 - 200$ μm) have lower accuracy compared to the rest of the channel, possibly influencing the magnitude of the fibers concentration measured. However, concentration profiles obtained for fibers belonging to different curvature classes exhibit a trend that is consistent along the channel height, showing no change for the lowest value of y^+ reported. This observation suggests that the uncertainty on the fibers measurements induced by the laser reflections has no remarkable impact on the statistics considered. While the influence of fibres curvature is particularly important in the near-wall region, the effect of the Reynolds number is apparent over a wider portion of the domain considered. For $\mathrm{Re}_\tau = 180$ and 360, we report a reduction of the concentration from the channel centre towards the walls. This observation, in agreement with previous works on straight rods [48, 95], is valid for all curvature classes considered. The situation is different when $\mathrm{Re}_\tau = 720$: the concentration profiles show an opposite tendency with respect to lower Re, with a local increase of the number of curved fibres from centre towards the wall.

We speculate that the reason behind the reduction of concentration in the near wall region, observed for $\mathrm{Re}_\tau = 180$ and 360, is due to their possible interaction with the wall [see also Capone et al. [18]]. Abbasi Hoseini et al. [2] observed that fibers-wall interactions depend on fibers size and aspect ratio. Therefore, to further investigate

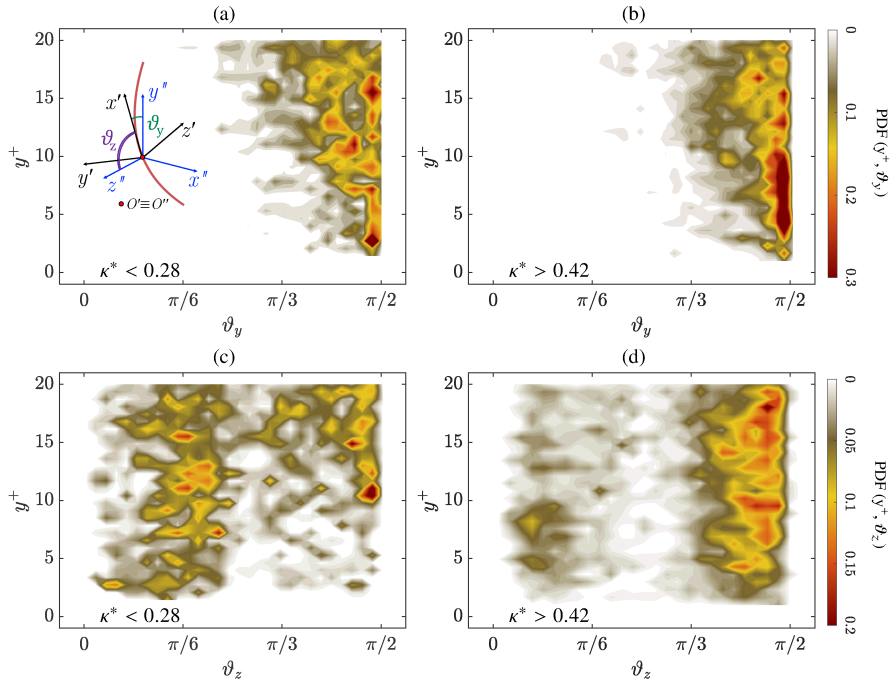

FIGURE 4.3 – Particle preferential location and orientation for $\mathrm{Re}_\tau = 180$ in the region $y^+ \leq 20$. Joint PDF of particle wall-normal position, y^+, orientation ϑ_y (a,b) and orientation ϑ_z (c,d) are reported. The angles are defined as in the inset of panel (a). Two classes of fibers are considered: nearly straight ($\kappa^* < 0.28$, panels a,c) and highly curved ($\kappa^* > 0.42$, panels b,d).

this aspect, we show in figure 4.3 the joint PDF of particle wall-normal position (y^+) and orientation (ϑ_y or ϑ_z) for $\mathrm{Re}_\tau = 180$ and $y^+ \leq 20$. The two angles considered, ϑ_y and ϑ_z, depicted in the inset of figure 4.3(a), represent the angles formed by the principal axis of the fiber (x') with the lab reference frame translated to the midpoint of the fiber (y'' and z'', respectively). The joint PDF of (y^+, ϑ_y) and (y^+, ϑ_z) are reported in figure 4.3(a,c) and figure 4.3(b,d), for straight ($\kappa^* < 0.28$) and curved ($\kappa^* > 0.42$) fibers respectively.

We observe that both straight and curved fibers align preferentially parallel to the wall, i.e. the angle ϑ_y is large ($\pi/3 \leq \vartheta_y \leq \pi/2$). However, from a closer view one can observe that while for curved fibers $\vartheta_y \approx \pi/2$ for $3 \leq y^+ \leq 10$, for straight fibers the peak of the probability distribution corresponds to $\vartheta_y \approx \pi/2$ and $y^+ \leq 3$. One possible reason of this difference is due to the geometry of the fibers. When $\vartheta_y = \pi/2$, the center of mass of straight fibers can stay up to $y^+ = d_f/\delta = 0.05$, with d_f fiber diameter. When fibers have large values of curvature, instead, the minimum distance of the center of mass depends on the orientation of the fibers plane with respect to the laboratory reference frame. Another possible reason of the different behaviour observed for straight and curved fibers in the region $0 \leq y^+ \leq 10$, could be explained with different fiber-wall (rebound) and fiber-coherent structure interactions.

We consider now the orientation (ϑ_z) that the fibers have with respect to the spanwise direction, and we analysed the joint PDF of (y^+, ϑ_z) shown figure 4.3(c) and (d), for straight and curved fibers, respectively. It is clear in this case that, within the region $y^+ \leq 10$, straight fibers align preferentially with $\vartheta_y = \pi/6$. Outside of this region, i.e. for $10 \leq y^+ \leq 20$, fibers align both with angles $\vartheta_y = \pi/6$ and $\vartheta_y = \pi/2$. The picture is different for fiber with $\kappa^* > 0.42$ [figure 4.3(d)]. The dominant orientation over the entire region considered is $\vartheta_y = \pi/2$. However, when $y^+ \leq 10$, a considerable number of fibers aligns with $\vartheta_y \approx \pi/6$. These differences suggest, again, that the curvature of the fibers plays a crucial role on their dynamics, making the fibers to respond differently to wall-interactions (rebound) and near-wall coherent structures.

The orientation of curved fibers, reported figures 4.3(b) and (d), indicates that their preferential alignment corresponds to $\vartheta_y \approx \vartheta_z \approx \pi/2$. As a results, one can observe that the principal axis of the fiber (x') remains aligned with the streamwise direction ($x \equiv x''$). We identify two possible fibers motions fulfilling this condition: i) fibers are mainly carried in streamwise direction (i.e. the alignment of the principal axis of the fiber is constant), and ii) fibers experience drift. A drift motion consists of a translation movement along a path inclined with respect to the streamwise direction. It has been shown numerically [88, 83] that non-asymmetric fibers could experience such a motion in shear flows. However, further measurements in wider domains (i.e. larger extension of the measurement region in spanwise direction) are required to study in detail this phenomenon.

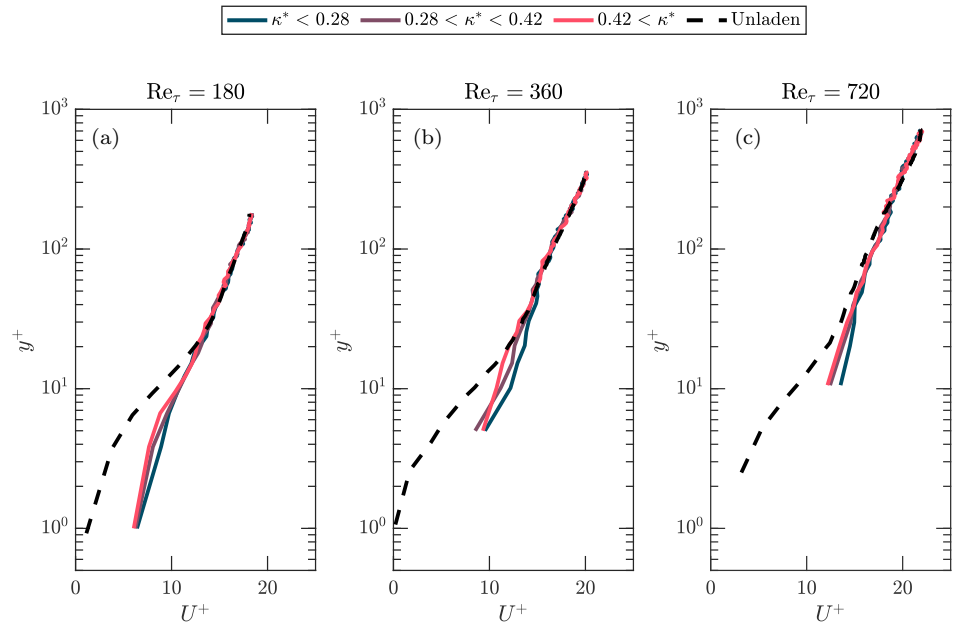

FIGURE 4.4 – $x - z$ averaged stream-wise velocity (U^+) obtained for fibers (solid lines) in correspondence of three values of shear Reynolds number, respectively $Re_\tau = 180$ (a), $Re_\tau = 360$ (b) and $Re_\tau = 720$ (c). Fibers are divided according to their curvature, κ^*, in three different classes. Fluid velocity profiles (unladen flow, dashed line) obtained from single-phase measurements are also shown.

4.2.2 Streamwise velocity

We report in figure 4.4 the mean velocity profile of the fibers (solid lines), in correspondence of three values of curvature and in three different Re_τ numbers. Profiles are compared against single-phase experiments (unladen flow, solid lines). Mean velocity profile of $\mathrm{Re}_\tau = 180$, $\mathrm{Re}_\tau = 360$ and $\mathrm{Re}_\tau = 720$ are shown in figure 4.4(a), (b) and (c), respectively. Due to experimental limitations, we resolve the near-wall region up to $y^+ = 1$, 5 and 10 for $\mathrm{Re}_\tau = 180$, 360 and 720, respectively. In all cases, fibers velocity profiles match the fluid velocity in the center, in agreement with experimental observations of Capone et al. [18]. Approaching the near-wall region, a deviation from the single-phase profile starts at $y^+ \geq 20$ for $\mathrm{Re}_\tau = 180$, at $y^+ \geq 40$ for $\mathrm{Re}_\tau = 360$ and at $y^+ \geq 60$ for $\mathrm{Re}_\tau = 720$. In particular, fibers are observed to move faster than the fluid, as also reported by Abbasi Hoseini et al. [2] and Capone et al. [18], possibly due to the fibers tendency to stay preferentially in the high-speed streaks [1]. Abbasi Hoseini et al. [2] have also shown that this behaviour depends on the length-to-diameter fiber ratio: The larger the aspect ratio, the higher the fibers near-wall streamwise velocity. Very recently, Shaik et al. [78] observed a similar near-wall behaviour for fibers having Stokes number about two orders of magnitude larger than that in this study.

We report in figure 4.5(a,b) the PDF of the streamwise velocity of the fibers (classified by their curvature) and of the unladen flow for $\mathrm{Re}_\tau = 180$ and $\mathrm{Re}_\tau = 720$, respectively.

The data (circles) are fitted by Gaussian functions (solid lines). In figure 4.5(a), we start considering the center of the channel ($170 \leq y^+ \leq 210$), in which the location of the peaks of the PDF(U^+) is the same for both fibers and unladen flow ($U^+ \approx 18.5$). One can observe that there is not any effect of curvature and only a slight difference in the magnitude of the peaks of the PDF of the fibers compared to the fluid is visible. Then, we consider the region $50 \leq y^+ \leq 70$, closer to the wall but beyond the buffer layer. In this case, the difference between the fibers and the single-phase profiles gets larger, and it is also a function of the curvature. Similarly to what has been observed in the center, the peak of the PDFs in constant (PDF(U^+) ≈ 16.5) while their shape differs. In particular, the larger discrepancies are found for low values of velocity ($10 \leq U^+ \leq 14$): Fibers move slower than the fluid, and the higher the curvature, the lower the fibers velocity. Finally, we consider the near-wall region ($1 \leq y^+ \leq 20$). The probability distributions are rather different in this case, suggesting that there is not only one dominant value of velocity, but the curves are rather characterised by two distinct peaks (bimodal distribution). We believe that in this region the fibers average velocity could be influenced by the near-wall coherent structures. Indeed, as suggested by Abbasi Hoseini et al. [2], who performed experiments at $\mathrm{Re}_\tau = 170$ and large fibers aspect ratio, the bimodal distribution of PDF(U^+) observed for the fibers is nothing but the footprint of sweeps and ejections. The position of the peaks associated to sweeps and ejections are also supported when we ensemble the fibers as descending and ascending fibers and re-plot the same PDF. We observe that the bimodal trend is present for all fibers curvatures classes considered, but the magnitude of the PDF is a function of the curvature. We consider the range of velocities $0 \leq U^+ \leq 5$, approximately corresponding to $0 \leq y^+ \leq 5$, i.e. to a near-wall region having thickness in the same order of the fibers length, L_f^+. In this interval, the probability of finding fibers with a given curvature is a function of κ^*: curved fibers ($\kappa^* \geq 0.42$) have much higher probability than the straighter ones ($\kappa^* \leq 0.28$). Therefore, curved fibers are expected to move slowly in this region and their residence time will increase with respect to the straight ones. This dynamics could possibly justify to the curvature-induced concentration increase observed in figure 4.2. In figure 4.5(b), we consider the region $640 \leq y^+ \leq 720$, $300 \leq y^+ \leq 360$ and $1 \leq y^+ \leq 60$ resembling similar regions as shown for $\mathrm{Re}_\tau = 180$ in figure 4.5(a). Same as $\mathrm{Re}_\tau = 180$, trends are very similar for channel center, $640 \leq y^+ \leq 720$ and closer to the wall but beyond the buffer layer, $300 \leq y^+ \leq 360$. In the near wall region, unlike $\mathrm{Re}_\tau = 180$, we are not bale to see a distinguishable bi-modal distribution, but the same trend as function fo curvature is visible. For range of velocities $0 \leq U^+ \leq 8$, the probability of finding fibers with a given curvature is a function of κ^*: curved fibers ($\kappa^* \geq 0.42$) have much higher probability than the straighter ones ($\kappa^* \leq 0.28$). We conclude that the tendency of the fibers to interact with the wall (rebound) and the near-wall coherent structures is a function of curvature, similarly to what has been observed in the §4.2.1, and the orientation will be also influenced by the fibers shape (See §4.2.3). However, as mentioned in §4.2.1, to fully comprehend the reasons behind the fibers interaction with the near-wall coherent structures, further investigations in wider domains are required.

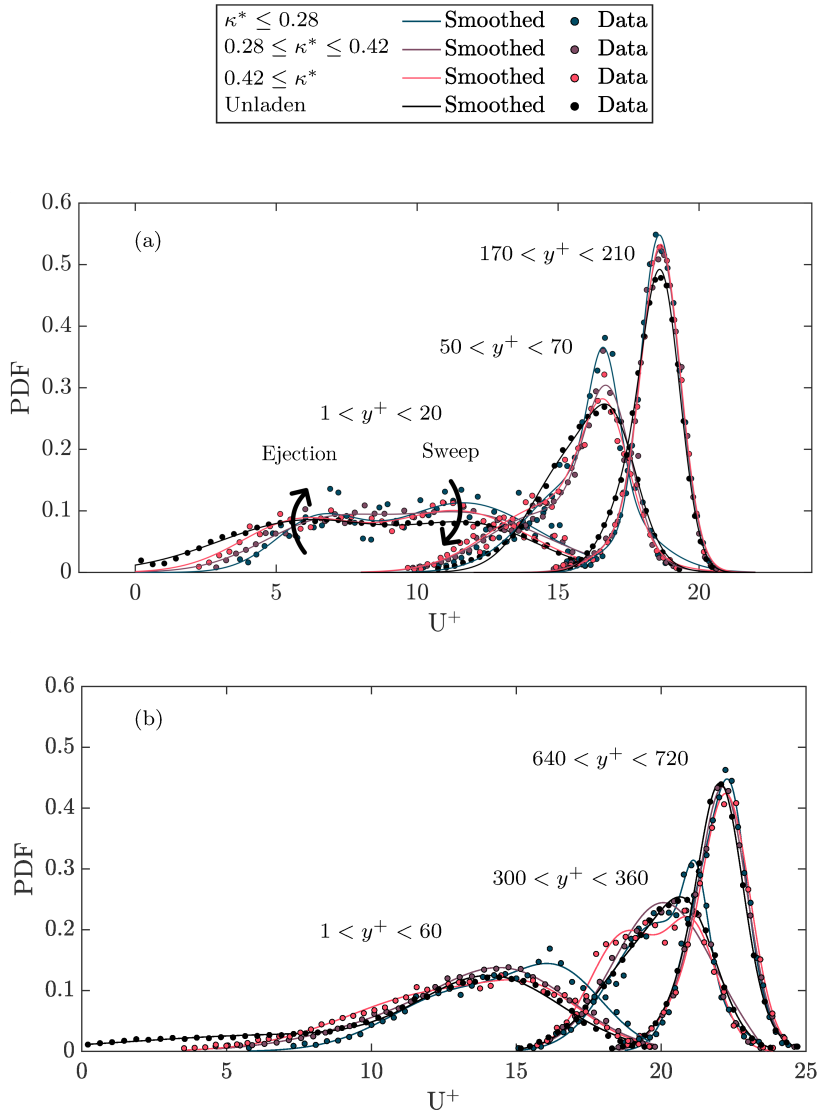

FIGURE 4.5 – PDF of streamwise velocity of fibers and unladen flow (U^+) at $\mathrm{Re}_\tau = 180$, panel (a), and at $\mathrm{Re}_\tau = 720$ shown in panel (b). Three flow regions are considered: near-wall ($1 \leq y^+ \leq 20$ for $\mathrm{Re}_\tau = 180$ and $1 \leq y^+ \leq 60$ for $\mathrm{Re}_\tau = 720$), intermediate region ($50 \leq y^+ \leq 70$ for $\mathrm{Re}_\tau = 180$ and $300 \leq y^+ \leq 360$ for $\mathrm{Re}_\tau = 720$) and channel center ($170 \leq y^+ \leq 210$ for $\mathrm{Re}_\tau = 180$ and $640 \leq y^+ \leq 760$ for $\mathrm{Re}_\tau = 720$). Fibers are divided according to their curvature, κ^*, in three classes. Values of velocity corresponding to sweeps and ejections are also indicated. Both measurements (symbols) and best-fitting functions (solid lines) are shown.

4.2.3 Orientation

In this section we investigate the orientation of the fibers at different Reynolds numbers. Fibers are classified in three classes, according to their curvature κ^*, and the results are shown in terms of the angle that the principal axis of the fibers form with the laboratory reference frame translated to the midpoint of the fiber [see also figure 2.8(b)]. In particular, figure 4.6(a,d,g) refer to the PDF of ϑ_y (angle between fibers principle axis, x', and wall-normal direction of the laboratory reference frame, y''), figure 4.6(b,e,h) refer to the PDF of ϑ_x, (angle between x' and x'') and figure 4.6(c,f,i) refer to the PDF of ϑ_z (angle between x' and z''). Both measurements (symbols) and best-fitting functions (solid lines) are shown. We considered the near-wall region, defined here as the portion of domain in which the discrepancy between the velocity of fiber-laden and unladen flow is observed (figure 4.4). PDF of the orientation angles are shown for $0 \leq y^+ \leq 20$ when $\mathrm{Re}_\tau = 180$ (a-c), $0 \leq y^+ \leq 40$ when $\mathrm{Re}_\tau = 360$ (e-g) and $0 \leq y^+ \leq 60$ when $\mathrm{Re}_\tau = 720$ (h-j). In §3.1.3, we showed that non-asymmetric fibers have bimodal distribution for the PDF of the orientation angles in the near wall region. Here, we extended the previous study and we provide a physical motivation that explains this observation.

We first consider the dynamics at low Reynolds number, $\mathrm{Re}_\tau = 180$. The angles ϑ_x and ϑ_z, shown in Figure 4.6(b,c), exhibit the same bimodal (i.e. double peak) trend reported in §3.1.3. For all classes considered, the peaks are located in correspondence of different values of ϑ_x and ϑ_z: $\vartheta_x = \pi/3$ and $\vartheta_z = \pi/6$ for $0.28 \leq \kappa^*$, $\vartheta_x = 11\pi/12$ and $\vartheta_z = \pi/12$ for $0.28 \leq \kappa^* \leq 0.42$ and $\vartheta_x = \pi/12$ and $\vartheta_z = 11\pi/12$ for $\kappa^* \geq 0.42$. However, these values are geometrically correlated, since their sum is always $\pi/2$. To motivate this, we look at figure 4.6(a), which shows that the dominant peak of ϑ_y is close to $\pi/2$, regardless of their curvature class. This indicates that the principal axis of the fiber (x') lays on a plane parallel to the channel wall, and therefore the other two orientation angles have to give $\vartheta_x + \vartheta_z = \pi/2$. We consider now the dynamics at $\mathrm{Re}_\tau = 360$, in figure 4.6(d-f). Although the value of the PDF in correspondence of $\vartheta_y = \pi/2$ is lower than in the case at $\mathrm{Re}_\tau = 180$, a bimodal behaviour for ϑ_x and ϑ_z is still observed [figure 4.6(e,f)]. Finally, for $\mathrm{Re}_\tau = 720$, the configuration $\vartheta_y = \pi/2$ is still the most probable [figure 4.6(g)], i.e. the principal axis of the fibers is on a plane parallel to the wall, but in this case the PDF is less sharp, indicating a more random distribution of the fibers orientation. However, also here the double peak is visible in the distribution of the ϑ_x and ϑ_z [figure 4.6(h,i)].

We speculate that, the reason behind these bimodal trends is fibers preferential orientation in sweep and ejection structures of the near wall region. In order to investigate this, we ensemble the fibers in two groups labeled as ascending and descending fibers. Joint PDFs of stream-wise velocity and the angle between fibers principle axis (x') and span-wise axis of laboratory reference frame (z''), ϑ_z, within $0 \leq y^+ \leq 20$ for $\mathrm{Re}_\tau = 180$ are shown in figure 4.7. Figure 4.7(a-c) refer to the joint PDF of fibers for all three curvature classes, regardless of the ascending or descending motion. The angles representing the peaks in these panels are equivalent to the peaks reported in figure 4.6(c). Descending fibers, joint PDF shown in figure 4.7(d-f), which should be mainly carried down to the wall by sweep motions, have a peak referring to $10 \leq U^+ \leq 14$. This is in agreement with the data reported in figure 4.5 and marked as sweep. Descending straighter fibers, $\kappa^* \leq 0.28$, have peak corresponding to $\vartheta_z = \pi/6$,

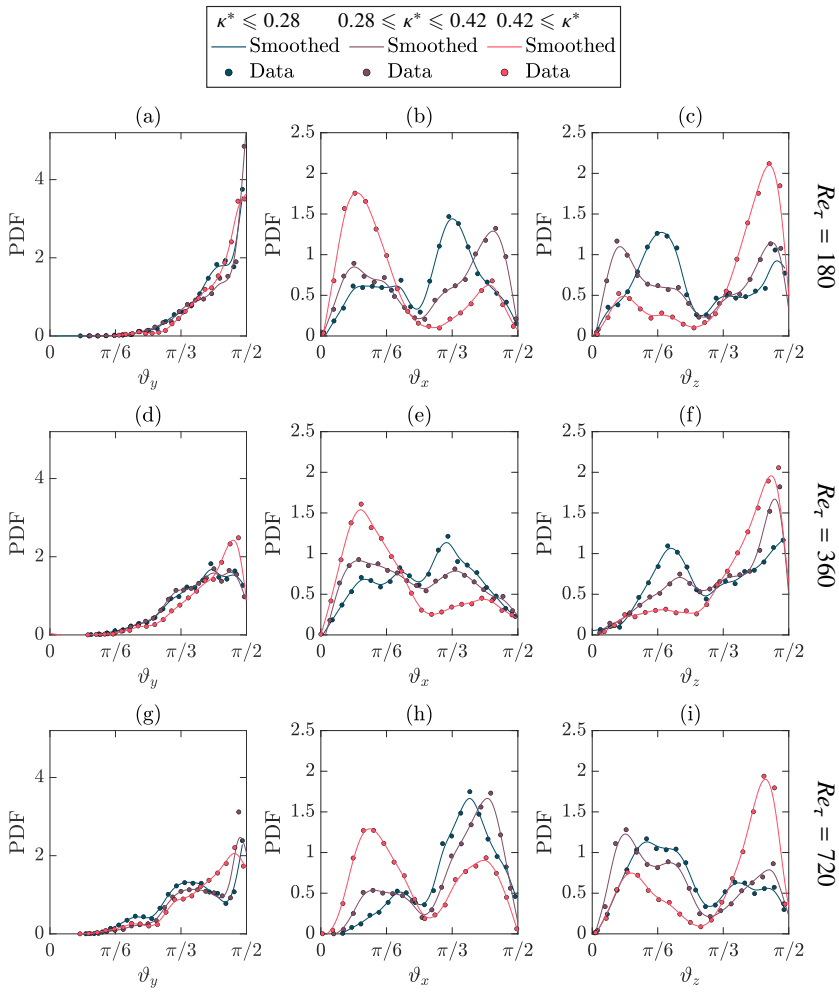

FIGURE 4.6 – PDF of the orientation angles of the fibers (divided according to their curvature in three classes) in the near-wall region, identified as $0 \leq y^+ \leq 20$ for $\mathrm{Re}_\tau = 180$ (a-c), $0 \leq y^+ \leq 40$ for $\mathrm{Re}_\tau = 360$ (e-g) and $0 \leq y^+ \leq 60$ for $\mathrm{Re}_\tau = 720$ (h-j). Orientation angles are defined by ϑ_x, ϑ_y and ϑ_z, and are shown in the left, central and right columns, respectively. Both measurements (symbols) and best-fitting functions (solid lines) are shown.

shown in figure 4.7(d), where fibers in $0.28 \leq \kappa^* \leq 0.42$ class, figure 4.7(e), show more scatter PDF data and their the peak refers to a value close to $\vartheta_z = 11\pi/12$. Unlike these classes, curved fibers, shown in figure 4.7(f), have a strong peak for a angle close to $\vartheta_z = 11\pi/12$ while they are descending. Based on these observations, descending straight fibers tend to not aligned their principle axis with flow's stream-wise direction, unlike the curved ones. The intermediate curvature class, 4.7(f), represents a transition between straight to curved fibers and therefore its PDF is more scatter compared to the others. Joint PDF of the ascending fibers, presented in figure 4.7(g-i), have a peak referring to $4 \leq U^+ \leq 8$, in agreement with the data reported in figure 4.5 and marked as ejection. Unlike descending, straighter fibers show a stronger peak close to $\vartheta_z = \pi/2$, figure 4.7(g), indicating their tendency to align parallel with the stream-wise direction of the flow while they are carried up by ascending motions. This could be due to their lower stream-wise velocity and therefore, having longer time to set their principle axis aligned with the flow direction within their resident time in the near wall region. The same trend is visible by referring to figure 4.7(h), where we can see a peak corresponding to angle close $\vartheta_z = \pi/2$ for $0.28 \leq \kappa^* \leq 0.42$, gets stronger compare to descending case. The situation remain consistent for the curved fibers, figure 4.7(h), where the peak angle is the same for both ascending and descending cases. These data suggest that, different preferential orientation induced by sweep and ejection is the reason behind strong (for $\kappa^* \leq 0.28$ and $0.28 \leq \kappa^* \leq 0.42$) and weak ($0.42 \leq \kappa^*$) bimodal behaviour of the PDF data reported in figure 4.6.

Non-axisymmetric fibers used in this study can be described on a 2D plane as it is shown in figure 4.8(a). We showed that in near wall region curved fiber's principle axis (x') is predominantly parallel to the wall and $\vartheta_y \approx \pi/2$, figure 4.6(a,d,g). This observation does not mean that the plane containing the fiber is also moving parallel to the wall. To investigate the orientation of the plane of the fibers, we introduce a new angle, angle created by the axis perpendicular to the fibers's plane (y') and the wall normal axis of the laboratory reference frame, (y''). This angle is named γ and is shown alongside ϑ_y on figure 4.8(a). We plot the joint PDF of the γ and ϑ_y of the fibers with curvature class of $\kappa^* \geq 0.42$ for $\mathrm{Re}_\tau = 180$ and $\mathrm{Re}_\tau = 720$ in two different region of the channel height, near-wall ($0 \leq y^+ \leq 20$ for $\mathrm{Re}_\tau = 180$ shown in figure 4.8(b) and $0 \leq y^+ \leq 60$ for $\mathrm{Re}_\tau = 720$ in figure 4.8(c)) and channel center (shown for $170 \leq y^+ \leq 210$ for $\mathrm{Re}_\tau = 180$ in figure 4.8(d) and for $660 \leq y^+ \leq 740$ for $\mathrm{Re}_\tau = 720$ in figure 4.8(e)). Figure 4.8(b) shows that most probable orientation of the principle axis and the fiber plane in the near wall region for $Re_\tau = 180$ is $\vartheta_y \approx \pi/2$ and $\pi/3 \leq \gamma \leq \pi/2$, respectively. This suggest that curved fibers moves parallel to wall but their plane is almost perpendicular to the channel wall. This behaviour bears similarities with what has been reported by means of numerical simulation for the near-wall orientation of oblate inertial spheroids in the channel flow [86, 20]. While curved fibers show preferential orientation for γ in the near wall region, in channel center, PDF data is scattered and randomly distributed, figure 4.8(c). In figure 4.8(d), we can see the most probable orientation of the principle axis and the fiber plane in the near wall region for $\mathrm{Re}_\tau = 720$ is close to $\vartheta_y \approx \pi/2$ and $\pi/3 \leq \gamma \leq \pi/2$, same as $\mathrm{Re}_\tau = 180$, but with shorter peak range and more scattered distribution. In center, same as $\mathrm{Re}_\tau = 180$, we see a random distribution for the joint PDF data of $\mathrm{Re}_\tau = 720$, shown in figure 4.8(e). We can conclude that, in center, regardless of the Re_τ, fibers

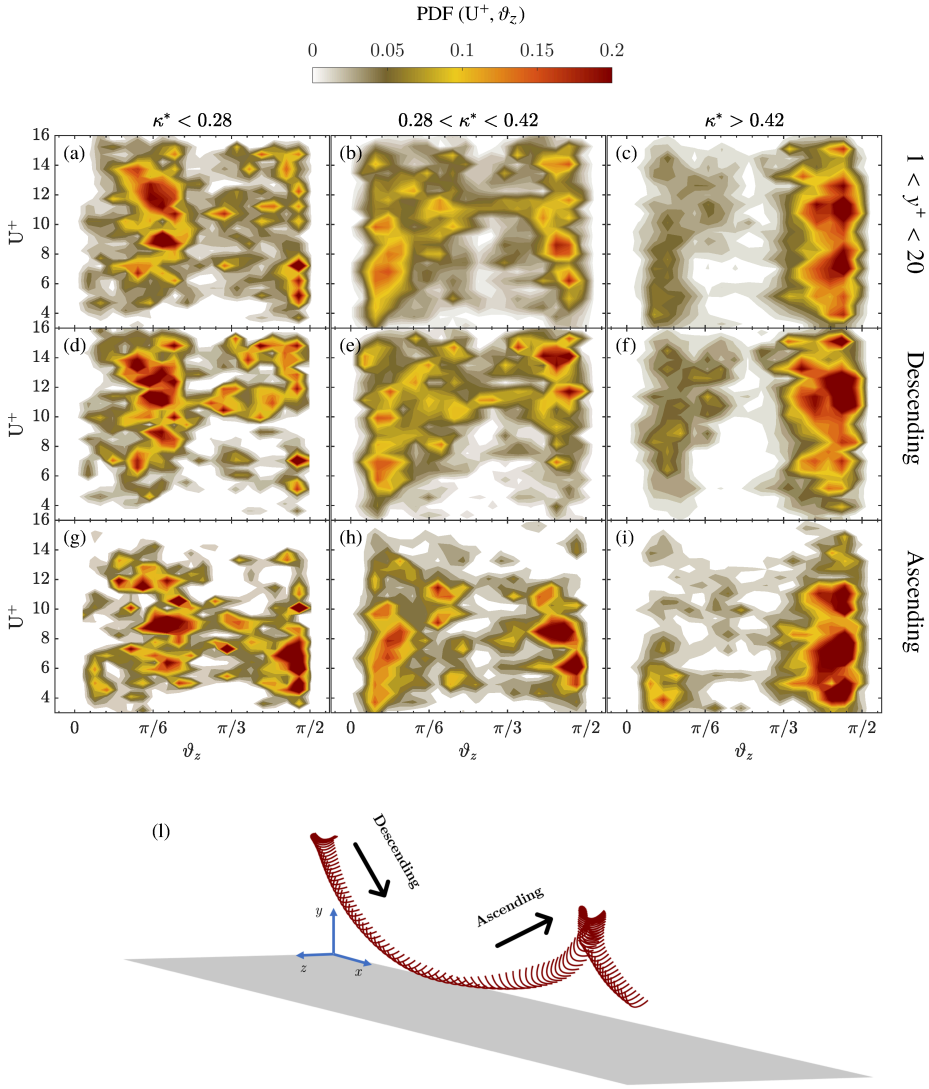

FIGURE 4.7 – Joint-PDF of fibers streamwise velocity (U^+) and spanwise orientation (ϑ_z) in the near-wall region ($0 \leq y^+ \leq 20$) for $\mathrm{Re}_\tau = 180$. Fibers are classified in three curvature classes, with curvature κ^* increasing from left to right. Joint-PDFs are shown considering all the fibers (a-c), fibers moving downward [descending with respect to the channel wall, (d-f)] or upward [ascending with respect to the channel wall, (g-i)]. Schematic of a fiber influenced by descending and ascending motions is shown in panel (l).

tend to have random orientation for both principle axis, ϑ_y,and plane, γ , orientation. Story is different in the near-wall region, where fibers tend to flow parallel to the wall with a plane orientation predominately in the range of $\pi/3 \leq \gamma \leq \pi/2$.

4.2.4 Rotational dynamics

In this section, we present first the rotation rate about the axis of the laboratory reference frame and later examining the rotation rate about the fibers frame system, i.e. tumbling and spinning, as function of curvature and for $\mathrm{Re}_\tau = 180$, $\mathrm{Re}_\tau = 360$ and $\mathrm{Re}_\tau = 720$. Stream and spanwise averaged rotation rates of the fibers, classified in three different ranges of curvature, are presented in figure 4.9. Angular velocities, $|\dot{\vartheta}_x|, |\dot{\vartheta}_y|$ and $|\dot{\vartheta}_z|$, are depicted on figure 4.9(a). Panels 4.9(b),(c) and (d) refer to the rate of change of ϑ_x, ϑ_z and ϑ_y for $\mathrm{Re}_\tau = 180$, panels 4.9(e),(f) and (g) refer to the rate of change of ϑ_x, ϑ_z and ϑ_y for $\mathrm{Re}_\tau = 360$ and panels 4.9(h),(i) and (j) refer to the rate of change of ϑ_x, ϑ_z and ϑ_y for $\mathrm{Re}_\tau = 720$, respectively. In particular, the $x - z$ averaged angular velocities, $|\dot{\vartheta}_x^+|, |\dot{\vartheta}_y^+|$ and $|\dot{\vartheta}_z^+|$, are defined as the mean value computed over horizontal planes of $|\partial\vartheta_x/\partial\tau|, |\partial\vartheta_y/\partial\tau|$ and $|\partial\vartheta_z/\partial\tau|$, respectively.
Same as data reported in §3.5, for all Re_τ, non-axisymmetric fibers rotate faster compared to straight rods, for all components considered and all along the channel height. The magnitude of the rotation rates also is consistent and close to each other for all Re_τ cases. We observe that, for the curvature classes considered, a nearly constant difference in the magnitude of the three rotation rates, regardless of Re_τ. Moreover, the magnitude of the rotation rate increases by approaching the wall. Another important observation is regarding panels 4.9(d),(g) and (j), referring to the rate of change of ϑ_y of $\mathrm{Re}_\tau = 180$, $\mathrm{Re}_\tau = 360$ and $\mathrm{Re}_\tau = 720$, respectively. In these panels, we can observe a nearly constant rate of change for ϑ_y the near wall region, $|\dot{\vartheta}_y^+| \approx 0.03$.
The effect of curvature on the tumbling rate has been investigated in §3.1.4, where it was shown that, in case of non-axisymmetric fibers, curvature plays a crucial role. We consider here the effect of the shear Reynolds number, Re_τ, on the tumbling of the fibers, and we investigate the entire channel extensions, $0 \leq y^+ \leq \mathrm{Re}_\tau$. A possible reference frame for axis-symmetric particles consists of their three main axis, i.e. the symmetry axis (x') and two perpendicular axis (y', z'). Therefore, the solid body rotation rate of axis-symmetric particles, $\boldsymbol{\Omega} = \boldsymbol{\omega}_x + \boldsymbol{\omega}_y + \boldsymbol{\omega}_z$, can be decomposed into a component $\boldsymbol{\omega}_x$ aligned with the symmetry axis (x'), called spinning, and two components ($\boldsymbol{\omega}_y$ and $\boldsymbol{\omega}_z$) perpendicular to the symmetry axis and aligned with y' and z', defined as tumbling [85]. Since curved fibers have no symmetry axis, we arbitrarily define the spinning as the rotation rate about the principal fiber axis (x') and the two tumbling components as the rotation about y' and z'. The configuration is shown in figure 2.8(b). The solid body rotation, $\boldsymbol{\Omega}$, can be split in spinning and tumbling components, respectively $\boldsymbol{\Omega}_s$ and tumbling $\boldsymbol{\Omega}_t$, so that

$$\boldsymbol{\Omega} = \boldsymbol{\omega}_x + (\boldsymbol{\omega}_y + \boldsymbol{\omega}_z) = \boldsymbol{\Omega}_s + \boldsymbol{\Omega}_t \tag{4.1}$$

with squared magnitude:

$$\Omega_s \Omega_s = \boldsymbol{\omega}_x \cdot \boldsymbol{\omega}_x = \omega_x^2 \tag{4.2}$$

$$\Omega_t \Omega_t = \boldsymbol{\omega}_y \cdot \boldsymbol{\omega}_y + \boldsymbol{\omega}_z \cdot \boldsymbol{\omega}_z = \omega_y^2 + \omega_z^2. \tag{4.3}$$

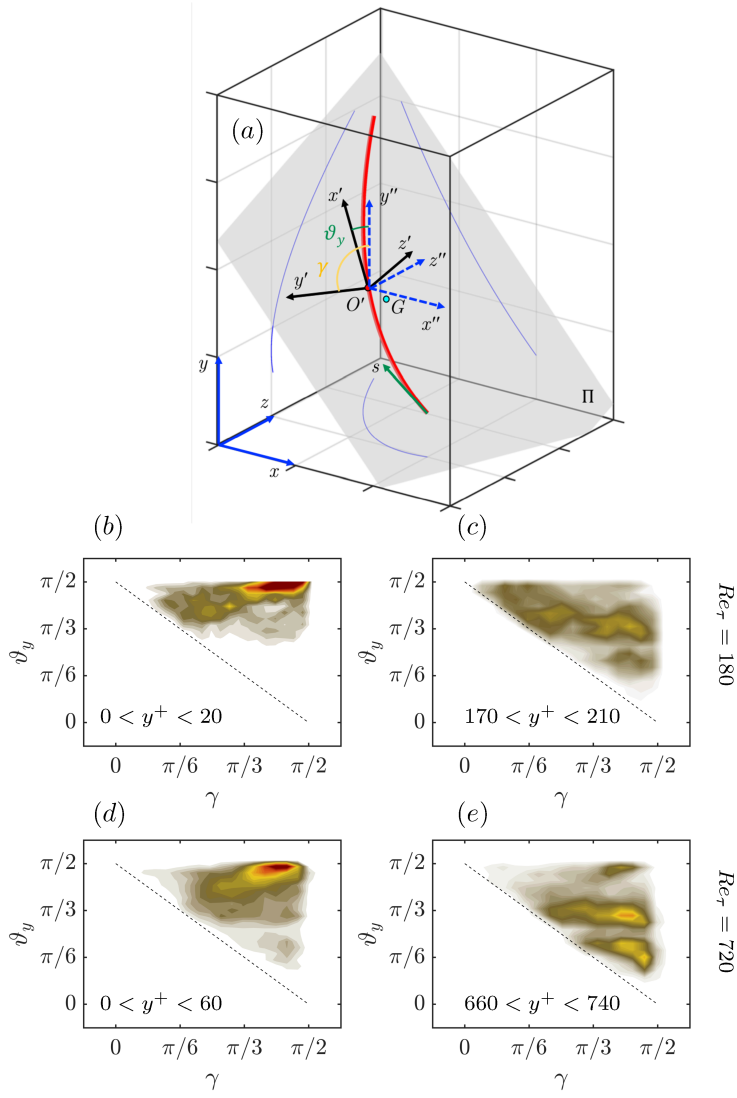

FIGURE 4.8 – (a) Orientation of the plane containing the fiber (Π) with respect to the channel reference frame (xyz). The angle formed by y', i.e. the vector perpendicular to Π, with y'', i.e. the global reference frame translated to the midpoint of the fiber, is defined with γ and is here indicated. The angle ϑ_y, formed by y'' with the principal axis of the fiber, is also indicated. (b-e) Joint PDF of γ and ϑ_y for $Re_\tau = 180$ (b-c) and $\mathrm{Re}_\tau = 720$ (d-e). Two different region of the flow are shown: near-wall (b,d) and center (c,e). The limits considered in terms of y^+ are also indicated.

Hereinafter, we will consider the mean square tumbling rate $\langle \Omega_t \Omega_t \rangle$, i.e. the tumbling rate $\Omega_t \Omega_t$ defined as in Eq. (4.3) and averaged in horizontal direction, so that the results can be shown as a function of y^+ (figure 4.10). We provide the statistics of mean tumbling expressed in wall-units, $\langle \Omega_t^+ \Omega_t^+ \rangle = \langle \Omega_t \Omega_t \rangle \tau^2$, with $\tau = \delta / u_\tau$ reported in table 4.1 for all experiments considered. Finally, to compute the tumbling from the experimental measurements we employed a second-order polynomial as time filter, with constant kernel size of 2.8τ, and we consider fibers that are tracked for at least 5τ. We observed that different values of kernel size can give tumbling rates that are different in magnitude, but the qualitative behaviour of the tumbling is not affected. Effect of kernel size of the filtering on the statistics is thoroughly analysed in §5.2.
First, we consider the measurements performed at $\mathrm{Re}_\tau = 180$ (figure 4.10a). Measurements on fibers, divided in three curvature classes, are shown by circles, whereas fitted experimental data (spline) are shown as solid lines. We observe that the the magnitude of the mean square tumbling rate, $\langle \Omega_t^+ \Omega_t^+ \rangle$, is sensitive to the distance from the wall, y^+. In particular, we observe that for all curvature classes the tumbling rate increases from center towards the wall, and this increase is larger for straight fibers ($\kappa^* \leq 0.28$) than for curved ones. We compare now our results against the direct numerical simulations performed by Zhao et al. [93]. In the simulation, ellipsoids ($\lambda = 50$, $St = 0$) in turbulent channel flow at $\mathrm{Re}_\tau = 180$ are considered, and give $\langle \Omega_t^+ \Omega_t^+ \rangle = 0.0056$ at $y^+ = 10.$. This result, shown in figure 4.10(a) as filled diamond, is in excellent agreement with the experimental measurements obtained for straight fibers ($\kappa^* \leq 0.28$).
We analyse now the measurements performed at $\mathrm{Re}_\tau = 360$, reported in figure 4.10(b). In §3, we showed that, at this value of Reynolds number, the curvature produces an increase of the tumbling rate. Moreover, we observe that also in this case the tumbling increase from center towards the wall. We compare our results with the experimental measurements proposed by Shaik et al. [78], where straight fibers are tracked in a turbulent channel flow at $\mathrm{Re}_\tau = 435$. They investigated the behaviour of fibers having Stokes numbers $St = 0.22$ ($\lambda = 31$) and $St = 0.34$ ($\lambda = 47$) considerably larger than the ones used in this study. However, when the fibers belonging to the first class are considered ($\kappa^* \leq 0.28$) the results proposed here are in fair agreement with the experimental measurements of Shaik et al. [78] for $St = 0.22$.
Finally, we consider the behaviour of the fibers at $\mathrm{Re}_\tau = 720$ in figure 4.10(c). Also in this case, the fibers tend to tumble faster approaching the walls of the channel, and the larger the curvature, the higher the tumbling rate. We can conclude that, regardless of Reynolds number, we observe that the magnitude of $\langle \Omega_t^+ \Omega_t^+ \rangle$ reduces by increasing the y^+ and this trend is less significant for curved fibers, especially in case $\mathrm{Re}_\tau = 720$ where it almost remains constant all along the channel height. Moreover, $\langle \Omega_t^+ \Omega_t^+ \rangle$ remains almost constant in the near-wall region, corresponding to $0 \leq y^+ \leq 10$, $y^+ \leq 40$ and $y^+ \leq 60$ for $\mathrm{Re}_\tau = 180$, $\mathrm{Re}_\tau = 360$ and $\mathrm{Re}_\tau = 720$, respectively.

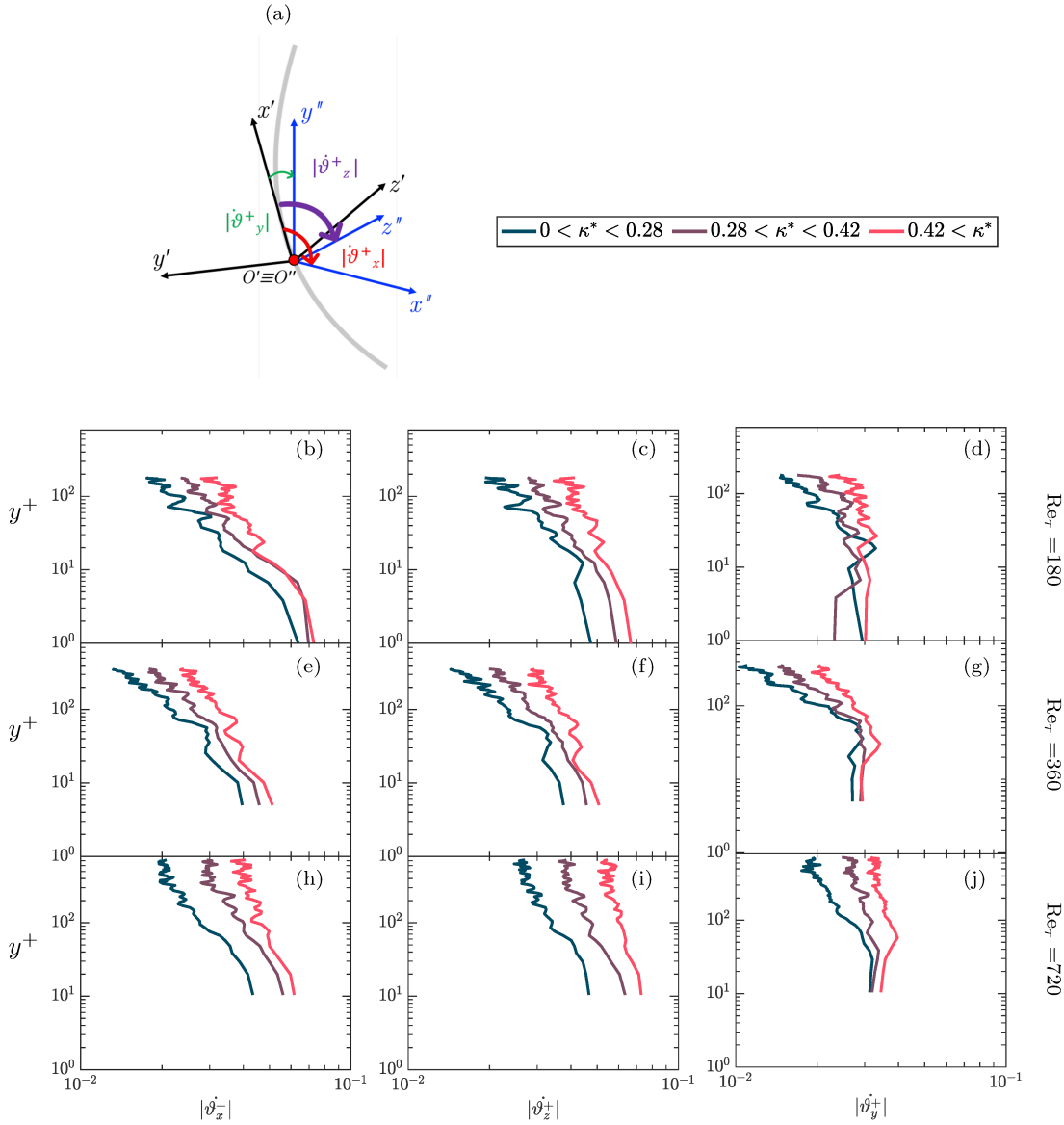

FIGURE 4.9 – $x-z$ averaged angular velocities of all three classes of fibers. The angular velocities in directions x, y and z ($|\dot{\vartheta}_x|, |\dot{\vartheta}_y|, |\dot{\vartheta}_z|$) are defined as the mean value computed over horizontal planes of $|\partial\vartheta_x/\partial t|, |\partial\vartheta_y/\partial t|$ and $|\partial\vartheta_z/\partial t|$, respectively.

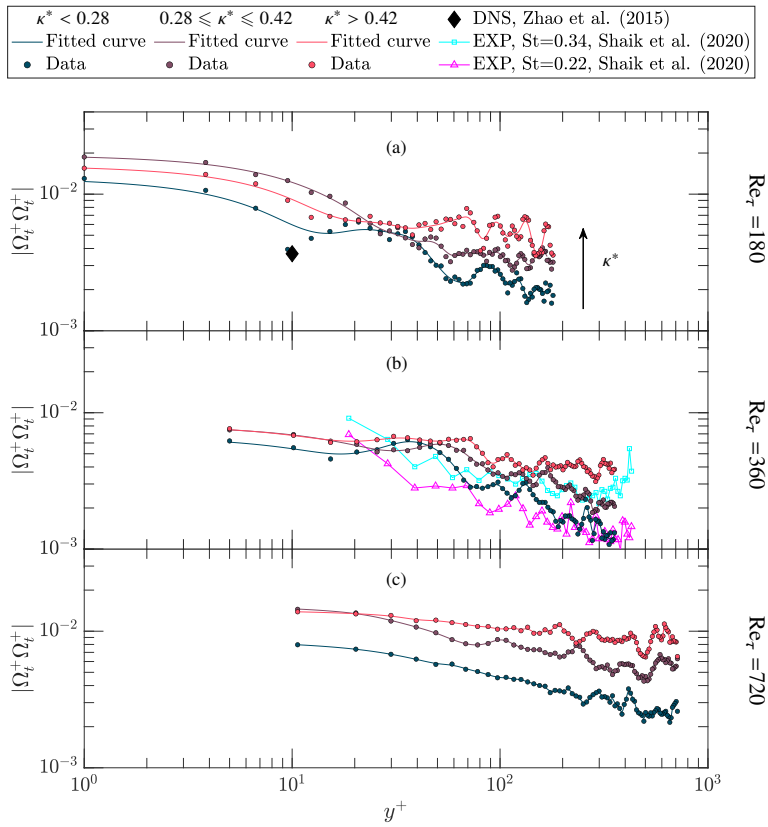

FIGURE 4.10 – $x-z$ averaged tumbling of the fibers $\langle \Omega_t^+ \Omega_t^+ \rangle$ (expressed in wall units) is shown as a function of the wall-normal coordinate, y^+. Measurements on fibers, divided in three curvature classes, are shown (circles) as well as fitted experimental data (solid lines). The three Reynolds number considered, $\mathrm{Re}_\tau = 180$, 360 and 720, are shown in panels (a), (b) and (c), respectively. Results are compared against numerical simulations [$\mathrm{Re}_\tau = 180$, $\lambda = 50$, $St = 0$, 93] and experimental measurements [$\mathrm{Re}_\tau = 435$, $St = 0.22$ and $\lambda = 31$, $St = 0.34$ and $\lambda = 12$, 78]

4.3 Conclusions

In this chapter, we investigated the effect of Reynolds number on the concentration, orientation and rotation rate of the fibers. Concentration of the fibers is influenced by the Reynolds number, and unlike the near wall reduction observed for cases $\mathrm{Re}_\tau = 180$ and $\mathrm{Re}_\tau = 360$, we observed a near wall accumulation for $\mathrm{Re}_\tau = 720$. In addition, effect of curvature in the near wall on the concentration trends is visible for all Reynolds numbers. Averaged normalised fibers concentration increases with the rate of asymmetry, in other words, curved fibers have higher concentration in near wall compared to straighter ones. We speculate that the reason behind this observation is due to different interactions of the fibers with near wall coherent structure and fiber-wall interaction.

Fibers mean stream-wise velocity profiles match the fluid velocity in the center, while by approaching to the near-wall region, a deviation from the single-phase profile is visible. By referring to the PDF data of the stream wise velocity of the fibers, we can conclude that the probability of finding fibers in the near wall region, $y^+ < 5$ for Re_τ=180, with a given curvature is a function of κ^*: curved fibers ($\kappa^* \geq 0.42$) have much higher probability than the straighter ones ($\kappa^* \leq 0.28$). Therefore, curved fibers are expected to move slowly in this region and their residence time will increase with respect to the straight ones. This could be another reason for curved fibers higher averaged normalised concentration in the near wall region.

PDF of fibers orientation, consistently showed double peak trends for all Reynolds numbers. We showed that this double peak behaviour could be due to different preferential orientation that fibers have while they are carried by descending and ascending motions of the flow in the near wall region, such as sweep and ejection. Non-axisymmetric fibers used in this study can be contained on a 2D plane. The preferential orientation of the plane angle with wall normal axis of lab reference frame, γ, is regardless of the orientation of their principal axis wall normal axis of lab reference frame, ϑ_y. We observed that, curved fibers, tend to flow parallel to the wall surface, while their plane angle ranges $\pi/3 < \gamma < \pi/2$. This observation have similarities with previously reported near wall orientation of the inertial disks.

Mean square tumbling statistics of the fibers non-dimensionalised by the viscous time scale of the flow as function of y^+, showed that regardless of the Reynolds number, $\langle \Omega_t^+ \Omega_t^+ \rangle$ increases by approaching to the wall and there is a consistent trend as a function curvature: curved fibers ($\kappa^* \geq 0.42$) tumble with higher magnitude than straighter ones ($\kappa^* \leq 0.28$). We also observed that, in the vicinity of the wall, magnitude of $\langle \Omega_t^+ \Omega_t^+ \rangle$ stays constant, regardless of the Reynolds or curvature class of the fibers.

5

Scaling laws of tumbling and spinning

In this chapter, mean square tumbling and spinning rate of the fibers, classified by their curvature are discussed. In addition to the curvature, we also classify the statistics based on the end-to-end length (named as effective length) of the fibers. In this way, we can examine the possible relation between curvature of the fiber and its effective length. Tumbling and spinning statistics are provided for three Reynolds numbers, Re_τ=180, Re_τ=360 and Re_τ=720 and effect of data filtering method (noise removal) on the statistics is also discussed. The data reported in this chapter are recorded with the same configuration as discussed in §3, §4 and shown in figure 2.1. Image acquisition, flow and fiber parameters are same as reported in the table 4.1.

5.1 Effective length

We define the effective length as the distance between two ends of the fiber, L_{eff}, where in case of the straight fibers effective length is equal to the fibers length, L_f. Assuming that the fiber is part of a circumference, one can find analytically the effective length of the fiber by knowing the curvature of the fiber, κ, and using the following correlation:

$$L_{eff} = \frac{\sqrt{(2 - 2\cos(\kappa L_f))}}{\kappa} \ . \tag{5.1}$$

If the fibers shape are symmetric with respect to z' axis (the axis perpendicular to the principal axis of the fiber, x' within the fiber plane Pi), this result must be equal to the length measured experimentally by finding the distance of the two ends of the fiber. In figure 5.1 (a), we compare the analytical prediction of L_{eff}/L_f with experimentally measured value by imposing the symmetry condition to the fibers. In other words, we use κ and L_f reconstructed from the experiments and input them to Eq. (5.1). Obviously, in this case, there is a perfect match between the analytical prediction and the measurement as it is shown in figure 5.1 (a). We can directly measure the L_{eff} by calculating the distance between two end of the polynomial fitted to the reconstructed light intensity of the fiber. Comparison of the analytical prediction and the direct measurement of the L_{eff}/L_f is shown in figure 5.1 (b). Although there is a good agreement between the analytical prediction and the measured L_{eff}/L_f, the PDF

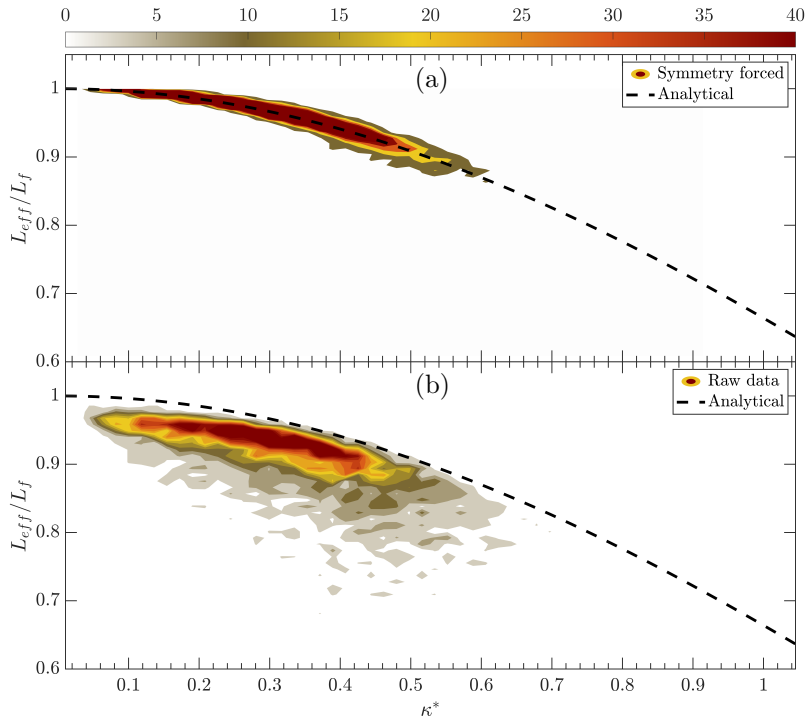

FIGURE 5.1 – Joint PDF of effective length of the fibers normalised by the fiber length with curvature distribution of the fibers examined in this study. L_{eff} is effective length (end-to-end) and L_f is the fiber length. Figure 5.1 (a), compares the analytical prediction of L_{eff}/L_f with experimentally measured value by imposing the symmetry condition. Comparison of the analytical prediction and the direct measurement of the L_{eff}/L_f is shown in figure 5.1 (b).

data is much more scatter in this case. This is due to the asymmetrical distribution of the curvature along the fiber length. In such a case, the curvature could be same as a case with symmetrical distribution but the effective length is different.
The curvature $\kappa_l(s)$ is defined locally as a function of the arc length coordinate, s. To evaluate the rate of asymmetry of the fiber, one can compute the following integral

$$I_f^* = \int_0^{L_f/2} |\kappa_l(s) - \kappa_l(L_f - s)| \mathrm{d}s,$$

which gives an indication of the rate of asymmetry of the fiber in terms of curvature ($I_f^* = 0$ means perfect symmetry with respect to the geometrical center of the fiber, located at $s = L_f/2$). We can also relate the rate of asymmetry I_f^* to the average curvature κ^* of the fiber by looking at the joint probability density distribution reported in figure 5.2. We observe that a correlation exists between the average curvature κ^* and the symmetry indicator I_f^* and the rate of asymmetry increases by increasing the curvature for the fiber dataset used in this study. However, to have a clear picture of

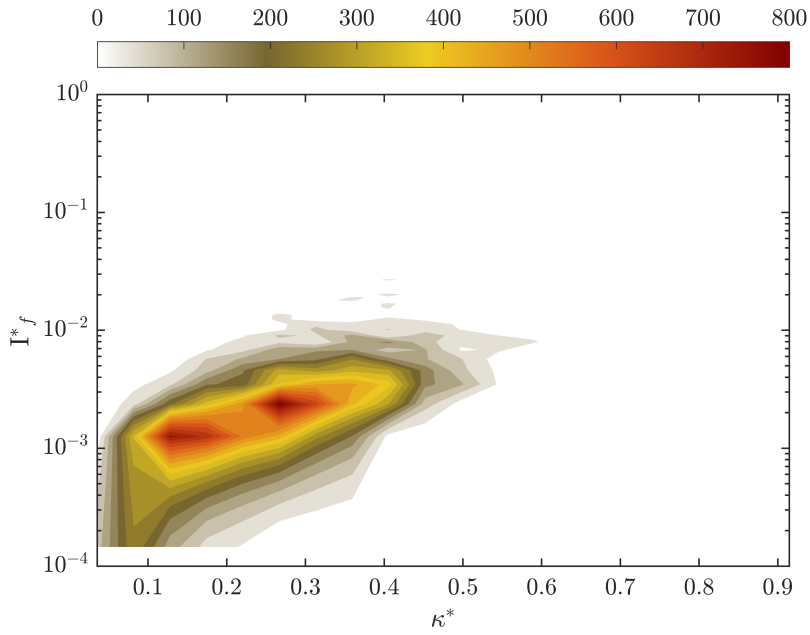

FIGURE 5.2 – Joint PDF of effective length of the fibers normalised by the fiber length with curvature distribution of the fibers examined in this study. L_{eff} is effective length (end-to-end) and L_f is the fiber length.

the role of asymmetry, a larger database is required.

5.2 Effect of kernel size on noise removal

Like every experimental measurement, data obtained from this study needs to be filtered by using fitting methods. For providing high order statistics like tumbling and spinning, effect of noise removal from the data is prominent, it can cause a significant error of bias in terms of the magnitude of the statistics. Channel flow configuration, by considering the criteria of covering full h of the channel, has restrictions in terms of non equal time scale of the flow compared to the experiments done in Homogeneous Isotropic Turbulence (HIT) configuration. Moreover, due to constant spatial resolution and strong mean flow, causing the tracks to be passive (entering from one side and exiting from the other side of the domain), tracks length are also restricted and shorter compared to HIT. This means that imposing a same kernel window size, K_w, in terms of snapshot number, to all tracks, has different weight in terms of flow time scale on the tracks depending on the location of the track within the channel height. Example evolution of the ϕ, component of Euler angles being used to calculate the tumbling, for a track in the near wall region and center of the channel is shown in figure 5.3

and figure 5.4, respectively. Raw data is smoothed by using different kernel window sizes and second order Savitzky-Golay filter. Figures 5.3(a-e) and 5.4(a-e) represent the K_w of 18, 36, 50, 100 and 150 snapshots. Their equivalent time scale based on viscous time scale, τ and Kolmogorov time scale, τ_k, are written in each panel. It is obvious that by increasing the K_w, we underestimate the magnitude and rate of change of the ϕ, figure 5.3(d,e), unlike the case of figure 5.3(a-c) corresponding to margin of $0.1 \leq K_w \leq 0.5\tau_k$. In other words, in the near wall region, $K_w \geq \tau_k$ underestimates the trend and the best window size should be chosen by relying on the viscous time scale, $K_w \approx \tau \approx 0.3\tau_k$. This trend is different for the tracks in the center of the channel, figure 5.4, where we can observe an overestimation for the trend in case of shorter kernels, $K_w \leq \tau$, figure 5.4(a,b), while for longer kernel sizes, figure 5.4(c-e), it does not underestimate the trend significantly. This suggest that, K_w in terms of snapshot for each track should be chosen based on local time scale of the flow surrounding the fiber track. In order to investigate the possible effect of variable kernel size on the statistics of tumbling spinning, we propose the following procedure:

- For each Re_τ, find the K_w in the near wall region by relying on a margin close to viscous time scale, e.g: $0.6\tau \leq K_w \leq 1.4\tau$. Near wall region could be defined to be $0 \leq y^+ \leq 20$, $0 \leq y^+ \leq 40$ and $0 \leq y^+ \leq 60$ for $\mathrm{Re}_\tau = 180$, $\mathrm{Re}_\tau = 360$ and $\mathrm{Re}_\tau = 720$, respectively.

- Find the equivalent range of the K_w in the near wall in terms of Kolmogorov time scale, e.g. $0.6\tau \leq K_w \leq 1.4\tau \approx 0.15\tau_k \leq K_w \leq 0.4\tau_k$.

- Only keep tracks $\gtrapprox 0.4\tau_k$ for all Re_τ and all along the channel height.

- Define a mean height for each track $\langle y^+_{fiber} \rangle$.

- Discretise the domain to a specific margins of y^+, $y^+_{i-1} \leq y^+_i \leq y^+_{i+1}$.

- Find all tracks fitting to $y^+_{i-1} \leq \langle y^+_{fiber} \rangle \leq y^+_{i+1}$ for each curvature class, $\kappa^* < 0.28$, $0.28 < \kappa^* < 0.42$ and $\kappa^* > 042$.

- Define the tracks local Kolmogorov time scale by correlating to the DNS data, [57, 36].

- Impose the K_w as filter width in terms of snapshot to the Euler angles evolution of the track, by using the margin found based on Kolmogorov time scale in the near wall region, $0.15\tau_k \leq K_w \leq 0.4\tau_k$, i.e. for each track based on its $\langle y^+_{fiber} \rangle$, $0.15\tau_k \leq K_w \leq 0.4\tau_k$ corresponds to different snapshot number.

- Calculate the tumbling and spinning, $\Omega_t\Omega_t = (\boldsymbol{\Omega}_t \cdot \boldsymbol{\Omega}_t) = (\omega_y^2 + \omega_z^2)$ and $\Omega_s\Omega_s = (\boldsymbol{\Omega}_s \cdot \boldsymbol{\Omega}_s) = (\omega_x^2)$, for each track and repeat it for the data obtained by considering K_w range.

- Calculate the mean and non-dimensiolise the tumbling and spinning by the local Kolmogorov time scale, $\langle \Omega_t\Omega_t \rangle \tau_k^2$ and $\langle \Omega_s\Omega_s \rangle \tau_k^2$ or with viscouse timescale, $\langle \Omega_t^+\Omega_t^+ \rangle$ and $\langle \Omega_s^+\Omega_s^+ \rangle$.

- Define the $L^* = L_{eff}/L_k$ for each track, where L_k refers to the local Kolmogorov length scale.

Since $0.4\tau_k$ means different number of snapshots for each Re_τ, and we have a limitation in terms of spatial resolution, it causes a significant reduction in terms of number of tracks specially for the $\mathrm{Re}_\tau = 180$. We would like to clarify the reason behind the above mentioned spatial resolution limitation. Indeed to reconstruct the fibers with a good accuracy, specially for the polynomial fitting process and curvature detection, we are restricted in terms of scale factor ($pixel/mm$), i.e. we need sufficient number of voxels to represent the fibers in the reconstructed volume. In other words, we could not locate the cameras far away to have more length in stream-wise direction and consequently longer tracks, by sacrifying the scale factor. In addition, we could not use optical lens with higher focal length (higher optical zoom), since we wanted to keep the full h of the channel within the frame of the camera. Another restriction that we would like to mention, is the sensor crop required to obtain the appropriate time resolution, which is very important for $\mathrm{Re}_\tau = 720$. This crop size, and the time frequency reported in table 4.1, was the optimal situation satisfying the above mentioned limits in terms of spatial resolution for $\mathrm{Re}_\tau = 720$: covering full h and not loosing too much from the scale factor.
Summary of the number of tracks, parameters used for the filtering such as the maximum K_w range available at center and corresponding meaning of $0.15\tau_k \leq K_w \leq 0.4\tau_k$ range in terms of snapshot for channel center, used in this section to provide the results are shown in table 5.1. Hereafter, Constant K_w refers to the case where the kernel is constant all along the channel regardless of the fibers $\langle y^+_{fiber} \rangle$ and adaptive filtering refers to $0.15\tau_k \leq K_w \leq 0.4\tau_k$ where the kernel size in terms of snapshot is variable based on the $\langle y^+_{fiber} \rangle$ of the fiber track.

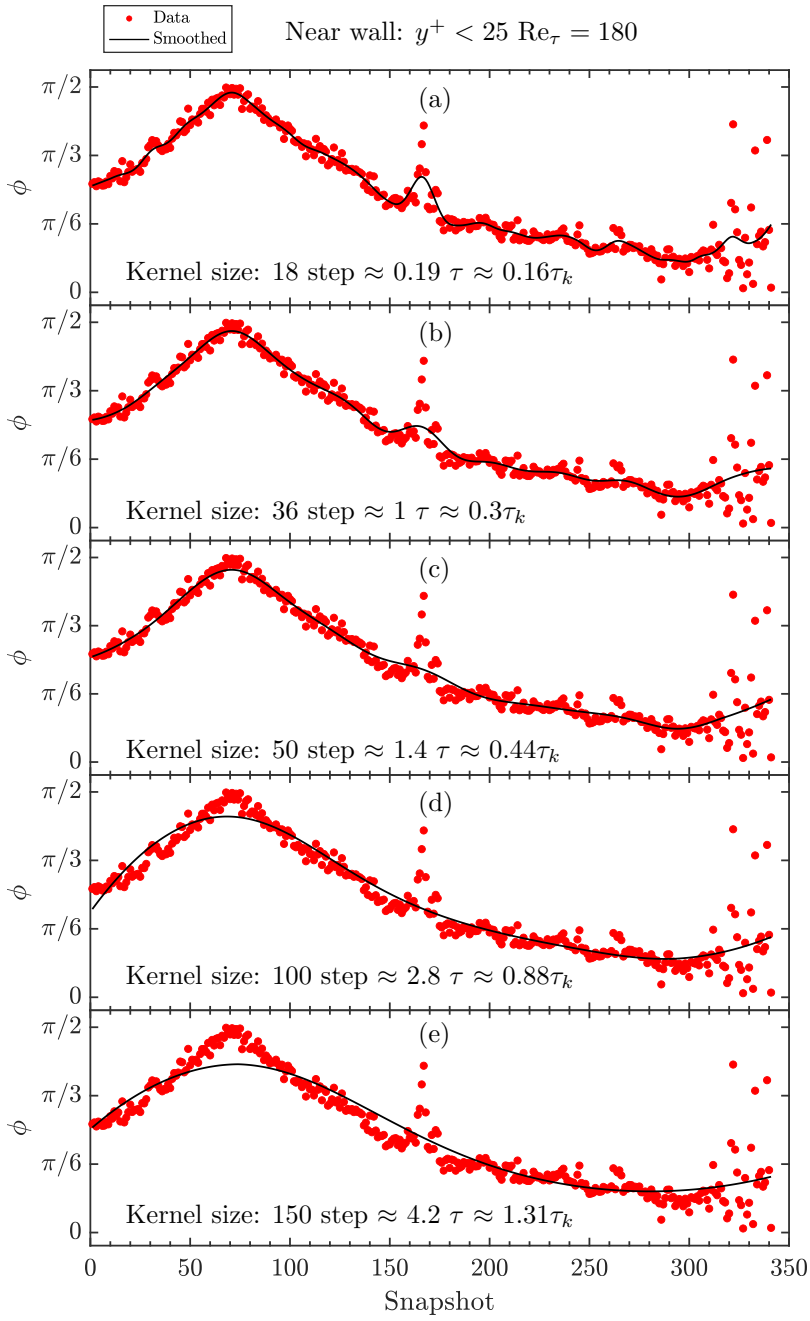

FIGURE 5.3 – Example of the evolution of the ϕ, for a track in the near wall region. Equivalent time scale based on viscous time scale, τ and Kolmogorov time scale, τ_k, are written in each panel. By increasing the K_w, we underestimate the magnitude and rate of change of the ϕ, figure 5.3(d,e), unlike the case of figure 5.3(a-c) corresponding to margin of $0.1 \leq K_w \leq 0.5\tau_k$.

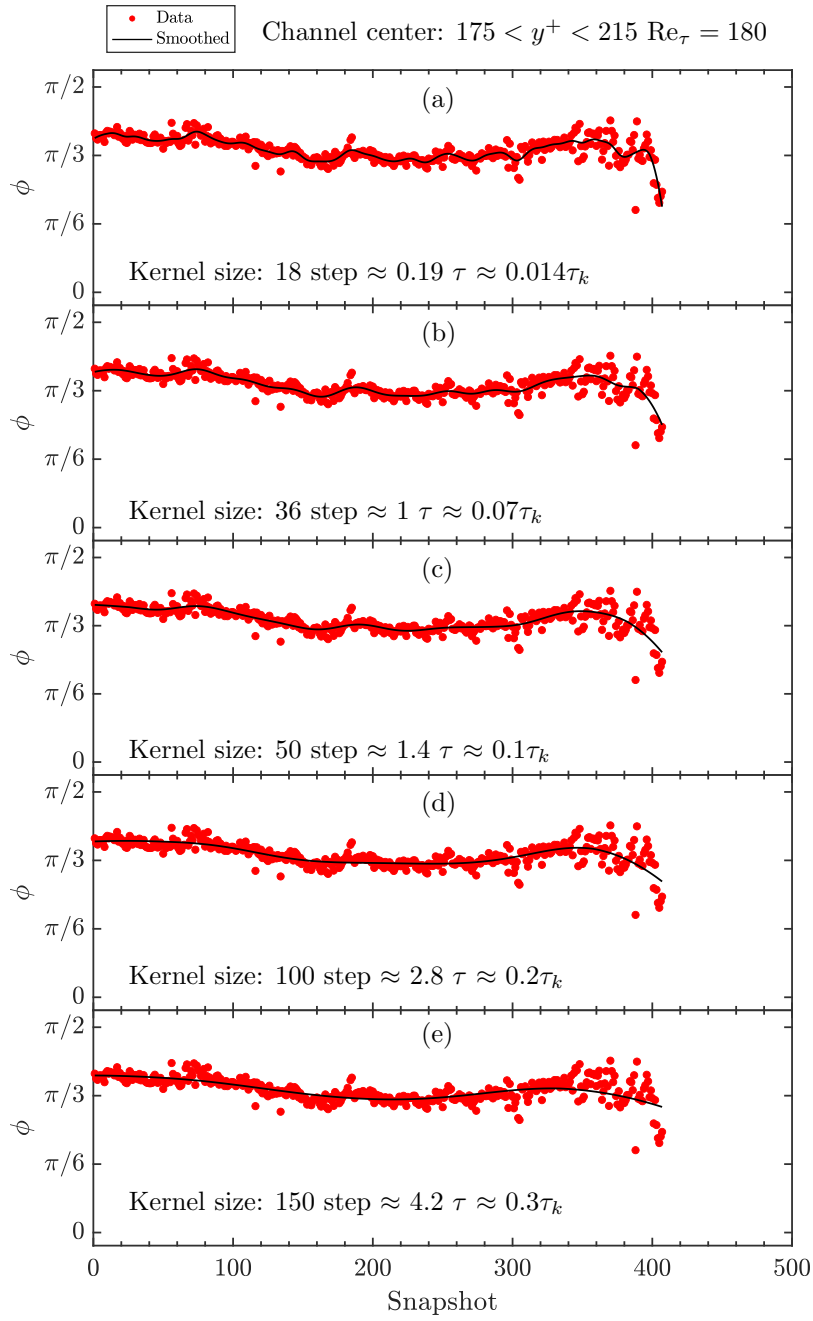

FIGURE 5.4 – Example of the evolution of the ϕ, for a track in the channel center. equivalent time scale based on viscous time scale, τ and Kolmogorov time scale, τ_k, are written in each panel. We can observe an overestimation for the trend in case of shorter kernels, $K_w \leq \tau$, figure 5.4(a,b), while for longer kernel sizes, figure 5.4(c-e), it does not underestimate the trend significantly.

Re_τ	Curvature	Total tracks	Tracks $\geq 0.4\ \tau_k$ Tracks $\geq 6\ \tau$	Tracks in center	K_w limits in center [s]	$0.15\tau_k \leq K_w \leq 0.4\tau_k$ in center [snaphsot]
180	$\kappa^* < 0.28$	13992	2261	354	$0 < K_w \leq 0.4\tau_k$	$80 \leq K_w \leq 200$
	$0.28 < \kappa^* < 0.42$	21205	2938	450		
	$\kappa^* > 042$	14541	2050	360		
360	$\kappa^* < 0.28$	7187	4599	749	$0 < K_w \leq 0.54\tau_k$	$64 \leq K_w \leq 144$
	$0.28 < \kappa^* < 0.42$	11848	7242	957		
	$\kappa^* > 042$	8556	4877	949		
720	$\kappa^* < 0.28$	11368	4792	613	$0 < K_w \leq 1.14\tau_k$	$26 \leq K_w \leq 68$
	$0.28 < \kappa^* < 0.42$	17841	7692	720		
	$\kappa^* > 042$	10108	3822	610		

TABLE 5.1 – Summary of the tracks number, classified based on curvature of the fibers, and kernel size limits used in this study for all three Re_τ. Center region is considered as: $175 \leq y^+ \leq 215$, $320 \leq y^+ \leq 400$ and $640 \leq y^+ \leq 760$ for $\mathrm{Re}_\tau = 180$, $\mathrm{Re}_\tau = 360$ and $\mathrm{Re}_\tau = 720$, respectively. These margins are chosen based on effective Reynolds number, $Re_{\tau,\mathrm{eff}}$. K_w range available at center, in terms of τ_k, and corresponding meaning of $0.15\tau_k \leq K_w \leq 0.4\tau_k$ range in terms of snapshot in the channel center is provided in column six and seven.

5.3 Results

In this section we present the statistics of mean square tumbling and spinning rate by using constant, $K_w \approx 2.8\tau$, and adaptive kernel size, $0.15\tau_k \leq K_w \leq 0.4\tau_k$. Fibers are classified based on curvature and effective length of the fibers.

5.3.1 Tumbling

Majority of the available statistics in literature regarding the mean square tumbling rate magnitude, are in HIT configuration and the reported value for inertialess fibers is close to $\langle\Omega_t\Omega_t\rangle\tau_k^2 \approx 0.1$ [66, 64, 54]. Based on the author knowledge, the only reported statistics of the mean square tumbling rate value of the fibers in channel flow non-dimensiolised by Kolmogorov time scale and reported for the channel center, is provided by Zhao et al. [93] and done by means of DNS. This result is in agreement with the reported results for HIT configuration, $\langle\Omega_t\Omega_t\rangle\tau_k^2 \approx 0.1$. In order to compare our results, we first plot the tumbling values in the channel center, where theoretically should have similarities with HIT conditions. In figure 5.5, we plot the Mean square tumbling rate of fibers, non-dimensionlised by the local Kolmogorov time scale, $\langle\Omega_t\Omega_t\rangle\tau_k^2$, for $\mathrm{Re}_\tau = 180$, $\mathrm{Re}_\tau = 360$ and $\mathrm{Re}_\tau = 720$, in $175 \leq y^+ \leq 215$, $320 \leq y^+ \leq 400$ and $640 \leq y^+ \leq 760$, respectively. For $\mathrm{Re}_\tau = 180$, data $0.15\tau_k \leq K_w \leq 0.4\tau_k$ are shown in blue error bar and the mean value of this range is shown by blue circle while the data representing constant Kernel of $K_w \approx \tau$ is shown with black circles. In the same way, data of $\mathrm{Re}_\tau = 360$ are shown in red error bar, red and black square markers while data of $\mathrm{Re}_\tau = 720$ are presented in green error bar, green and black diamond markers. All data are classified in three curvature classes, $\kappa^* < 0.28$, $0.28 < \kappa^* < 0.42$ and $\kappa^* > 0.42$. Curvature magnitude representing each class, is chosen based on the weighted average of each curvature class, therefore it slightly differs depending on the dataset of each Re_τ.

First observation from this plot is, regardless of using constant or adaptive filter, mean square tumbling rate is increasing by increasing the curvature value. This is in agreement with what we reported in §3, figure 3.9, regarding the effect of curvature on the mean square tumbling rate of fibers, where curved fibers show higher magnitudes of mean square tumbling rate. Although the trend is same for both cases of the filtering, the story is different for the magnitude and there is a significant difference in this sense. Using the constant kernel, $K_w \approx \tau$, causes higher magnitudes for the $\langle\Omega_t\Omega_t\rangle\tau_k^2$ and this magnitude shows a trend as function of Re_τ as well, where higher Re_τ results in higher $\langle\Omega_t\Omega_t\rangle\tau_k^2$. By imposing the adaptive filtering, and considering the kernel window size of $0.15\tau_k \leq K_w \leq 0.4\tau_k$, the magnitude of $\langle\Omega_t\Omega_t\rangle\tau_k^2$ reduces close to one order of magnitude. The mean value of this region (colored markers), show the magnitude in the range of $0.2 \leq \langle\Omega_t\Omega_t\rangle\tau_k^2 \leq 0.6$ where the lower magnitude refers to the first class of the curvature, $\kappa^* < 0.28$. The trend suggests that, it is possible to have even closer value to 0.1, for perfectly straight fibers at $\kappa^* \approx 0$, as shown previously in the literature for HIT experiments [66, 64, 54].

To investigate the difference between using constant, $K_w \approx 2.8\tau$, and adaptive kernel size, $0.15\tau_k \leq K_w \leq 0.4\tau_k$, on the mean square tumbling rate as function of y^+, we plot the $\langle\Omega_t^+\Omega_t^+\rangle$ for $\mathrm{Re}_\tau = 180$ in figure 5.6. Raw data referring to $K_w \approx 2.8\tau$

are shown by triangle marker and data representing $0.15\tau_k \leq K_w \leq 0.4\tau_k$ are shown by pentagram marker, all coloured by their corresponding curvature class. Fitted curves, by using smoothed spline approach, are plotted by straight and dashed lines for $K_w \approx 2.8\tau$ and $0.15\tau_k \leq K_w \leq 0.4\tau_k$, respectively. In the region close to channel center, $y^+ > 100$, both cases show $\langle \Omega_t^+ \Omega_t^+ \rangle$ in same order of magnitude and with same sensitivity to the curvature classes. By approaching the wall, deviation starts and the difference between two cases grows where in the near wall region, $y^+ < 20$. In this position of the domain, there is almost one order of magnitude difference in the $\langle \Omega_t^+ \Omega_t^+ \rangle$ due to underestimation done by the constant kernel approach for the near wall tracks. Although the magnitude is different, the trend in the near wall is similar for both cases and the magnitude of $\langle \Omega_t^+ \Omega_t^+ \rangle$ is constant within that range.
Turbulent channel flow has variable flow length scales, increasing from the near wall region towards the channel center. In order to investigate the effect of the relative length of fiber with respect to the length scale of the flow, we plot the magnitude of the $\langle \Omega_t \Omega_t \rangle \tau_k^2$ as function of relative length of fiber. We consider the magnitude of the mean square tumbling rate for all curvature classes as function of the ratio of effective length to the local Kolmogorov length scale, $L^* = L_{eff}/l_k$, in figure 5.7(a,b). In figure 5.7(a), we show the results by using the constant kernel size for filtering process, $K_w \approx 2.8\tau$, where in figure 5.7(b), same statistics are shown by using adaptive filtering approach, variable kernel window size in the range of $0.15\tau_k \leq K_w \leq 0.4\tau_k$. We would like to mention a point here: reason behind choosing $K_w \approx 2.8\tau$ as the constant kernel size relies on the visual observation of the tracks, and indeed using shorter or larger kernel, results in over or underestimation of the magnitudes. In both panels, figure 5.7(a,b), data of $\mathrm{Re}_\tau = 180$, $\mathrm{Re}_\tau = 360$ and $\mathrm{Re}_\tau = 720$ are shown by circle, square and diamond markers, while colored based on their curvature class. In figure 5.7(a), it is obvious that, trends are same for all three Re_τ, where within each Re_τ, mean square tumbling rate shows almost one order of magnitude reduction by increasing L^*. Note that, in data set of each Re_τ, smaller L^* refers to the fiber in the channel center and larger ones, corresponds to the fibers flowing closer to the wall region. Another observation is, for $\mathrm{Re}_\tau = 180$ and $\mathrm{Re}_\tau = 360$ effect of curvature is less prominent than $\mathrm{Re}_\tau = 720$. In figure 5.7(b), we can observe that by imposing the kernel window size of $0.15\tau_k \leq K_w \leq 0.4\tau_k$, magnitude of the $\langle \Omega_t \Omega_t \rangle \tau_k^2$ for each curvature class stays almost constant, no matter of the magnitude of the L^*, except for the very last data point, $L^* > 6$. This is in agreement with the observation of [64], where inertialess fibers in range $L^* < 10$ show $\langle \Omega_t \Omega_t \rangle \tau_k^2 \approx 0.1$ without a significant reduction in magnitude. The main observation of this plot, is the effect of curvature, where we can conclude that regardless of the magnitude of L^*, increasing curvature results in higher $\langle \Omega_t \Omega_t \rangle \tau_k^2$. The main reason behind the difference observe in figure 5.7(a) and figure 5.7(b), is due to underestimation of the magnitude of the mean square tumbling rate in the near wall region when data are smoothed by constant kernel size.

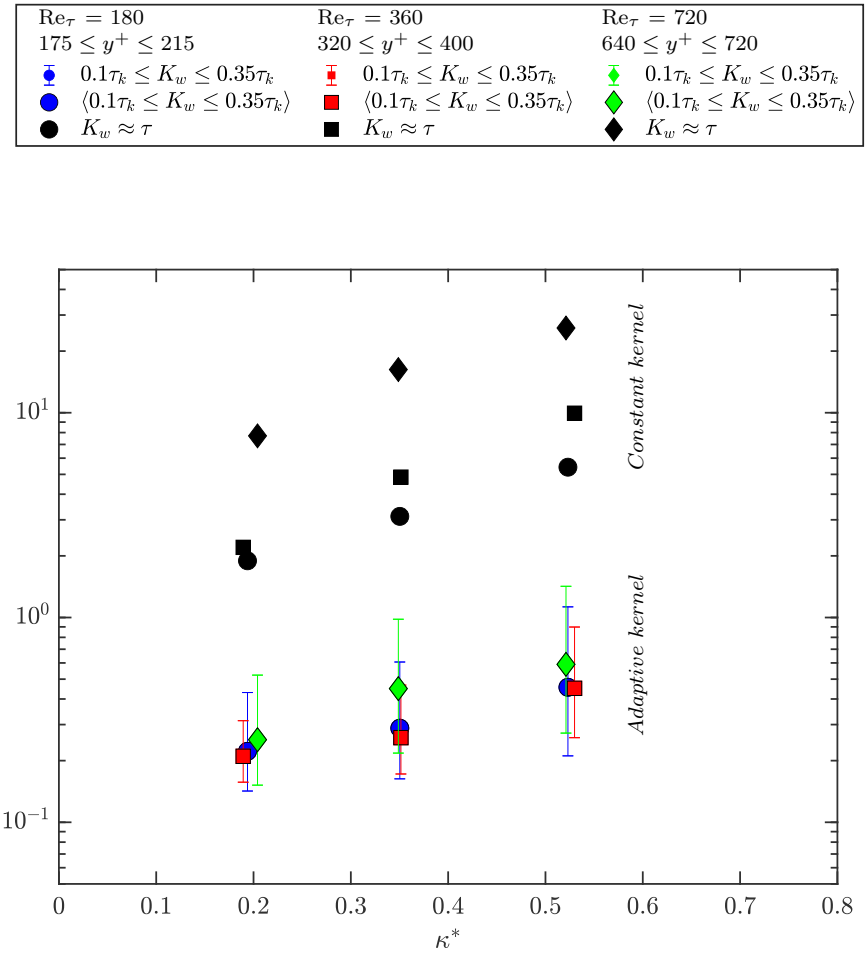

FIGURE 5.5 – Comparison of Mean square tumbling rate of fibers as function of curvature, $\kappa^* < 0.28$, $0.28 < \kappa^* < 0.42$ and $\kappa^* > 0.42$. Curvature magnitude, κ^* shown in x axis, is chosen based on the weighted average of each curvature class. Data are non-dimensionlised by the local Kolmogorov time scale, τ_k^2 , for Re$_\tau$ = 180, Re$_\tau$ = 360 and Re$_\tau$ = 720, in 175 ≤ y^+ ≤ 215, 320 ≤ y^+ ≤ 400 and 640 ≤ y^+ ≤ 760. Re$_\tau$ = 180, data of $0.15\tau_k \leq K_w \leq 0.4\tau_k$ is shown in blue error bar and the mean value of this range is shown by blue circle while the data representing constant kernel of $K_w \approx \tau$ is shown with black circle marker. In the same way, for Re$_\tau$ = 360, data are shown in red error bar, red and black squared markers while data of Re$_\tau$ = 720 are presented in green error bar, green and black diamond markers.

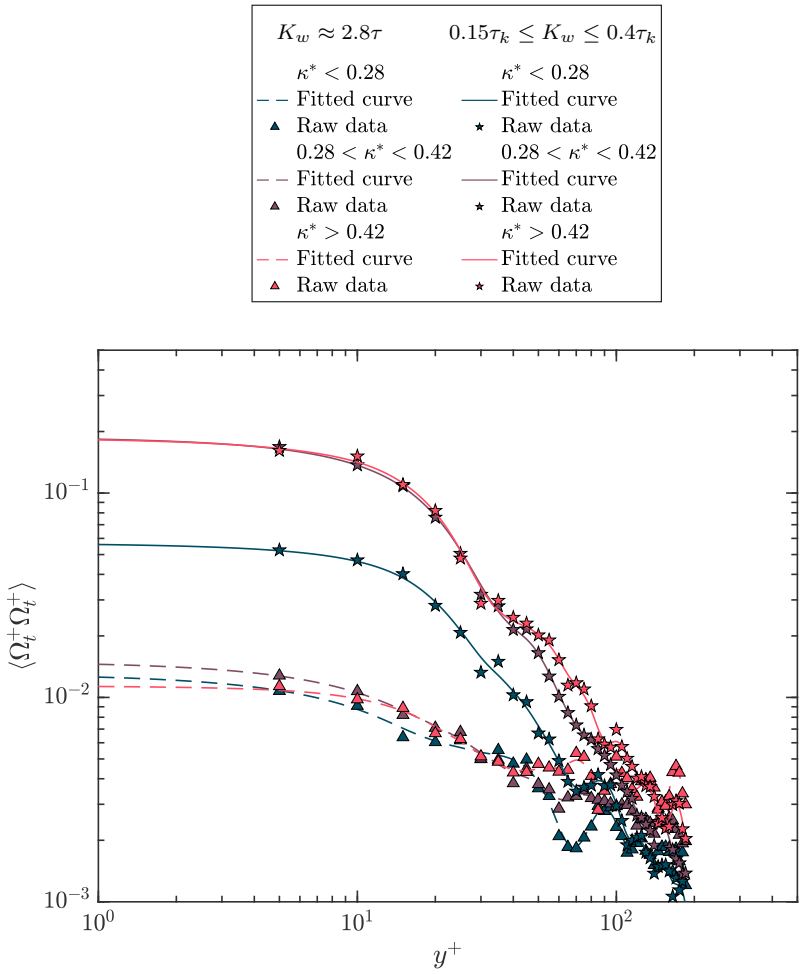

FIGURE 5.6 – Mean square tumbling rate $\langle \Omega_t^+ \Omega_t^+ \rangle$, as function of y^+ , for $\mathrm{Re}_\tau = 180$. Raw data referring to $K_w \approx 2.8\tau$ are shown by triangle marker and data representing $0.15\tau_k \leq K_w \leq 0.4\tau_k$ are shown by pentagram marker, all coloured by their corresponding curvature class. Fitted curves, by using smoothed spline approach, are plotted by solid and dashed lines for $K_w \approx 2.8\tau$ and $0.15\tau_k \leq K_w \leq 0.4\tau_k$, respectively.

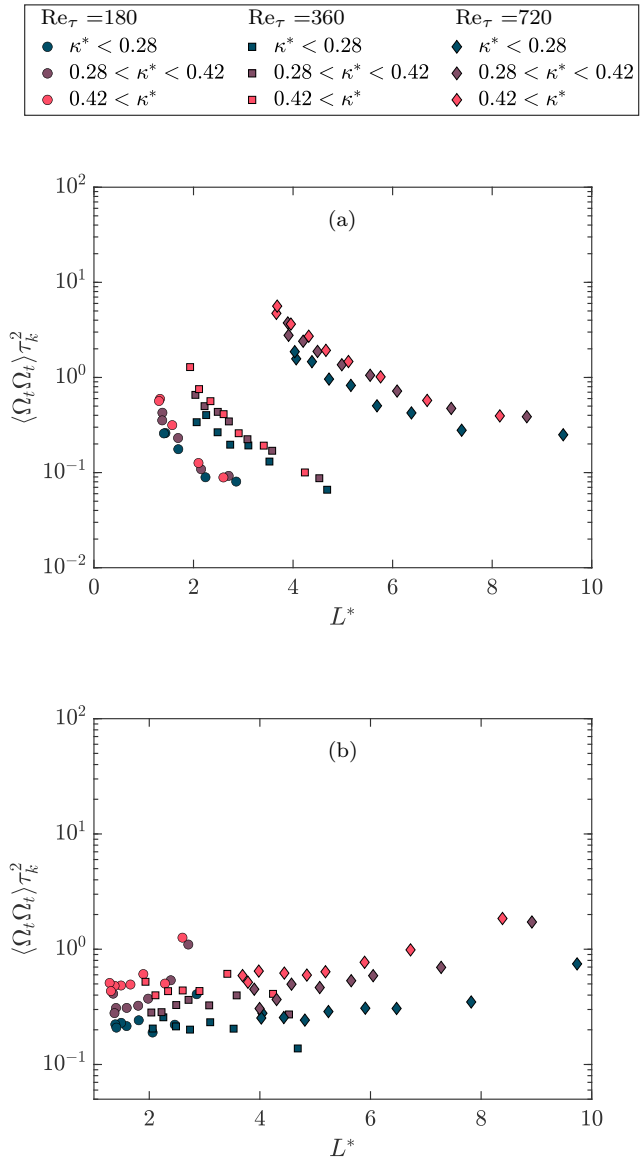

FIGURE 5.7 – Mean square tumbling rate of fibers, non-dimensionlised by local Kolmogorov time scale, $\langle \Omega_t \Omega_t \rangle \tau_k^2$, as function of the ratio of effective length to the local Kolmogorov length scale, $L^* = L_{eff}/l_k$. In panel (a), constant kernel window size, $K_w \approx 2.8\tau$ is used for obtaining these data. In panel (b), adaptive filtering by using variable kernel size (in terms of snapshot number), $0.15\tau_k \leq K_w \leq 0.4\tau_k$, is used for obtaining these data.

5.3.2 Spinning

Measurement of the spinning of straight fibers is very hard to obtain and not possible without using marks on the surface of the fibers. This is due to the existence of the infinite options for defining the two axis perpendicular to the fibres principal axis, x', shown in figure 2.8. Based on the author knowledge, the only available study for this matter, is very recently published by Oehmke et al. [62], where they use visual helix marks on the surface of the fibers by which they can measure the spinning, however, this method is only possible for large, thick fibers and is almost impossible to be implemented for the size of the fibers used in this study. Unlike perfectly straight fibers, asymmetry in shape, makes it possible to define a plane which contains the fibers, Π shown in figure 2.8, and therefore one can find the two perpendicular axis to the principal axis of the fibers. In this way, it is possible to measure the spinning, but the accuracy of the measurements depends on the rate of asymmetry, or in other words, depends on the magnitude of the curvature: larger the curvature, higher the accuracy of the spinning measurements. Mean square spinning rate of the fibers, non-dimensionlised by local Kolmogorov time scale, $\langle \Omega_s \Omega_s \rangle \tau_k^2$, as function of the ratio of effective length to the local Kolmogorov length scale, $L^* = L_{eff}/l_k$ is shown in figure 5.8(a,b). Data filtered by using constant kernel window size, $K_w \approx 2.8\tau$, for $\mathrm{Re}_\tau = 180$, $\mathrm{Re}_\tau = 360$ and $\mathrm{Re}_\tau = 720$ are shown in figure 5.8(a) by circle, squared and diamond markers while colored based on their curvature classes, respectively. Same as figure 5.7(a), there is a significant reduction in magnitude of the $\langle \Omega_s \Omega_s \rangle \tau_k^2$ for each Re_τ dataset by increasing the L^*, i.e by approaching from center to the near wall region. In addition, the trends are more sensitive to curvature compared to data reported for mean square tumbling rate in figure 5.7(a) and we observe that curved fibers show lower magnitude for mean square spinning rate compared to straighter fibers. By imposing the adaptive filtering to the tracks, $0.15\tau_k \leq K_w \leq 0.4\tau_k$, shown in figure 5.8(b), the trend changes and the significant reduction in the magnitude of the $\langle \Omega_s \Omega_s \rangle \tau_k^2$, within the same Re_τ dataset is not visible anymore. In contrast, we observe that for $L^* < 6$, $\langle \Omega_s \Omega_s \rangle \tau_k^2$ stays constant for each curvature class and curved fibers has lower magnitude compared to the straighter ones. This trend is different for $L^* > 6$, in this range, curvature does not have any effect the magnitude stays constant for all three classes. The observed trend as function of curvature, is consistence regardless of filtering approach and and the chosen kernel size.

The magnitude of the mean square spinning rate, even by imposing the adaptive filtering, is bigger than 1, suggesting faster rotation than the smallest eddies of the flow. We provide two possible explanations for this observation. We speculate that, due to larger length of the fibers with respect to the Kolmogorov flow length scale, and smaller ratio of the diameter of the fibers to the Kolmogorov length scale, coupling of multiple flow structure along fibers length could result in higher spinning for the fibers than the flow structures itself. In addition, preferential sampling of the fibers within faster structures of the flow could result in higher mean square spinning magnitude than the flow as well. This preferential sampling should be more evident in the near wall region as discussed in §4.2.2. Another reason could be the measurement accuracy for detecting the spinning magnitude. Although, adaptive filtering significantly improves the magnitude predictions for the mean square tumbling rate as shown in figure 5.5, where the trend as function of curvature suggests that it is possible to have closer

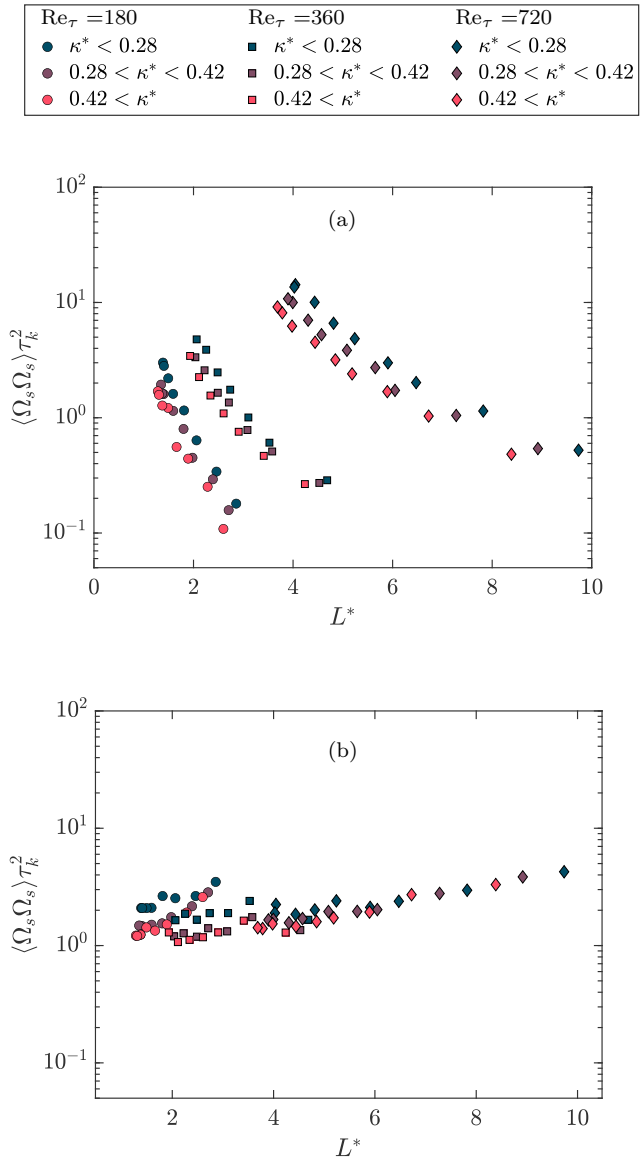

FIGURE 5.8 – Mean square spinning rate of the fibers, non-dimensionlised by local Kolmogorov time scale, $\langle \Omega_s \Omega_s \rangle \tau_k^2$, as function of the ratio of effective length to the local Kolmogorov length scale, $L^* = L_{eff}/l_k$. In panel (a), constant kernel window size, $K_w \approx 2.8\tau$ is used for obtaining these data. In panel (b), adaptive filtering by using variable kernel size (in terms of snapshot number), $0.15\tau_k \leq K_w \leq 0.4\tau_k$, is used for obtaining these data.

value to HIT predictions ($\langle\Omega_t\Omega_t\rangle\tau_k^2 \approx 0.1$ [66, 64, 54]) for perfectly straight fibers at $\kappa^* \approx 0$, sensitivity of the mean square spinning rate magnitude to the measurement accuracy could be even higher and the predicted magnitude still needs corrections by using higher temporal and spatial resolution for the recordings.
It is well known that fibers with length smaller than Kolmogorov length scale of the flow, spin more than tumble [85]. It is expected that long rods tendency to spin more than tumble reduces if the length of the fibers gets longer than Kolmogorov length scale $L > l_k$. This reduction could be due to the switch of the preferential orientation from the local vorticity to the most extensional eigenvector of the coarse-grained strain rate tensor as reported by [70]. In contrast, Picardo et al. [68], showed that long rods tend to trap in vortex tubes, elongated and randomly oriented coherent structures with typical length of integral length of the flow. Oehmke et al. [62] observed that, even in case of inertial fibers longer than Kolmogorov length scale, $10 < l_k$, fibers tend to spin more than tumble, or in other words, the ratio of the mean square spinning rate to tumbling, $\langle\Omega_s\Omega_s\rangle/\langle\Omega_t\Omega_t\rangle$, is always bigger than one. They suggested that the scenario arguing the effect of vortex tubes on the fibers spinning is in agreement with their observation and in-fact inertial fibers longer than Kolmogorov length scale preferentially trap in theses structures leading them to spin more than tumble. We plot the $\langle\Omega_s\Omega_s\rangle/\langle\Omega_t\Omega_t\rangle$ by using variable kernel window size, $0.15\tau_k \leq K_w \leq 0.4\tau_k$, as function of the ratio of effective length to the local Kolmogorov length scale, $L^* = L_{eff}/l_k$, in figure 5.9. We can observe that, regardless of the magnitude of L^*, i.e. independent of Re_τ, for each curvature class, the magnitude of the $\langle\Omega_s\Omega_s\rangle/\langle\Omega_t\Omega_t\rangle$ stays constant and it is always bigger than one. In other words, non-axysmmetric fibers used in this study, regardless of their asymmetry rate and L^*, tend to spin more than tumble. This observation, $\langle\Omega_s\Omega_s\rangle/\langle\Omega_t\Omega_t\rangle > 1$, is agreement with experiments done by Oehmke et al. [62]. Our data show that, tendency of fibers to spin more than tumble decreases by increasing the curvature or rate of the asymmetry of the fibers. Curved fibers show $\langle\Omega_s\Omega_s\rangle/\langle\Omega_t\Omega_t\rangle \approx 2.6$ while it is $\langle\Omega_s\Omega_s\rangle/\langle\Omega_t\Omega_t\rangle \approx 4.5$ for $0.28 < \kappa^* < 0.42$ and $\langle\Omega_s\Omega_s\rangle/\langle\Omega_t\Omega_t\rangle \approx 10$ for $\kappa^* < 0.28$. If the scenario provided by Oehmke et al. [62] and Pujara et al. [70] regarding preferentially trapping of fibers in vortex tubes is the main reason behind the fibers tendency to spin more than tumble, we speculate that, curved fibers should have less tendency to preferentially trapped in the vortex tubes due to their curvature induced thickness which could be thicker than these elongated coherent structures thickness. In addition, regardless of this suggested scenario, it is reasonable to assume that, curved fibers due to the asymmetry induce by the curvature, have higher inertia around their principal axis compared to the straighter ones, and therefore they spin with lower rate around their principal axis compared to straighter ones. Although the measurement accuracy of the mean square spinning rate for the fibers of the first curvature class could be lower than the curved ones, due to lower asymmetry rate and possible error in the detection fiber orientation, the observed trend as function of curvature seems to be consistent.

5.4 Conclusion

In this chapter, we introduced the adaptive filtering method and evaluate its effect compared to case of constant kernel by referring to the the mean square tumbling and

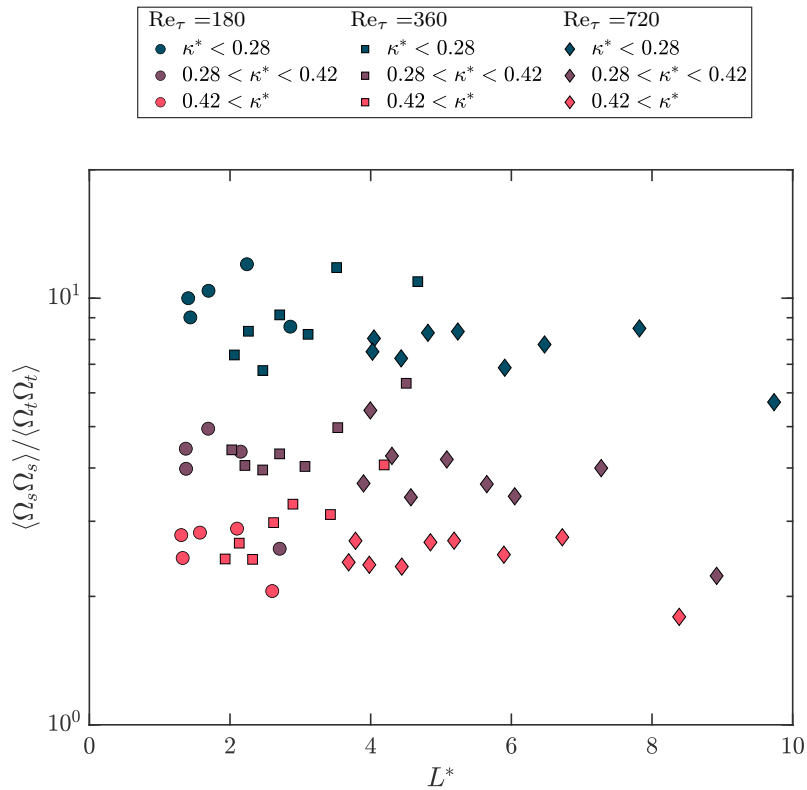

FIGURE 5.9 – Ratio of Mean square spinning rate to Mean square tumbling rate of the fibers, $\langle \Omega_s \Omega_s \rangle / \langle \Omega_t \Omega_t \rangle$, as function of as function of the ratio of effective length to the local Kolmogorov length scale, $L^* = L_{eff}/l_k$. Variable kernel window size, $0.15\tau_k \leq K_w \leq 0.4\tau_k$ is used for obtaining these data.

spinning rate statistics. Based on this comparison, adaptive filtering shows significant influence on the results and it seems that using the constant kernel underestimates the magnitude of the near wall Mean square tumbling spinning rate. Referring to the Mean square tumbling rate data in channel center, filtered by variable kernel size $0.15\tau_k \leq K_w \leq 0.4\tau_k$, we obtain $0.2 \leq \langle\Omega_t\Omega_t\rangle\tau_k^2 \leq 0.6$ where the lower magnitude refers to the first class of the curvature, $\kappa^* < 0.28$. The trend shown in figure 5.5 suggests that, it is possible to have even closer value to 0.1, for perfectly straight fibers at $\kappa^* \approx 0$, as shown previously in the literature for HIT experiments [66, 64, 54]. Mean square tumbling rate and spining of the fibers processed by adaptive filtering, $\langle\Omega_t\Omega_t\rangle\tau_k^2$ and $\langle\Omega_s\Omega_s\rangle\tau_k^2$, shows constant magnitude for each curvature class as function of the ratio of effective length to the local Kolmogorov length scale, $L^* = L_{eff}/l_k$, no matter of the magnitude of the L^*, except for the very last data point, $L^* > 6$. Finally, we observed that, non-axysmmetric fibers used in this study, regardless of their asymmetry rate and L^*, tend to spin more than tumble, $\langle\Omega_s\Omega_s\rangle/\langle\Omega_t\Omega_t\rangle > 1$ and magnitude of this ratio decreases by increasing the asymmetry in shape.

6

Effect of near-wall structures

In this chapter, we provide a qualitative visualisation of the fibers, classified based on their curvature class. In particular, we focus on the near-wall region and we investigate a larger domain in the span-wise direction at Re_τ=180. In this way, we are able to investigate the possible influence of near-wall coherent structures such as turbulent streaks on the orientation and concentration of the fibers.

6.1 Experimental setup

By means of these experiments, we aim at investigating the effect of near wall coherent structures on the orientation and rotation of the fibers, therefore the illumination volume must cover more space in the span-wise direction. To this end, we will reorganise the illumination volume, as discussed in §2.1.3 with dimension of $53.4 \times 53.4 \times 14$ mm^3 to $84 \times 14 \times 84$ mm^3, $x \times y \times z$. Illumination comes from the side of the channel and consists of a thick laser sheet (527 nm, double cavity, 25 mJ per pulse, Litron LD60-532 PIV). The images are recorded using four Phantom VEO 340 L cameras, with sensor size of 2560×1600 pixel at 0.8 kHz and each pixel size is 10×10 μm^2. The cameras are located on top of the channel. Flow and recording properties are given in table 6.1. Real view of the test section is presented in figure 6.1.

Re_τ	180
Illumination volume (x, y, z)	$14 \times 72 \times 52$ mm^3
CCD sensor size (cropped)	2560×1600 pixel
Digital resolution	0.038 mm/pixel
$f/\#$	22
Depth of field	31 mm
Frame rate of fiber-laden recording	0.8 kHz
Frame rate of unladen recording, STB	1 kHz

TABLE 6.1 – Summary of the flow and recording parameters adopted.

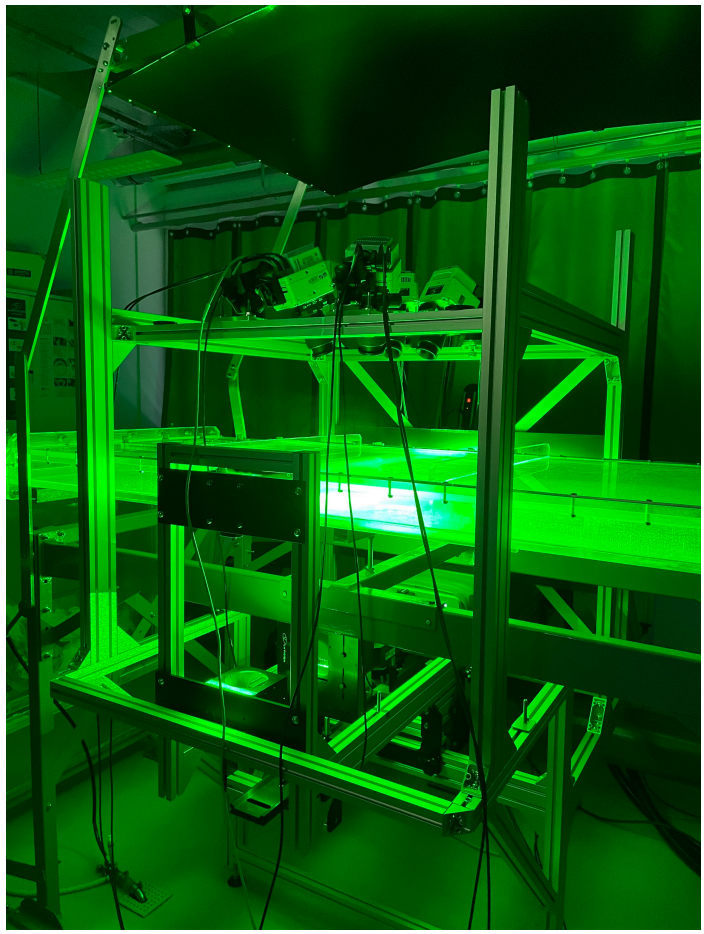

FIGURE 6.1 – Real view of the test section consist of 4 cameras located at top and laser beam illuminated from the side wall bu means of two perpendicular mirror placed on one side of the channel.

6.2 Unladen flow

It is more than five decades that near wall coherent structures and in particular streak like structures have been observed experimentally, first time reported by Kline et al. [43] . These structures could have significant effect on the local concentration and orientation of the particles in the near wall region. We performed single phase experiments at $Re_\tau = 180$, and present the averaged stream-wise velocity results for the domain corresponding to $300 \times 50 \times 300$ wall units in x, y and z direction, respectively. The contours of wall-normal averaged stream-wise velocity of the flow in $15 < y^+ < 20$, normalised by the maximum velocity of the flow in the specified margin of y^+, are shown for $t = 0$, $t = 30\tau$, $t = 60\tau$ and $t = 90\tau$ of a continues recording in figure 6.2(a-d), respectively. Each panel of figure 6.2 corresponds to the time averaged data interval equal to $t = \tau$ of the recording. It is clear form this qualitative comparison that within the domain considered, evidences of existences of the high and low speed streaks are visible. Although the location of these structures varies in time, but the number of them is consistent within the domain of interest. Performing simultaneous flow and fiber tracking is not possible due to experimental difficulties. In the next section, we anticipate the location of these structure by referring to the fibers wall-normal averaged stream-wise velocity, in the margin of $0 < y^+ < 40$, but this observation in figure 6.2, gives us a hint about the existence and frequency of these structure in the near wall to be used in the next section and results related to fibers concentration and orientation.

6.3 Results

In this section, we present the results of our dataset which consists of about 10^4 fibers, each tracked over at least 50 consecutive frames at $Re_\tau = 180$. This corresponds to a minimum time window of 1.4τ. We report a qualitative representation of the distribution, orientation and velocity of the non-axisymmetric fibers. In figure 6.3 (a), we show the three dimensional distribution and in figure 6.3 (b) the $z - y$ projection of the fibers, colored based on their stream-wise velocity normalised by the maximum velocity of the flow in the specified margin of domain height, $0 < y^+ < 60$. Unlike the unladen experiments, here we had restriction in the amount of data, therefore fibers are shown for a time window of 90τ. From each track time length, instants of $t_{track} = 0$ and $t_{track} = 1.4\tau$ are chosen and shown in this figure. Fibers are visually shown regardless of their curvature class, $0 < \kappa^* < 1$. In figure 6.3 (a), contour of the wall-normal averaged stream-wise velocity of the fibers is shown on bottom of the three dimensional representation of the fibers. By referring to the figure 6.3 (b), we can qualitatively observe the near wall structures effect on the stream-wise velocity of the fibers, where there are two high speed cores in the vicinity of $0 < z^+ < 30$ and $150 < z^+ < 200$. Since the fibers ensemble time, i.e the time window of recording that we consider for plotting the fibers and measuring the averaged velocity, is large, the difference between the streaks is small but still visually visible.

We present the qualitative representation, $z - x$ projection, of the fibers position in the domain in figure 6.4. From each track time length, instances of $t_{track} = 0$

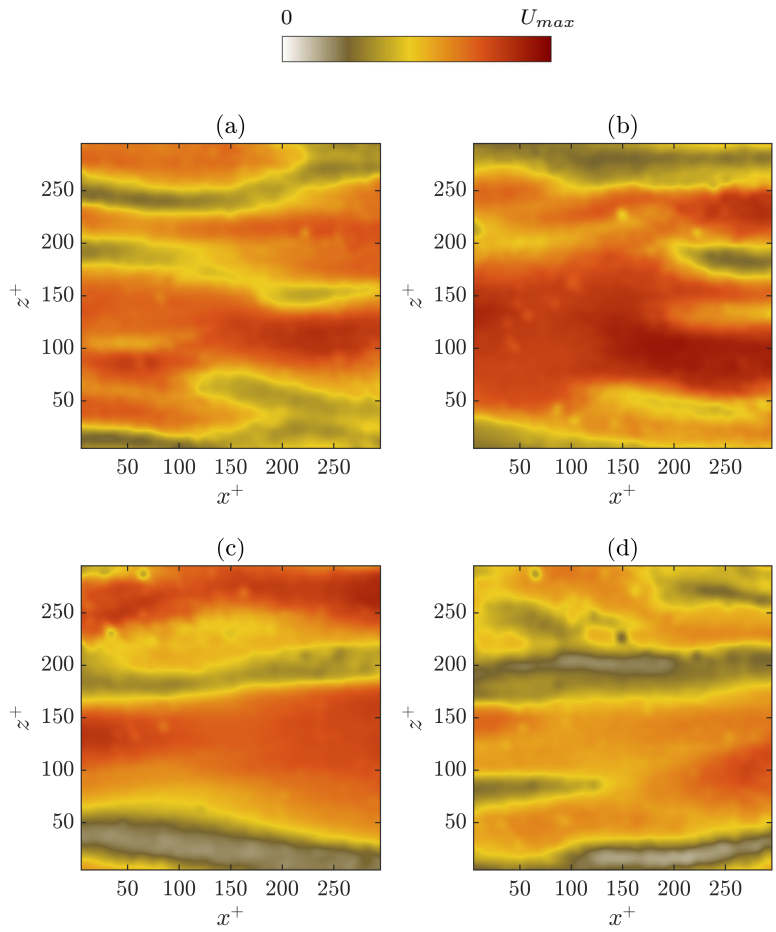

FIGURE 6.2 – Averaged stream-wise velocity of the flow in $15 < y^+ < 20$ are shown for $t = 0$, $t = 30\tau$, $t = 60\tau$ and $t = 90\tau$ of a continues recording, in panels (a), (b), (c) and (d), respectively. Each panel of figure 6.2 corresponds to the average ensemble of $t = \tau$ of the recording.

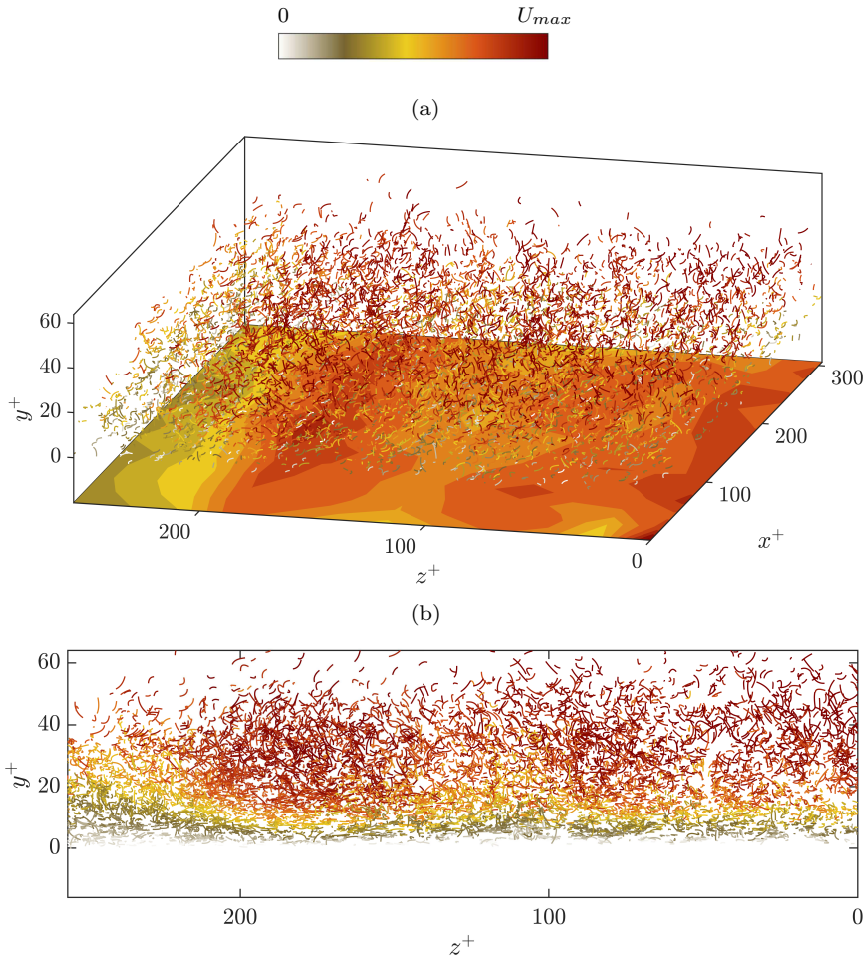

FIGURE 6.3 – Three dimensional, in panel (a) and $z-y$ projection, in panel (b), of the fibers, colored based on their stream-wise velocity normalised by the maximum velocity of the flow in the specified margin of domain height, $0 < y^+ < 60$.

and $t_{track} = 1.4\tau$ of each track are chosen and shown in the figure 6.4 (a) and (b) for straight fibers, $\kappa^* < 0.28$ and curved ones, $\kappa^* > 0.42$, respectively. Figure 6.4 (a), contains instants of $t_{track} = 0$ and $t_{track} = 1.4\tau$ of 4×10^3 tracks of straighter fibers, oversampled on the contour of wall normal averaged stream-wise velocity of the fibers. Although to give more quantitative analysis, longer recordings and larger database is needed, qualitative view of this figure shows a tendency of the fibers to accumulate in high speed streaks. Figure 6.4(b) contains instances of $t_{track} = 0$ and $t_{track} = 1.4\tau$ of 3.6×10^3 tracks curved fibers oversampled on the contour of wall normal averaged stream-wise velocity of the fibers. These qualitative observations show weaker tendency of the curved fibers to stuck in high speed streaks compared to the straighter fibers and distribution seems to be more scattered.
Non-axisymmetric fibers used in this study can be described on a 2D plane. The preferential orientation of the plane angle with wall normal axis of lab reference frame, γ, is independent of the orientation of their principal axis with respect to the wall normal axis of lab reference frame, ϑ_y. The preferential orientation of the plane angle with wall normal axis of lab reference frame, γ, is shown in figure 4.8(a). In figure 4.8, we showed that, curved fibers, tend to flow parallel to the wall surface, while their plane angle ranges $\pi/3 < \gamma < \pi/2$. This observation have similarities with previously reported near wall orientation of the inertial disk by Challabotla et al. [20] and Voth [86]. In figure 6.5 (a), we plot the $z - x$ projection of the instants $t_{track} = 0$ and $t_{track} = 1.4\tau$ of each track for curved fibers, $\kappa^* > 0.42$, oversampled on the contour of wall normal averaged stream-wise velocity of the fibers and colored based on their preferential orientation of the plane angle with wall normal axis of lab reference frame, γ. Similar to what is reported in figure 4.8, in figure 6.5 (a), we observe that most of the curved fibers show a color representing the $\gamma > \pi/4$, suggesting similarities with previously reported near wall orientation of the inertial disk. In figure 6.5 (b), $z - y$ projection of the volume of interest is shown. It is clear that, most of the fibers with $\gamma \approx 0$ are located in the region of $y^+ < 5$ and very close to the wall, while $\gamma > \pi/4$ is widely spread within the height of the domain of investigation. Although, in general there is a similarity between curved fibers near wall orientation and the near wall inertial disk orientation in the $y^+ < 40$, in the very close wall region $y^+ < 5$, there exists differences. In order to give clear discussion on this matter, larger dataset is needed and will be done as future work of this study.

6.4 Conclusion

In this chapter we investigate, visually, the effect of near wall coherent structures of fibers distribution and orientation. We qualitatively observed the near wall structures effect on the stream-wise velocity of the fibers. In the near wall region, there exist two high and low speed cores for the sample of fibers shown in figure 6.3. Straighter fibers, $\kappa^* < 0.28$ showed weak preferential distribution in high speed streak, while curved ones, $\kappa^* > 0.42$, showed more scatter distribution for the data shown here. Visualisation of the curved fibers coloured based on the orientation of their plane angle with respect to the wall normal axis of lab reference frame, γ, is in agreement with the discussion done in §4.2.3 and figure 4.8. Although the results shown in this chapter gives qualitative views about the fibers distribution and orientation in the

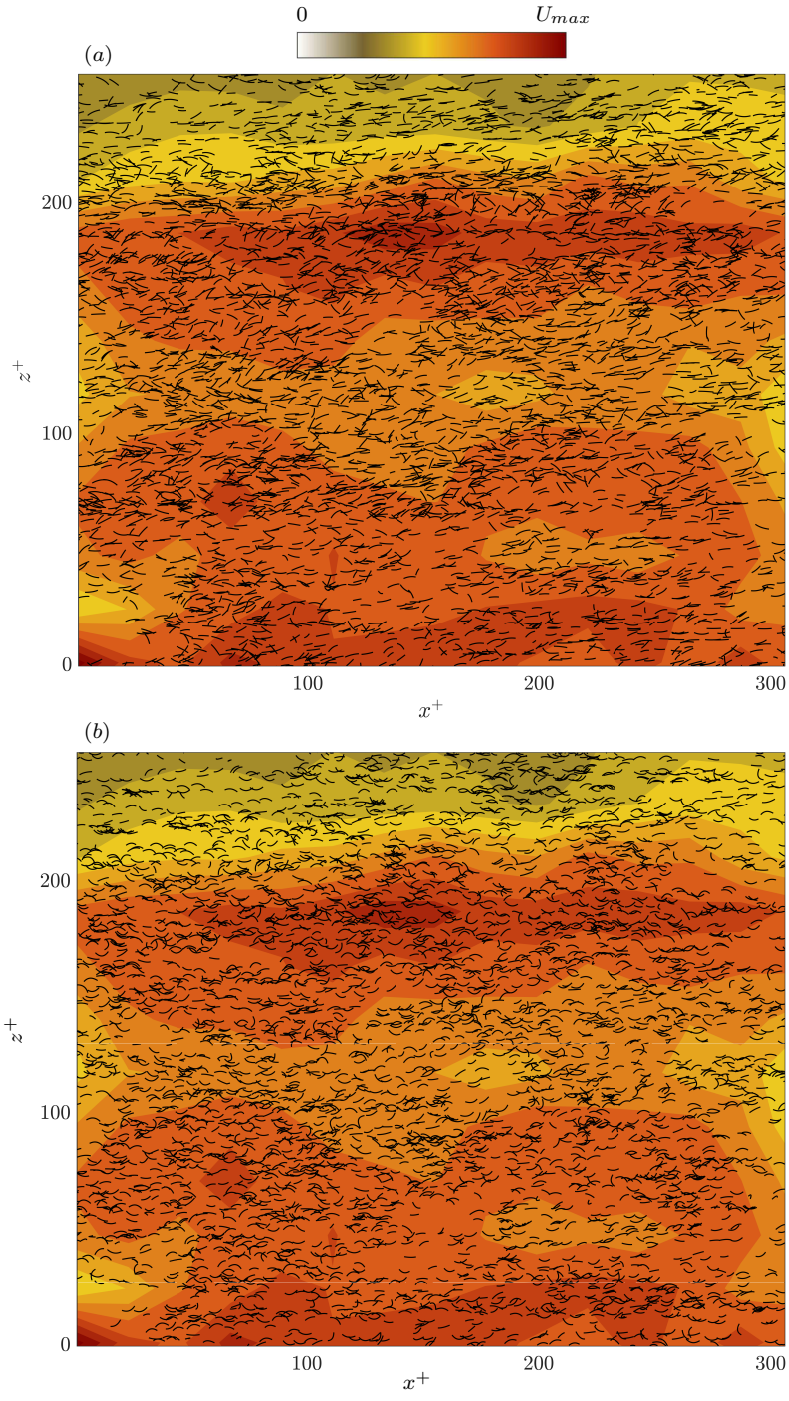

FIGURE 6.4 – Distribution of straighter fibers, $\kappa^* < 0.28$, and curved ones, $\kappa^* > 0.42$, corresponding to instants of $t = 0$ and $t = 1.4\tau$ of each track, oversampled on the contour of wall normal averaged stream-wise velocity of the fibers are shown in panel (a) and (b), repsectively.

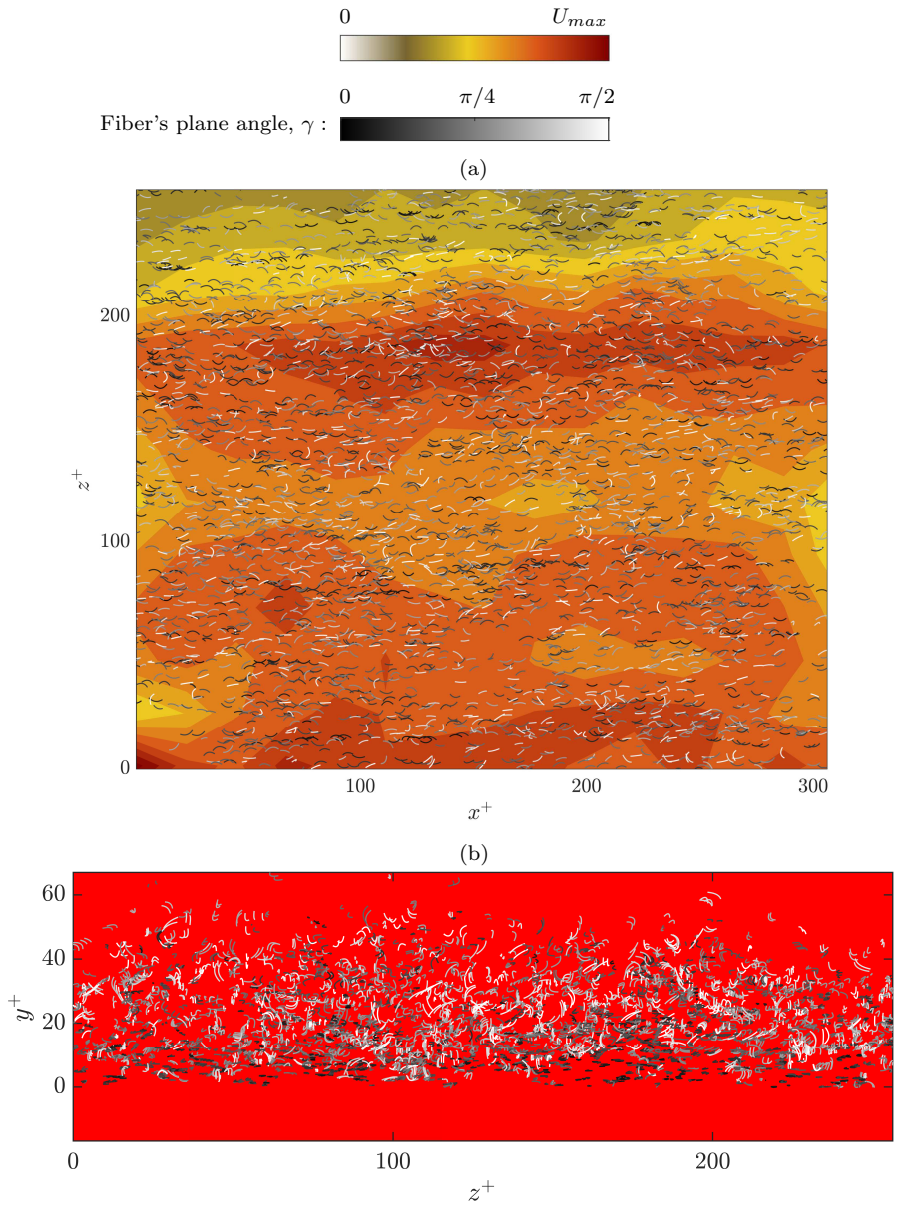

FIGURE 6.5 – Panel (a) refers to the $z-x$ projection of the instants $t = 0$ and $t = 1.4\tau$ of each track for curved fibers, $\kappa^* > 0.42$, oversampled on the contour of wall normal averaged stream-wise velocity of the fibers and colored based on preferential orientation of the plane angle with wall normal axis of lab reference frame, γ. Panel (b) refers to $z - y$ projection of the volume of the interest.

near wall and effect of the wall streaks on them, to provide more in detail statistics larger dataset is needed which will be done as the future work of this study.

7

Conclusions and future works

7.1 Conclusions

In most of the environmental and industrial applications, fibers have asymmetry in their shape or mass distribution. We investigated experimentally the behaviour of long non-axisymmetric fibers in turbulent channel flow. To this aim, we introduced a novel experimental methodology for detecting the asymmetry of the fibers and track them in time and volume of interest. This methodology is based on reconstructing fibers light distribution in 3D by means of MART and fitting a polynomial passing through the clusters of voxels. In this way, we can detect the curvature of the polynomial and therefore classify the statistics based on fibers curvature. We provided, original experimental measurements of disturbution, orientation and rotation rates of long curved fibers by performing experiments in different Reynolds numbers, $\mathrm{Re}_\tau = 180$, $\mathrm{Re}_\tau = 360$ and $\mathrm{Re}_\tau = 720$. Our measurements showed that effect of the non-axisymmetric shape of the fibers produces important differences in the fiber behaviour with respect to straight rods, in terms of concentration, orientation and rotation rates.

Distribution of the fibers is influenced by the asymmetry rate of the fibers as well as the Reynolds number of the experiments. We observed that, no matter of the Reynolds number or asymmetry rate, from channel center to the close wall region, averaged normalised concentration of the fibers stays constants. Discrepancy grows in the near wall region and the concentration shows different trends depending on the curvature of the fibers: curved fibers ($\kappa^* \geq 0.42$) show higher concentration compared to the straighter ones ($\kappa^* \leq 0.28$). We speculate the reason behind this observation to the difference in interaction that fibers have with near wall coherent structure and channel wall due to their shapes asymmetry rate, in other words, geometry of the fibers play critical role on this matter. To investigate this, we showed that preferential orientation of the principal axis of the curved fibers ($\kappa^* \geq 0.42$) and the straighter ones ($\kappa^* \leq 0.28$) in $y^+ < 10$ is different due to their different interaction with near wall structures, and this influence their local concentration.

The only deviation that we observed for the average stream-wise velocity of fibers with respect to the unladen flow profile, happens in the near wall region and is consistent for all Reynolds numbers reported. Fibers show higher average velocity in the near wall region, due to their possible higher residence time in the high speed coherent structures in the near wall region. We speculate that, same as average normalised concentration,

geometry of the fibers plays a critical role on this matter. PDF data of the stream-wise velocity showed that curved fibers ($\kappa^* \geq 0.42$) have much higher probability than the straighter ones ($\kappa^* \leq 0.28$). Therefore, curved fibers are expected to move slowly in this region compared to the straighter ones and their residence time will increase with respect to the straight ones, eventually increase their local concentration.

Preferential orientation of non-axisymmetric fibers showed significant dependency on the shape and asymmetry rate of the fibers. In the channel center, angle created by the principal axis of the fibers with respect to the stream-wise, span-wise and wall normal axis of the laboratory reference frame, ϑ_x, ϑ_z and ϑ_y, are randomly distributed. This behaviour shares similarities with Homogeneous Isotropic Turbulence conditions. The story looked significantly different in the near wall region. In the near wall region, although the fibers principal axis is consistently parallel to the wall, double peak trends for the PDF of the ϑ_x, ϑ_z is observed. The observed trends are visible for all Reynolds numbers reported in this study. We showed that this double peak behaviour could be due to the different preferential orientation that fibers have while they are carried by descending and ascending motions of the flow in the near wall region, such as sweep and ejection. Non-axisymmetric fibers used in this study can be described on a 2D plane. The preferential orientation of the plane angle with the wall normal axis of lab reference frame, γ, is independent of the orientation of their principal axis wall normal axis of lab reference frame, ϑ_y. We observed that, curved fibers, tend to flow parallel to the wall surface, while their plane angle ranges $\pi/3 < \gamma < \pi/2$. This observation have similarities with previously reported near wall orientation of the inertial disks.

In order to compare our results with the numerical solutions, we solved numerically the autonomous system of ordinary differential equations for the Euler angles of curved ellipsoids in laminar shear flow [35]. We consider the same range of curvature (κ^*) studied in our experiments, and measure the mean square tumbling rate of the curved ellipsoid by using different initial conditions for the Euler angles $(\vartheta_0, n\pi, \psi_0)$, with $\vartheta_0, \psi_0 \in [0; \pi]$. We found that the normalised mean square tumbling rate of the fibers is in excellent agreement with the theoretical predictions, and also in this case the curvature plays a key role, modulating the intensity of the tumbling rate measured.

Mean square tumbling rate, $\langle \Omega_t^+ \Omega_t^+ \rangle$, statistics of the fibers non-dimensionalised by viscous time scale of the flow as function of y^+, showed that regardless of the Reynolds number, $\langle \Omega_t^+ \Omega_t^+ \rangle$ increases by approaching the wall and there is a consistent trend function curvature: curved fibers ($\kappa^* \geq 0.42$) tumble with higher magnitude than straighter wall ($\kappa^* \leq 0.28$). We also observed that, in the vicinity of the wall, magnitude of the $\langle \Omega_t^+ \Omega_t^+ \rangle$ stays constant, regardless of the Reynolds or curvature class of the fibers. These statistics were provided by using constant kernel size for the noise removal process. We observed that different values of kernel size can give tumbling rates that are different in magnitude, but the qualitative behaviour of the tumbling is not affected.

To investigate the effect of the size of the kernel to the flow time scale on the statistics, we introduced the adaptive filtering method and evaluate its effect compared to the case of constant kernel by referring to the the mean square tumbling and spinning rate statistics. In adaptive filtering, kernel size of tracks is defined in relation to the local Kolmogorov timescale of the flow at the position of the track. Based on this

comparison, adaptive filtering shows significant influence on the results and it seems using the constant kernel underestimates the magnitude of the statistics of rotational dynamics in the near wall region. By implementing adaptive filtering method, we measure $0.2 \leq \langle \Omega_t \Omega_t \rangle \tau_k^2 \leq 0.6$ in channel center where the lower magnitude refers to the first class of the curvature, $\kappa^* < 0.28$. The trend suggests that for perfectly straight fibers, reported $\langle \Omega_t \Omega_t \rangle \tau_k^2 \approx 0.1$ of HIT experiments, [66, 64, 54], could be achieved. Due to asymmetry in shape of the fibers, we are able to measure the spinning of the particles in this study as well. We shoed that, mean square tumbling and spinning rate of the fibers, non-dimensionlised by local Kolmogorov time scale and processed by adaptive filtering, independent of the magnitude of the ratio of effective length to the local Kolmogorov length scale, $L^* = L_{eff}/l_k$, stays constant for $L^* < 6$. In addition, we observed that regardless of their asymmetry rate and L^*, fibers tend to spin more than tumble, $\langle \Omega_s \Omega_s \rangle / \langle \Omega_t \Omega_t \rangle > 1$ and magnitude of this ratio decreases by increasing the asymmetry in shape.

7.2 Application

This original database, in which fibers are classified according to their curvature, represents a first step towards the characterisation of the behaviour of complex objects in turbulent channel flows. Our databased showed that asymmetry has significant effect on concentration, orientation and rotational dynamics of the fibers especially in the near wall boundary. The results obtained can contribute to the development and validation of new modelling approaches, which are required to tackle the variety of environmental and industrial problems in which complex particle geometries are present. Two of the most related applications are related to predictions of dynamics of the microplastics fibers in oceans and paper and pulp making processes.

Based on the available dataset of these microplastic fibers, [71], the size and shape of the fibers that we used in this study shares great similarities with real micro fibers laden in oceans. Currently, majority of the large scale ocean simulations consider the micro plastics as passive scalar [58] or in case of lagrangian tracking as a spherical tracers [84, 63, 81]. Fully resolving the shape is avoided due to tremendous computational costs in such a large scale. Predictions of these simulations could be strengthened by implementing models to impose the effect that shape of fibers have on the fibers preferential orientation and rotation rate, these additions will eventually improve the predictions that we have for concentration or hot zones of the micro fiber on and in the ocean. This impact is even more significant at smaller scales of environmental flows like rivers and small lakes. For this purpose, the comparison of numerical simulations and results of our experimental work in terms of rotational dynamics especially in the near wall region, will provide great opportunity to introduce models to be used in large scale based simulations.

Industrial applications like composite, paper and pulp making have processes which include water films transporting micro fibers. Simulations of such processes are based on multiple simplifications and includes models as well. These models could dramatically change the predictions about how these particles are layered on each other and eventually affect the final quality of the product. Indeed, the outcome of this study, in

terms of fibers preferential orientation close to wall region, could improve these models and eventually quality of their products.
Moreover, in both of the above mentioned applications, asymmetry in shape is very common for the fibers. Therefore effect of curvature in terms of preferential orientation and rotation as discussed in this dissertation could improve the currently existing models as well.

7.3 Future works

There are various topics of interest that could be tackled in future based on methodology and results of this study. The methodology proposed in this thesis has flexibility to be implemented in different flow boundary conditions and fiber properties. List of the possible future works are follows:

- **Simultaneous Fiber and Flow velocimetry:** it is important to resolve the flow around the fibers to understand the main reason induced by the shape asymmetry on the rotational dynamics. To do so, preferably in a more volume controlled configuration like HIT, series of experiments with 3D printed fibers, from perfectly straight toward a complete ring could be done. In this way, we can clearly observe the transition happens in the rotation rate such as spinning and tumbling due to the geometrical asymmetry. In order to resolve the flow around the particles and track particles simultaneously, in addition to mounting extra pair of cameras, fluorescent dyed fibers and tracers with different solutions must be used and each set of cameras should be mounted with appropriate optical filter corresponding to the fluorescent dye used for the particles.

- **Flexible fibers:** to reconstruct the flexible fibers in similar length scale of the fibers reported in this study, methodology introduced in this study should be modified. The main modification have to be done on the fitting approach. We propose to divide the cluster of voxels of the reconstructed fiber to equal and small portions and then fit a linear line to each segment. Eventually by connecting these line, one can find a spline description for the fiber. The rate of change of the spline deformation between two consecutive image must be restricted based on the flexibility limit anticipated from the fiber properties.

- **Free surface boundary condition:** Interaction of straight fibers with non breaking waves has been studied numerically and experimentally (2D planar configuration) very recently [25, 24], where it is shown that free surface boundary condition has significant effect on the orientation and local concentration of the straight fibers where the impact of this effect relies on wave amplitude as well. It would be interesting to reconstruct simultaneously the free surface and track the fibers in that region by using non-axisymmetric fibers. Methodology that is proposed here for reconstructing the fibers, is flexible to be used in this boundary condition as well. To reconstruct the free surface, we propose to use fluorescent dyed tracers and track them by means of 3D-PTV method. Fibers and tracers, should be dyed with different fluorescent solutions to enable the simultaneous tracking. The setup will need extra camera pair, and divided to two sets of

camera for surface and fiber reconstruction. Each set of cameras should be mounted with appropriate optical filter corresponding to the fluorescent dye used for the particles.

A

Publication List

A.1 Journals

A.1.1 Published

J1 **Alipour, M.**, De Paoli M., Ghaemi S. and Soldati A. (2021), Long non-axisymmetric fibers in turbulent channel flow, *Journal of Fluid Mechanics* , **916**, A3. https://doi.org/10.1017/jfm.2021.185.

J2 Jietuo Wang, **Alipour, M.**, Soligo, G., Roccon, A., De Paoli, M., Picano, F., Soldati, A. (2021), Short-range exposure to airborne virus transmission and current guidelines, Proceedings of the National Academy of Sciences (PNAS) (In press).

J3 **Alipour, M.**, De Paoli M. and Soldati A. (2020), Concentration-based Velocity Reconstruction of convective flows in Hele-Shaw cell, *Experiments in Fluids*, **61**, 9. https://doi.org/10.1007/s00348-020-03016-3.

J4 De Paoli M., **Alipour, M.** and Soldati A. (2020), How non-Darcy effects influence scaling laws in Hele-Shaw convection experiments, *Journal of Fluid Mechanics*, **892**, A41. https://doi.org/10.1017/jfm.2020.229.

J5 **Alipour, M.** and Dursunkaya Z. (2019), Limitations of Matching Condensing Film Profile on a Micro Fin with the Groove: Critical Effect of Disjoining Pressure, *Nanoscale and Microscale Thermophysical Engineering*, **vol23**, 4. https://doi.org/10.1080/15567265.2019.1633712.

J6 **Alipour, M.** and De Paoli, M. (2019), Convective dissolution in porous media: experimental investigation in Hele-Shaw cell. *Proc. Appl. Math. Mech.*, **19: e201900236**, https://doi.org/10.1002/pamm.201900236.

A.1.2 Submitted / in preparation

J7 **Alipour, M.**, De Paoli M. and Soldati A., Influence of Reynolds number on the dynamics of long non-axisymmetric fibres in channel flow turbulence, *Submitted to Journal of Fluid Mechanics*

J8 **Alipour, M.**, De Paoli M. and Soldati A., Spinning and tumbling of inertialess non-axisymmetric fibers in channel flow, *In preparation*

J9 **Alipour, M.**, Giurgiu V., De Paoli M. and Soldati A., Near wall orientation of non-axisymmetric fibers in turbulent channel flow, *In preparation*

A.2 Conferences

C1 **Alipour M.**, De Paoli M. and Soldati A., Transport of non-axisymmetric fibers in Turbulent channel flow, *EUROMECH Colloquium 621: Transport and fluxes in dispersed turbulent flows.*, 30 June 2021-2 July 2021, Online.

C2 **Alipour M.**, De Paoli M., Ghaemi S. and Soldati A., Dynamics of straight and curvy long fibers in turbulent channel flow, *Bulletin of the American Physical Society (73 APS-DFD)*, 23-26 Nov 2020, Chicago, USA.

C3 **Alipour M.**, De Paoli, M. and Soldati, A. Simultaneous measurement of velocity and concentration fields in Hele-Shaw cell, *Bulletin of the American Physical Society (72 APS-DFD)*, 23-26 Nov 2019, Seattle, USA.

C4 **Alipour M.**, De Paoli, M. and Soldati, A. Simultaneous measurement of velocity and concentration fields in Hele-Shaw cell, *ISPIV2019*, 22-24 July 2019, Munich, Germany.

C5 De Paoli, M., **Alipour M.**and Soldati, Experimental investigation on the scaling of convective dissolution in porous media, *Bulletin of the American Physical Society (72 APS-DFD)*, 23-26 Nov 2019, Seattle, USA.

C6 De Paoli, M., **Alipour M.**, Zonta, F. and Soldati, A. Experimental and numerical investigation of convective dissolution in two-dimensional porous media, *Bulletin of the American Physical Society (71 APS-DFD)*, 18-20 November 2018, Atlanta, USA.

C7 De Paoli, M., **Alipour M.**, Zonta, F. and Soldati, A. Convective dissolution in porous media: experimental investigation in Hele-Shaw cell, *90th Annual Meeting of the International Association of Applied Mathematics and Mechanics GAMM*, 18-22 Feburary 2019, Vienna, Austria.

C8 **Alipour M.**,, Dursunkaya, Z., Condensation modeling on the fin top of a micro-grooved heat pipe, *26th Canadian Congress of Applied Mechanics (CANCAM 2017)*, 28 may- 1 June 2017, Victoria, Canada.

C9 **Alipour M.**,, Dursunkaya, Z., Analyzing the Effect of Disjoining Pressure on the Condensation Film inside a Flat Groove. *19th International Heat Pipe Conference and 13th international Heat Pipe Symposium*,10-14 June, Pisa, Italy.

Bibliography

[1] A Abbasi Hoseini. *Experimental study of turbulent flow with dispersed rod-like particles through optical measurements*. PhD thesis, Norwegian University of Science and Technology NTNU - Trondheim,, 2014.

[2] A. Abbasi Hoseini, F. Lundell, and H. I. Andersson. Finite-length effects on dynamical behavior of rod-like particles in wall-bounded turbulent flow. *Int. J. Multiph. Flow.*, 76:13 – 21, 2015.

[3] M. Alipour, M. De Paoli, S. Ghaemi, and A. Soldati. Long non-axisymmetric fibres in turbulent channel flow. *J Fluid Mech*, 916, 2021.

[4] S. Allende, C. Henry, and J. Bec. Stretching and buckling of small elastic fibers in turbulence. *Phys. Rev. Lett.*, 121(15):154501, 2018.

[5] M. N. Ardekani and L. Brandt. Turbulence modulation in channel flow of finite-size spheroidal particles. *J Fluid Mech*, 859:887–901, 2019.

[6] D. Bakhuis, V. Mathai, R. A. Verschoof, R. Ezeta, D. Lohse, S. G. Huisman, and C. Sun. Statistics of rigid fibers in strongly sheared turbulence. *Phys Rev Fluids*, 4:072301, Jul 2019.

[7] G. Basterretxea, J. S. Font-Munoz, and I. Tuval. Phytoplankton orientation in a turbulent ocean: A microscale perspective. *Front. Mar. Sci.*, 7:185, 2020. ISSN 2296-7745.

[8] O. Bernstein and M. Shapiro. Direct determination of the orientation distribution function of cylindrical particles immersed in laminar and turbulent shear flows. *J. Aerosol Sci.*, 25(1):113 – 136, 1994. ISSN 0021-8502.

[9] A. D. Bordoloi and E. Variano. Rotational kinematics of large cylindrical particles in turbulence. *J Fluid Mech*, 815:199–222, 2017.

[10] A. D. Bordoloi, E. Variano, and G. Verhille. Lagrangian time scale of passive rotation for mesoscale particles in turbulence. *Front. Mar. Sci.*, 7:473, 2020. ISSN 2296-7745.

[11] S. Bounoua, G. Bouchet, and G. Verhille. Tumbling of inertial fibers in turbulence. *Phys Rev Lett*, 121:124502, Sep 2018.

[12] H. Brenner. The Stokes resistance of an arbitrary particle. *Chem Eng Sci*, 18(1): 1 – 25, 1963.

[13] F. P. Bretherton. The motion of rigid particles in a shear flow at low Reynolds number. *J Fluid Mech*, 14:284–304, January 1962.

[14] C. Brouzet, G. Verhille, and P. Le Gal. Flexible fiber in a turbulent flow: A macroscopic polymer. *Phys Rev Lett*, 112:074501, Feb 2014.

[15] A.R. Bunsell. Fibers with High Modulus. In K.H.J. Buschow, R.W. Cahn, M.C. Flemings, B. Ilschner, E.J. Kramer, S. Mahajan, and P. Veyssière, editors, *Encyclopedia of Materials: Science and Technology*, pages 3151 – 3157. Elsevier, Oxford, 2001.

[16] M. Byron, J. Einarsson, K. Gustavsson, G. Voth, B. Mehlig, and E. Variano. Shape-dependence of particle rotation in isotropic turbulence. *Phys Fluids*, 27 (3):035101, 2015.

[17] A. Capone, G. P. Romano, and A. Soldati. Experimental investigation on interactions among fluid and rod-like particles in a turbulent pipe jet by means of particle image velocimetry. *Exp Fluids*, 56(1):1, 2014. ISSN 1432-1114.

[18] A. Capone, M. Miozzi, and G. P. Romano. On translational and rotational relative velocities of fibers and fluid in a turbulent channel flow with a backward-facing step. *Int. J. Multiph. Flow.*, 94:189 – 200, 2017. ISSN 0301-9322.

[19] N. R. Challabotla, L. Zhao, and H. I. Andersson. Shape effects on dynamics of inertia-free spheroids in wall turbulence. *Phys Fluids*, 27(6):061703, 2015.

[20] N. R. Challabotla, L. Zhao, and H. I. Andersson. Orientation and rotation of inertial disk particles in wall turbulence. *J Fluid Mech*, 766:R2, 2015.

[21] D. Crowdy. Flipping and scooping of curved 2d rigid fibers in simple shear: The Jeffery equations. *Phys Fluids*, 28(5):053105, 2016.

[22] S. Dearing, M. Campolo, A. Capone, and A. Soldati. Phase discrimination and object fitting to measure fibers distribution and orientation in turbulent pipe flows. *Exp. Fluids*, 54:1419, 2012.

[23] M. H. Di Benedetto, N. T. Ouellette, and J. R. Koseff. Transport of anisotropic particles under waves. *J Fluid Mech*, 837:320–340, 2018.

[24] M. H. Di Benedetto, J. R. Koseff, and N. T. Ouellette. Orientation dynamics of nonspherical particles under surface gravity waves. *Phys Rev Fluids*, 4:034301, Mar 2019.

[25] Michelle H. DiBenedetto. Non-breaking wave effects on buoyant particle distributions. *Frontiers in Marine Science*, 7:148, 2020. ISSN 2296-7745.

[26] M. Do-Quang, G. Amberg, G. Brethouwer, and A. V. Johansson. Simulation of finite-size fibers in turbulent channel flows. *Phys Rev E*, 89:013006, Jan 2014.

[27] D. Dotto and C. Marchioli. Orientation, distribution, and deformation of inertial flexible fibers in turbulent channel flow. *Acta Mech.*, 230(2):597–621, 2019.

[28] D. Dotto, A. Soldati, and C. Marchioli. Deformation of flexible fibers in turbulent channel flow. *Meccanica*, 55(2):343–356, 2020. ISSN 1572-9648.

[29] G. E. Elsinga, F. Scarano, B. Wieneke, and B. W. van Oudheusden. Tomographic particle image velocimetry. *Exp Fluids*, 41(6):933–947, 2006.

[30] A. Eshghinejadfard, S. A. Hosseini, and D. Thevenin. Fully-resolved prolate spheroids in turbulent channel flows: A lattice Boltzmann study. *AIP Advances*, 7(9):095007, 2017.

[31] J. S. Guasto, R. Rusconi, and R. Stocker. Fluid mechanics of planktonic microorganisms. *Annl Rev Fluid Mech*, 44(1):373–400, 2012.

[32] Pejman Hadi Sichani. *Direct numerical simulation of stably stratified turbulence under Oberbeck-Boussinesq hypotheses at high Reynolds and Richardson numbers.* Wien, 2018.

[33] K. M. O. Håkansson, M. Kvick, F. Lundell, L. Prahl Wittberg, and L. D. Söderberg. Measurement of width and intensity of particle streaks in turbulent flows. *Exp Fluids*, 54(6):1555, 2013. ISSN 1432-1114.

[34] B. Hejazi, M. Krellenstein, and G. A. Voth. Using deformable particles for single-particle measurements of velocity gradient tensors. *Exp Fluids*, 60(10):153, 2019. ISSN 1432-1114.

[35] E. J. Hinch and L. G. Leal. Rotation of small non-axisymmetric particles in a simple shear flow. *J Fluid Mech*, 92(3):591–607, 1979.

[36] K. Iwamoto, Y. Suzuki, and N. Kasagi. Reynolds number effect on wall turbulence: toward effective feedback control. *Int. J. Heat Fluid Fl.*, 23(5):678–689, 2002.

[37] G B Jeffery. The motion of ellipsoidal particles immersed in a viscous fluid. *Proc. R. Soc. Lond. A*, 102(715):161–179, 1922.

[38] L. Jiang, E. Calzavarini, and C. Sun. Rotation of anisotropic particles in Rayleigh-Bénard turbulence. *J Fluid Mech*, 901:A8, 2020.

[39] Z. Jiang, J. Verlinde, E. E. Clothiaux, K. Aydin, and C. Schmitt. Shapes and Fall Orientations of Ice Particle Aggregates. *J. Atmos. Sci.*, 76(7):1903–1916, 06 2019. ISSN 0022-4928.

[40] Y. Jie, C. Xu, J. R. Dawson, H. I. Andersson, and L. Zhao. Influence of the quiescent core on tracer spheroidal particle dynamics in turbulent channel flow. *J. Turb*, 20(7):424–438, jul 2019.

[41] Ian A. Kane, Michael A. Clare, Elda Miramontes, Roy Wogelius, James J. Rothwell, Pierre Garreau, and Florian Pohl. Seafloor microplastic hotspots controlled by deep-sea circulation. *Science*, 368(6495):1140–1145, 2020. ISSN 0036-8075.

[42] C. Kleinstreuer and Y. Feng. Computational analysis of non-spherical particle transport and deposition in shear flow with application to lung aerosol dynamics – a review. *J Biomech Eng.*, 135(2), 02 2013. ISSN 0148-0731.

[43] S. J. Kline, W. C. Reynolds, F. A. Schraub, and P. W. Runstadler. The structure of turbulent boundary layers. *Journal of Fluid Mechanics*, 30(4):741–773, 1967.

[44] L. Korson, W. Drost-Hansen, and F. J. Millero. Viscosity of water at various temperatures. *J. Phys. Chem*, 73(1):34–39, jan 1969. ISSN 0022-3654.

[45] S Kotz, N Balakrishnan, and N L Johnson. *Continuous multivariate distributions, Volume 1: Models and applications*. John Wiley & Sons, 2004.

[46] S. Kramel, G. A. Voth, S. Tympel, and F. Toschi. Preferential rotation of chiral dipoles in isotropic turbulence. *Phys Rev Lett*, 117:154501, Oct 2016.

[47] J. E. Kristjànsson, J. M. Edwards, and D. L. Mitchell. Impact of a new scheme for optical properties of ice crystals on climates of two gcms. *JCR: Atmospheres*, 105(D8):10063–10079, 2000.

[48] P. J. Krochak, Olson J. A., and D. M. Martinez. Near-wall estimates of the concentration and orientation distribution of a semi-dilute rigid fibre suspension in poiseuille flow. *J Fluid Mech*, 653:431–462, 2010.

[49] S. Kuperman, L. Sabban, and R. van Hout. Inertial effects on the dynamics of rigid heavy fibers in isotropic turbulence. *Phys Rev Fluids*, 4:064301, Jun 2019.

[50] G. Lecrivain, T. B. P. Grein, R. Yamamoto, U. Hampel, and T. Taniguchi. Eulerian/Lagrangian formulation for the elasto-capillary deformation of a flexible fibre. *J. Comput. Phys.*, 409:109324, 2020. ISSN 00219991.

[51] F. Lundell, L. D. Söderberg, and P. H. Alfredsson. Fluid mechanics of papermaking. *Annl Rev Fluid Mech*, 43(1):195–217, 2011.

[52] C. Marchioli, M. Fantoni, and A. Soldati. Orientation, distribution, and deposition of elongated, inertial fibers in turbulent channel flow. *Phys Fluids*, 22(3): 033301, 2010.

[53] C. Marchioli, L. Zhao, and H. I. Andersson. On the relative rotational motion between rigid fibers and fluid in turbulent channel flow. *Phys Fluids*, 28(1):013301, 2016.

[54] G. G. Marcus, S. Parsa, S. Kramel, R. Ni, and G. A. Voth. Measurements of the solid-body rotation of anisotropic particles in 3D turbulence. *New J. Phys.*, 16, 2014. ISSN 13672630.

[55] E. Meiburg and B. Kneller. Turbidity currents and their deposits. *Annl Rev Fluid Mech*, 42(1):135–156, 2010.

[56] P. H. Mortensen, H. I. Andersson, J. J. J. Gillissen, and B. J. Boersma. Dynamics of prolate ellipsoidal particles in a turbulent channel flow. *Phys Fluids*, 20(9): 093302, 2008.

[57] R. D. Moser, J. Kim, and N. N. Mansour. Direct numerical simulation of turbulent channel flow up to Re=590. *Phys Fluids*, 11(4):943–945, 1999.

[58] A. S. Mountford and M. A. Morales Maqueda. Eulerian modeling of the three-dimensional distribution of seven popular microplastic types in the global ocean. *Journal of Geophysical Research: Oceans*, 124(12):8558–8573, 2019.

[59] R Ni, N T Ouellette, and G A. Voth. Alignment of vorticity and rods with lagrangian fluid stretching in turbulence. *J Fluid Mech*, 743:R3, 2014.

[60] R. Ni, S. Kramel, N. T. Ouellette, and G. A. Voth. Measurements of the coupling between the tumbling of rods and the velocity gradient tensor in turbulence. *J Fluid Mech.*, 766:202–225, 2015.

[61] M. Novara and F. Scarano. Performances of motion tracking enhanced Tomo-PIV on turbulent shear flows. *Exp Fluids*, 52(4):1027–1041, 2012.

[62] Theresa B. Oehmke, Ankur D. Bordoloi, Evan Variano, and Gautier Verhille. Spinning and tumbling of long fibers in isotropic turbulence. *Phys. Rev. Fluids*, 6:044610, Apr 2021.

[63] Victor Onink, David Wichmann, Philippe Delandmeter, and Erik van Sebille. The role of ekman currents, geostrophy, and stokes drift in the accumulation of floating microplastic. *Journal of Geophysical Research: Oceans*, 124(3):1474–1490, 2019.

[64] S. Parsa and G. A. Voth. Inertial range scaling in rotations of long rods in turbulence. *Phys Rev Lett*, 112:024501, Jan 2014.

[65] S. Parsa, J. S. Guasto, M. Kishore, N. T. Ouellette, J. P. Gollub, and G. A. Voth. Rotation and alignment of rods in two-dimensional chaotic flow. *Phys Fluids*, 23 (4):043302, 2011.

[66] S. Parsa, E. Calzavarini, F. Toschi, and G. A. Voth. Rotation rate of rods in turbulent fluid flow. *Phys Rev Lett*, 109:134501, Sep 2012.

[67] M. Parsheh, M. L. Brown, and C. K. Aidun. On the orientation of stiff fibres suspended in turbulent flow in a planar contraction. *J Fluid Mech*, 545:245–269, 2005.

[68] Jason R. Picardo, Rahul Singh, Samriddhi Sankar Ray, and Dario Vincenzi. Dynamics of a long chain in turbulent flows: impact of vortices. *Philosophical Transactions of the Royal Society A: Mathematical, Physical and Engineering Sciences*, 378(2175):20190405, 2020.

[69] N. Pujara, T. B. Oehmke, A. D. Bordoloi, and Evan A. Variano. Rotations of large inertial cubes, cuboids, cones, and cylinders in turbulence. *Phys Rev Fluids*, 3:054605, May 2018.

[70] N. Pujara, G. A. Voth, and E. A. Variano. Scale-dependent alignment, tumbling and stretching of slender rods in isotropic turbulence. *J Fluid Mech*, 860:465–486, 2019.

[71] Peter S Ross, Stephen Chastain, Ekaterina Vassilenko, Anahita Etemadifar, Sarah Zimmermann, Sarah-Ann Quesnel, Jane Eert, Eric Solomon, Shreyas Patankar, Anna M Posacka, and Bill Williams. Pervasive distribution of polyester fibres in the Arctic Ocean is driven by Atlantic inputs. *Nature Communications*, 12(1): 106, 2021. ISSN 2041-1723.

[72] W A Rowin and S. Ghaemi. Streamwise and spanwise slip over a superhydrophobic surface. *J Fluid Mech.*, 870:1127–1157, 2019.

[73] A. Roy, R. J. Hamati, L. Tierney, D. L. Koch, and G. A. Voth. Inertial torques and a symmetry breaking orientational transition in the sedimentation of slender fibres. *J Fluid Mech*, 875:576–596, 2019.

[74] L. Sabban, A. Cohen, and R. van Hout. Temporally resolved measurements of heavy, rigid fibre translation and rotation in nearly homogeneous isotropic turbulence. *J Fluid Mech*, 814:42–68, 2017.

[75] K. Sangtae and J. K. Seppo. Chapter 5 - resistance and mobility relations. In Sangtae Kim and Seppo J. Karrila, editors, *Microhydrodynamics*, pages 107 – 145. Butterworth-Heinemann, 1991. ISBN 978-0-7506-9173-4.

[76] F Scarano. Tomographic PIV: principles and practice. *Meas Sci Technol*, 24(1): 012001, oct 2012.

[77] D. Schanz, S. Gesemann, and A. Schröder. Shake-The-Box: Lagrangian particle tracking at high particle image densities. *Exp Fluids*, 57(5):1–27, 2016.

[78] Subhani Shaik, Sofia Kuperman, Vladislav Rinsky, and René van Hout. Measurements of length effects on the dynamics of rigid fibers in a turbulent channel flow. *Phys. Rev. Fluids*, 5:114309, Nov 2020.

[79] M. Shin and D. L. Koch. Rotational and translational dispersion of fibres in isotropic turbulent flows. *J Fluid Mech*, 540:143–173, 2005.

[80] M. J. Shultz. Crystal growth in ice and snow. *Physical Today*, 71(2):34–35, 2018.

[81] Miriam F. Sterl, Philippe Delandmeter, and Erik van Sebille. Influence of barotropic tidal currents on transport and accumulation of floating microplastics in the global open ocean. *Journal of Geophysical Research: Oceans*, 125(2): e2019JC015583, 2020. e2019JC015583 10.1029/2019JC015583.

[82] H. Tang, Z. Tian, J. Yan, and S. Yuan. Determining drag coefficients and their application in modelling of turbulent flow with submerged vegetation. *Adv. Wat. Res.*, 69:134 – 145, 2014.

[83] I. R. Thorp and J. R. Lister. Motion of a non-axisymmetric particle in viscous shear flow. *J Fluid Mech*, 872:532–559, 2019.

[84] Erik van Sebille, Stephen M. Griffies, Ryan Abernathey, Thomas P. Adams, Pavel Berloff, Arne Biastoch, Bruno Blanke, Eric P. Chassignet, Yu Cheng, Colin J. Cotter, Eric Deleersnijder, Kristofer Döös, Henri F. Drake, Sybren Drijfhout,

Stefan F. Gary, Arnold W. Heemink, Joakim Kjellsson, Inga Monika Koszalka, Michael Lange, Camille Lique, Graeme A. MacGilchrist, Robert Marsh, C. Gabriela Mayorga Adame, Ronan McAdam, Francesco Nencioli, Claire B. Paris, Matthew D. Piggott, Jeff A. Polton, Siren Rühs, Syed H.A.M. Shah, Matthew D. Thomas, Jinbo Wang, Phillip J. Wolfram, Laure Zanna, and Jan D. Zika. Lagrangian ocean analysis: Fundamentals and practices. *Ocean Modelling*, 121:49–75, 2018. ISSN 1463-5003.

[85] G. A. Voth and A. Soldati. Anisotropic particles in turbulence. *Annl Rev Fluid Mech*, 49(1):249–276, 2017.

[86] Greg A. Voth. Disks aligned in a turbulent channel. *Journal of Fluid Mechanics*, 772:1–4, 2015.

[87] G. Wang, M. Abbas, Z. Yu, A. Pedrono, and E. Climent. Transport of finite-size particles in a turbulent couette flow: The effect of particle shape and inertia. *Int. J. Multiph. Flow.*, 107:168 – 181, 2018. ISSN 0301-9322.

[88] J. Wang, E. J. Tozzi, M. D. Graham, and D. J. Klingenberg. Flipping, scooping, and spinning: Drift of rigid curved nonchiral fibers in simple shear flow. *Phys Fluids*, 24(12):123304, 2012.

[89] B Wieneke. Volume self-calibration for 3D particle image velocimetry. *Exp Fluids*, 45(4):549–556, 2008. ISSN 1432-1114.

[90] J. Yang, N. Francois, H. Punzmann, M. Shats, and H. Xia. Diffusion of ellipsoids in laboratory two-dimensional turbulent flow. *Phys Fluids*, 31(8):085116, 2019.

[91] L. Zhao and H. I. Andersson. Why spheroids orient preferentially in near-wall turbulence. *J Fluid Mech*, 807:221–234, 2016.

[92] L. Zhao, C. Marchioli, and H. I. Andersson. Slip velocity of rigid fibers in turbulent channel flow. *Phys Fluids*, 26(6):063302, 2014.

[93] L. Zhao, N. R. Challabotla, H. I. Andersson, and E. A. Variano. Rotation of nonspherical particles in turbulent channel flow. *Phys Rev Lett*, 115:244501, Dec 2015.

[94] L. Zhao, K. Gustavsson, R. Ni, S. Kramel, G. A. Voth, H. I. Andersson, and B. Mehlig. Passive directors in turbulence. *Phys Rev Fluids*, 4:054602, May 2019.

[95] C. Zhu, Z. Yu, and X. Shao. Interface-resolved direct numerical simulations of the interactions between neutrally buoyant spheroidal particles and turbulent channel flows. *Phys Fluids*, 30(11):115103, 2018.

[96] C. Zhu, Z. Yu, D. Pan, and X. Shao. Interface-resolved direct numerical simulations of the interactions between spheroidal particles and upward vertical turbulent channel flows. *J Fluid Mech*, 891:A6, 2020.

[97] F Zonta, C Marchioli, and A Soldati. Modulation of turbulence in forced convection by temperature-dependent viscosity. *J Fluid Mech*, 697:150, 2012.